UNICAMP

GUILHERME ABREU FARIA

Exploring Metallic Materials Behavior Through *In Situ* Crystallographic Studies by Synchrotron Radiation

Explorando o Comportamento de Materiais Metálicos Através de Estudos Cristalográficos In Situ *via Radiação Síncrotron*

102/2014

CAMPINAS
2014

UNIVERSIDADE ESTADUAL DE CAMPINAS
FACULDADE DE ENGENHARIA MECÂNICA
COMISSÃO DE PÓS-GRADUAÇÃO EM ENGENHARIA MECÂNICA
DEPARTAMENTO DE MATERIAIS E PROCESSOS DE FABRICAÇÃO

ACADEMIC MASTERS DISSERTATION
DISSERTAÇÃO DE MESTRADO ACADEMICO

Exploring Metallic Materials Behavior Through *In Situ* Crystallographic Studies by Synchrotron Radiation

Explorando o Comportamento de Materiais Metálicos Através de Estudos Cristalográficos In Situ *via Radiação Síncrotron*

Masters dissertation presented to the School of Mechanical Engineering of the State University of Campinas in partial fulfillment of the requirements for the degree of Master in Mechanical Engineering, in the Materials and Fabrication Processes Area.

Dissertação de Mestrado apresentada à Faculdade de Engenharia Mecânica da Universidade Estadual de Campinas como parte dos requisitos exigidos para obtenção do título de Mestre em Engenharia Mecânica, na Área de materiais e processos de fabricação.

Orientador: Prof. Dr. Antonio Jose Ramirez Londono

ESTE EXEMPLAR CORRESPONDE À VERSÃO FINAL DA DISSERTAÇÃO DEFENDIDA PELO ALUNO GUILHERME ABREU FARIA, E ORIENTADA PELO PROF. DR ANTONIO JOSE RAMIREZ LONDONO.

Antonio José Ramirez

ASSINATURA DO ORIENTADOR

CAMPINAS
2014

Ficha catalográfica
Universidade Estadual de Campinas
Biblioteca da Área de Engenharia e Arquitetura
Rose Meire da Silva - CRB 8/5974

F225e

Faria, Guilherme Abreu, 1987-
Exploring metallic materials behavior through *in situ* crystallographic studies by synchrotron radiation / Guilherme Abreu Faria. – Campinas, SP : [s.n.], 2014.

Orientador: Antonio Jose Ramirez Londono.
Dissertação (mestrado) – Universidade Estadual de Campinas, Faculdade de Engenharia Mecânica.

1. Experimentos *in situ*. 2. Raios X - Difração. 3. Transformações de fase. I. Ramirez Londono, Antonio Jose. II. Universidade Estadual de Campinas. Faculdade de Engenharia Mecânica. III. Título.

Informações para Biblioteca Digital

Título em outro idioma: Explorando o comportamento de materiais metálicos através de estudos cristalográficos *in situ* via radiação síncrotron
Palavras-chave em inglês:
In situ experiments
X rays - Diffraction
Phase transformations
Área de concentração: Materiais e Processos de Fabricação
Titulação: Mestre em Engenharia Mecânica
Banca examinadora:
Antonio Jose Ramirez Londono [Orientador]
Carlos Kenichi Suzuki
Hugo Ricardo Zschommler Sandim
Data de defesa: 30-09-2014
Programa de Pós-Graduação: Engenharia Mecânica

UNIVERSIDADE ESTADUAL DE CAMPINAS
FACULDADE DE ENGENHARIA MECÂNICA
COMISSÃO DE PÓS-GRADUAÇÃO EM ENGENHARIA MECÂNICA
DEPARTAMENTO DE MATERIAIS E PROCESSOS DE FABRICAÇÃO

DISSERTAÇÃO DE MESTRADO ACADEMICO

Exploring Metallic Materials Behavior Through *In Situ* Crystallographic Studies by Synchrotron Radiation

Explorando o Comportamento de Materiais Metálicos Através de Estudos Cristalográficos In Situ *via Radiação Síncrotron*

Autor: Guilherme Abreu Faria
Orientador: Prof. Dr. Antonio Jose Ramirez Londono

A Banca Examinadora composta pelos membros abaixo aprovou esta Dissertação:

Antonio José Ramirez

Prof. Dr. Antonio Jose Ramirez Londono, Presidente
LNNano/Centro Nacional de Pesquisa em Energia e Materiais,
DEMA/FEM/Universidade Estadual de Campinas

Prof. Dr. Carlos Kenichi Suzuki
DEMA/FEM/ Universidade Estadual de Campinas

Prof. Dr. Hugo Ricardo Zschommler Sandim
EEL/Universidade de São Paulo

Campinas, 30 de Setembro de 2014

Dedico este trabalho a minha família.

Acknowledgements

I would like to thank all people and entities that, in some way or another, helped this project become a reality:

To my parents and brother, for showing me the joy of learning.

To my supervisor, Antonio Ramirez, who always showed me I could go further.

To Leonardo Wu and the TMEC team, for their imperturbable disposition to help me.

To Júlia, for always being there for me.

To Julian Escobar, partner in countless beamtimes, and in the challenges and joys of science.

To Suresh Babu, for the inspiring discussions we had.

To the CPM team, for their patience and support.

To Prof. Dr. Jorge Otubo and Prof. Dr. Heide Bernardi, for providing the Stainless Steel SMAs, and for the several discussions regarding this material.

To the LNNano and LNLS staff, for the help and support.

To the friends from the Physics and Mathematics Institutes at Unicamp, for their disposition to discuss this work, and inspire me by doing that.

To all XTMS users I got in touch with, who showed me how beautiful materials science can be.

To the Brazilian National Petroleum Agency and Brazilian National Council for Technologic and Scientific Development, for granting the scholarship and financial support used in this work.

To the Unicamp Mechanical Engineering School, for the opportunity.

To the State University of Campinas, my academic cradle.

“*There are the rushing waves*
mountains of molecules
each stupidly minding its own business
trillions apart
yet forming white surf in unison […]”
Richard Phillips Feynman

Abstract

FARIA, Guilherme Abreu, *Exploring Metallic Materials Behavior Through In Situ Crystallographic Studies by Synchrotron Radiation,* Campinas: School of Mechanical Engineering, University of Campinas, 2014.

The aim of this work was to develop measurement and data analysis methodologies for the XTMS experimental installation. This facility was engineered to simultaneously collect X-ray diffraction and thermo-mechanical information of materials as they are subjected to controlled thermo-mechanical conditions. This is an area of great interest for material scientists given the wide range of thermo-mechanical properties correlated with microscopic properties which are accessible through X-ray diffraction. Developments performed during this work include the development and/or study of measurement strategies, sample designs, and data processing and analysis, as well as the characterization of the XTMS installation as an X-ray diffraction station. As part of the work, the installation was used to study several cases of scientific interest, involving different testing and data analysis methodologies. The studies performed were the deformation of a shape memory alloy, the isothermal ferrite decomposition on a Superduplex stainless steel UNS-S32750, and phase transformations on a SuperCr13 supermartensitic steel through dilatometry coupled with time resolved X-ray diffraction.

Key Words: *In situ* Experiments, X rays - Diffraction, Phase Transformations.

Resumo

FARIA, Guilherme Abreu, *Explorando o Comportamento de Materiais Metálicos Através de Estudos Cristalográficos In Situ via Radiação Síncrotron*, Campinas: Faculdade de Engenharia Mecânica, Universidade Estadual de Campinas, 2014.

O objetivo deste trabalho foi desenvolver a metodologia de medição e análise de dados para a instalação experimental XTMS. Esta instalação foi projetada para possibilitar a medição simultânea de difração de raios X e informações térmicas e mecânicas de materiais enquanto estes são submetidas a condições termomecânicas controladas. Esta é uma área de grande interesse para cientistas de materiais uma vez que uma vasta gama de propriedades termomecânicas têm suas origens em propriedades microscópicas que são acessíveis através de dados de difração. Durante o trabalho, foram estudadas estratégias de medição, desenhos de amostras, métodos de processamento e análise de dados, assim como foi feita a caracterização da instalação como equipamento de medida de dados de difração. Como parte do trabalho, a instalação foi aplicada no estudo de casos científicos de interesse, que envolvem tanto diferentes metodologias de ensaios quanto dados de difração que exigem diferentes metodologias de análise. Os estudos consistiram em um ensaio de deformação em uma liga com memória de forma, ensaios de decomposição isotérmica em um aço inoxidável Superduplex UNS-S32750, e um ensaio de dilatometria acompanhado por difração do aço supermartensítico SuperCr13.

Palavras Chave: Experimentos *in situ*; Raios X - Difração, Transformações de fase.

Figure List

Table List

Abbreviations and Symbols List

Abbreviations

XTMS - X-ray scattering and thermomechanical simulation facility

LNNano - Brazilian Nanotechnology Laboratory *(Laboratório Nacional de Nanotecnologia)*

LNLS - Brazilian Synchrotron Light Laboratory *(Laboratório Nacional de Luz Síncrotron)*

CPM - Materials Processing and Characterization Group *(Grupo de Processamento e caracterização de materiais)*

SMA - Shape Memory Alloy

SDSS - Superduplex Stainless Steel

SMSS - Supermartensitic Stainless Steel

FCC - Face Centered Cubic

BCC - Body Centered Cubic

BCT - Body Centered Tetragonal

HCP - Hexagonal Close Packed

TRXRD - Time Resolved X-ray Diffraction

TRIP - Transformation Induced Plasticity

FWHM - Full Width at Half Maximum

Symbols

This work involves several areas of knowledge, in which a same symbol is used with different meanings. For example, σ is a precipitate phase in the field of steel metallurgy, stress in mechanical metallurgy, and the standard deviation in statistics. The author seemed fit to keep the typical literature nomenclature, which led to the same symbol being used for different meanings throughout the text. However, in a single section, a symbol has only one meaning, for example, in the ferrite decomposition section, where the σ precipitate is constantly mentioned, the symbol σ is not used to denote stress. In this list, symbol meanings are presented based on the section they are mentioned.

2θ - X-Ray scattering angle [°]
(All Sections)

$2\theta_{obs}$ - Observed diffraction angle [°]
(All Sections)

$\Delta 2\theta$ - Difference between observed diffraction angle and real diffraction angle due to sample misalignment [°]
(All Sections)

$2\theta_g$ - Angle between $\mathbf{e_z}$ and the vector pointing from the goniometer turning axis to the detector center pixel [°]
(All Sections)

α - Lattice Parameter, angle between $\mathbf{a_2}$ and $\mathbf{a_3}$ [°]
(Section 2.3)
- BCC phase in steels (ferrite)
(Sections 2.6.2; 4.5; 5.4.2)

α' - BCC/BCT martensitic phase in steels (martensite)
(All Sections)

β - Lattice Parameter, angle between $\mathbf{a_1}$ and $\mathbf{a_3}$ [°]
(Section 2.3)
- Diffraction peak width [°]
(Sections 2.4; 4.2; 4.6)

β_{size} - Peak broadening due to crystallite size [°]
(All Sections)

β_{strain} - Peak broadening due to microstrain [°]
(All Sections)

β_s - Total peak broadening due to sample effects [°]
(All Sections)

β_{geo} - Peak broadening due to measurement geometry [°]
(All Sections)

β_{div} - Incident beam divergence [°]
(All Sections)

β_{inst} - Total peak broadening due to the instrument [°]
(All Sections)

β_{obs} - Observed peak FWHM [°]
(All Sections)

γ - Lattice Parameter, angle between $\mathbf{a_1}$ and $\mathbf{a_2}$ [°]
(Section 2.3)
- FCC phase in steels (austenite)
(Sections 2.6; 4.4; 4.5; 4.6; 5.4)

γ^* - FCC phase in steels (secondary austenite in Duplex and Superduplex steels)
(All Sections)

ε - HCP martensitic phase in steels
(Sections 2.6.1; 4.4; 5.4.1)
- Strain
(Sections 4.1; 4.6; Appendix A)

$<\varepsilon>$ - Microstrain
(All Sections)

$[\boldsymbol{\varepsilon}]$ - Strain tensor
(All Sections)

$\varepsilon_{\{110\}}$ - Macrostrain for martensite observed {110} family
(All Sections)

$\varepsilon_{\{200\}}$ - Macrostrain for martensite observed {200} family
(All Sections)

θ - Bragg's angle [°]
(All Sections)

$\theta_{\{hkl\}}$ - Bragg's angle for plane family {hkl} [°]
(All Sections)

λ - X-ray wavelength [Å]
(All Sections)

μ - X-Ray mass attenuation coefficient [m^2/kg]
(All Sections)

σ - Second phase, common in stainless steels (sigma phase)
(Sections 2.3; 2.6.2; 4.5; 5.4.2)
- Stress [MPa]
(Sections 2.6.1; 4.6; 5.4.2; Appendix A)

σ - Standard Deviation
(Sections 4.2;4.3)

$[\boldsymbol{\sigma}]$ - Stress tensor
(All Sections)

σ_{ij} - Component ij of the stress tensor [MPa]
(All Sections)

σ_K - Average between σ_{11} and σ_{22} stress components [MPa]
(All Sections)

σ_{dy} - Standard deviation associated with dy [mm]
(All Sections)

σ_{yedge} - Standard deviation associated with y_{edge} [mm]
(All Sections)

σ_{fp} - Standard deviation associated with fp [mm]
(All Sections)

σ_{p0} - Standard deviation associated with p_0 [mm]
(All Sections)

σ_{ps} - Standard deviation associated with p_s [mm]
(All Sections)

σ_{ω} - Standard deviation associated with ω [°]
(All Sections)

σ_{dz} - Standard deviation associated with dz [mm]
(All Sections)

$\sigma_{\Delta y}$ - Standard deviation associated with Δy [mm]
(All Sections)

$\sigma_{\Delta z}$ - Standard deviation associated with Δz [mm]
(All Sections)

$\sigma_{\Delta 2\theta}$ - Standard deviation associated with $\Delta 2\theta$ [°]
(All Sections)

σ_d - Standard deviation associated with d [Å]
(All Sections)

σ_{oan} - Standard deviation associated with o_{an}
(All Sections)

$\sigma_{F\{hkl\}}$ - Standard deviation associated with $F_{\{hkl\}}$
(All Sections)

$\sigma_{R\{hkl\}}$ - Standard deviation associated with $R_{\{hkl\}}$
(All Sections)

ϕ - Sample diameter [mm]
(All Sections)

ϕ_0 - Sample diameter at the start of a test [mm]
(All Sections)

ω - Angle between X-ray incident beam and sample surface [°]
(All Sections)

ω_0 - ω for a standard sample used for alignment [°]
(All Sections)

ω_s - ω for a standard sample used for alignment [°]
(All Sections)

$\mathbf{a_i}$ - Vector set used in the construction of a crystallographic unit cell, i = 1,2,3
(All Sections)

a - Lattice parameter, $\mathbf{a_1}$ module [Å]
(All Sections)
- When used as an index, indicates a an atom in a crystallographic site
(All Sections)

a_0 - Unstrained lattice parameter [Å]
(All Sections)

a_{110}^{obs} - Observed lattice parameter for martensite {110} family [Å]
(All Sections)

a_{200}^{obs} - Observed lattice parameter for martensite {200} family [Å]
(All Sections)

$A(\theta_{\{hkl\}})$ - absorption factor;
(All Sections)

b - Lattice parameter, $\mathbf{a}_2$ module [Å]
(All Sections)

c - Lattice parameter, $\mathbf{a}_3$ module [Å]
(All Sections)

cz - Distance between $\mathbf{gl}_\mathbf{z}$ origin and the sample cross section center [mm]
(All Sections)

cz_0 - cz for a standard sample used for alignment [mm]
(All Sections)

cz_s - cz for a sample under alignment [mm]
(All Sections)

d - Interplanar spacing [Å]
(All Sections)

$d_{\{hkl\}}$ - Interplanar spacing of the {hkl} plane family [Å]
(All Sections)

$detd$ - Distance between goniometer turning axis and the detector center pixel [mm]
(All Sections)

dy - Displacement along $\mathbf{gl}_\mathbf{y}$ required to align a sample, distance between y_{edge} and $\mathbf{gl}_\mathbf{y}$ origin [mm]
(All Sections)

dz - Displacement along $\mathbf{gl}_\mathbf{z}$ required to align a sample [mm]
(All Sections)

D - Diffusion constant
(All Sections)

$\mathbf{e}_{\mathbf{x,y,z}}$ - Incident X-ray beam reference frame coordinate system
(All Sections)

f - Rate at which nuclei become critical in a phase transformation [s^{-1}]
(All Sections)

fp - Sample width along the irradiated surface [mm]
(All Sections)

$F_{p\{hkl\}}$ - structure factor of for the $\{hkl\}$ plane family of p phase;
(All Sections)

$\mathbf{gl}_{\mathbf{x,y,z}}$ - Simulator reference frame coordinate system
(All Sections)

G - Gibbs free energy [J]
(All Sections)

ΔG_V - Bulk Gibbs free energy difference between two phases [J]
(All Sections)

ΔG_d - Energy released during heterogeneous nucleation [J]
(All Sections)

ΔG^* - Energy barrier to a phase transformation [J]
(All Sections)

h - Miller index, defined along $\mathbf{a}_1$
(All Sections)

I - Transmitted beam intensity
(All Sections)

I_0 - Incident beam intensity
(All Sections)

$\mathbf{J}$ - Material flux (diffusion) [kg/s]
(All Sections)

k - Miller index, defined along $\mathbf{a}_2$
(All Sections)

l - Miller index, defined along $\mathbf{a}_3$
(All Sections)

$L(\theta_{\{hkl\}})$ - Lorentz factor;
(All Sections)

$M_{p\{hkl\}}$ - multiplicity factor for the $\{hkl\}$ plane family of p phase;
(All Sections)

n - When used as an index, indicates a crystallographic site in a unit cell
(All Sections)

o_{an} - Fraction occupation of atom a at site n
(All Sections)

p - Sample thickness, perpendicular to the irradiated surface [mm]
(All Sections)

p - When used as an index, indicates a crystallographic phase present in a material
(All Sections)

p_0 - p for a standard sample used for alignment [mm]
(All Sections)

p_s - p for a sample under alignment [mm]
(All Sections)

$P_{p\{hkl\}}$ - preferred orientation factor for the $\{hkl\}$ plane family of p phase;
(All Sections)

$Pol(\theta_{\{hkl\}})$- Polarization factor.
(All Sections)

$R_{p\{hkl\}}$ - constant relating diffracted intensity from $\{hkl\}$ plane family of p phase to p phase volume fraction;
(All Sections)

[S] - Compliance tensor
(All Sections)

S_{ij} - Component ij of the Compliance tensor (in Voigt notation) [MPa^{-1}]
(All Sections)

tr - Distance travelled by an incident beam inside a sample before being scattered [mm]
(All Sections)

tr' - Distance travelled by the scattered beam inside the sample [mm]
(All Sections)

v_p - unit cell volume of phase p [$Å^3$]
(All Sections)

w - Incident beam FWHM at the sample position [mm]
(All Sections)

W - Work [J]
(All Sections)

x,y,z - Goniometer reference frame coordinate system
(All Sections)

y_{edge}	Beam position at the sample upper edge in the $\mathbf{gl_y}$ coordinate system *(All Sections)*	[mm]
Δy	Distance between $\mathbf{gl_y}$ and $\mathbf{y}$ origins *(All Sections)*	[mm]
Δz	Distance between $\mathbf{gl_z}$ and $\mathbf{z}$ origins *(All Sections)*	[mm]

Summary

1. INTRODUCTION

The correlation between the materials macroscopic properties, such as their mechanical and thermal behavior, and their microstructure and crystalline structure has always been a key topic for material science. This connection is observed in several examples, such as: in duplex stainless steels (DSS), where the coexistence between two crystallographic phases ensures interesting mechanical properties as well as high corrosion resistance; in transformation induced plasticity (TRIP) steels, where good conformability and elevated strength are obtained through retaining a fraction of metastable austenite in a martensitic matrix; or in shape memory alloys (SMA), where the memory and pseudo-elasticity effects are the result of displacive reversible phase transformations.

Complex measurement and analysis techniques based on the scattering of photons, neutrons, and electrons have been used to investigate this correlation and address a wide range of materials macro- and micro-structural characteristics, including chemical composition, grain morphology and orientation, and crystallographic quantities such as lattice parameters, among many other. Understanding the materials characteristics and properties is essential not only to reach a deep level of fundamental knowledge but also to develop better materials and processing techniques.

Several techniques based on the analysis of the interaction between samples and X-rays, neutrons or electrons have been optimized to investigate the aforementioned characteristics and properties through the last century. Examples include diffraction, spectroscopy, tomography and microscopy. Despite normally requiring special sample preparation, these techniques are non-destructive and, although their use has been mostly limited to *ex situ* or *post mortem* analysis, they could be used *in situ*.

The motivation for *in situ* application of such techniques in metallic materials can be divided in two fields of interest, fundamental research and practical investigation. In the fundamental field, a number of thermodynamic phenomena take place under specific thermomechanical conditions. Examples of these phenomena include diffusive and displacive transformations, chemical partitioning, recovery and/or recrystallization, deformation mechanisms etc.

On the practical field, two industry related motivations can be listed, one regarding the investigation of new materials, and the other regarding the investigation of processes. The first practical motivation arises from the fact that several alloys and materials are vastly used in the industry due to interesting thermomechanical properties which are correlated with crystallographic phenomena, as is the case of the aforementioned TRIP steels. These properties can be better understood by *in situ* crystallographic studies, and therefore enhanced, leading to better materials. The second practical motivation comes from the fact that most industry materials go through processing and application under a wide range of temperatures and loads. The application of these conditions can lead to beneficial or undesired consequences on the materials microstructure, such as precipitate formation, creation or relief of residual tension, etc. Observing the evolution of the materials microstructure during these processes leads to more efficient, safer and reliable fabrication and application methods.

On the last few years, advances in detectors, sources and sample stage technologies drove an important increase on the use of *in situ* characterization techniques using photons neutrons and electrons. Each one of these probes allows measurement of different levels of information on different time and space scales. In comparison with the other probes, synchrotron generated X-rays used in diffraction measurements grant data with high time resolution, as well as bulk information, being the most used technique for *in situ* experiments. There are dedicated beamlines for simulation of *in situ* conditions in some of the largest synchrotrons around the world, such as Spring-8 in Japan, ESRF in France and APS in the United States. However, these installations are normally comprised of pre-existing beamlines equipped with sample stages especially suited for *in situ* experiments. In 2008, the Metals Characterization and Processing Group (CPM) from the Brazilian National Nanotechnology Laboratory (LNNano), led by Dr. Antonio Ramirez, started the construction of a scientific installation specifically designed for thermomechanical experimentation with metallic materials, the X-ray Diffraction and Thermo-Mechanical Simulation (XTMS) installation. Given the definite objective of this installation, it is comprised of a powerful and versatile thermomechanical simulator around which an X-ray diffraction experimental setup was built.

The presented work consists on some of the stages of the commissioning of this installation, focused on a scientific perspective. Topics addressed include measurement and analysis methodologies, characterization of the installation as a scientific measurement instrument, and its use in scientific cases demanding different measurement and analysis strategies.

1.1. Justification

The XTMS installation is built around two principles, time resolved diffraction, and simultaneous measurement of sample temperature, diameter, length and other variables. As stated before, this experimental strategy has great potential to provide information on the science behind materials behavior, although it does present important challenges. It is required to understand how these different sample variables are measured and to develop measurement strategies which allow the correlation between such variables and diffraction measurements. Another requirement is to study how to transform the measured variables and diffraction curves in relevant scientific quantities as stress, strain, lattice parameter, phase composition, etc., as well as determining the degree of uncertainty on the determination of such quantities.

As a time resolved X-ray diffraction facility, the XTMS installation produces an overall large amount of diffraction data. This data needs to be processed to allow the determination of more fundamental quantities. With such amount of data this processing requires automation. This automation needs to be developed in a versatile way to allow different processing strategies.

Finally, depending on what kind of thermo-mechanical and crystallographic information is more important in a test, different testing and data analysis strategies must be applied. Three different case studies focusing on different thermo-mechanical phenomena are performed in this work. The first one is based on the observation of the crystallographic behavior of different phases during a stress induced displacive transformation, the second on the observation of diffusive transformation kinetics under several thermo mechanic conditions and the third one on the observation of stress relief during heating. The analysis of each test will focus on different aspects of the collected diffraction data.

1.2. Objectives

The goals of this work include the characterization of XTMS installation as a diffraction instrument, the establishment of a functional and practical measurement strategy which ensures reproducible results, as well as strategies for processing and analyzing data to enable the correct determination of crystallographic quantities.

To achieve these objectives there are three areas of development, the first focuses on the use of the facility, the second focuses on and data processing and analysis, and the third, the application of developed methodologies on case studies.

For the facility use, the topics to be developed are:

- Ensure that sample designs allow the characterization of the studied material through the simultaneous use of the thermomechanical simulator and the X-ray diffraction setup;
- Characterize the facility diffraction measurement capabilities.

For data processing and analysis, the topics to be developed are:

- Development of data processing and analysis software and routines which enable automated processing of collected data;
- Assess the best approach to analysis of diffraction data generated in the facility.

The case studies consist of:

- Identify the phase transformations involved in the plasticity of a stainless steel shape memory alloy;
- Characterize the effect of temperature and stress in the kinetics of phase transformation in a Superduplex stainless steel;
- Detect stress relief during heating through the observation of crystallographic information in a supermartensitic stainless steel.

2. LITERATURE REVIEW

This chapter is divided in six sections. In the first one, the most recent advances in *in situ* synchrotron X-ray diffraction experiments with metallic materials are presented. The objective of this presentation is to show the tendencies used in such experiments in order to conceptualize this work. The next section shows the use of thermomechanical simulators in cases of interest. Later on, reviews on crystallography, X-ray diffraction and phase transformations in metallic alloys are presented. These are of extreme importance in the comprehension and interpretation of the data acquired in the XTMS installation. Finally, a review on the materials studied is presented.

2.1. Synchrotron TRXRD *in situ* Experiments

On the last decades, the use of *in situ* experiments using photons neutrons and electrons as probes has been growing uninterruptedly, as a result of the increase in the complexity of the materials being developed and number of dedicated instruments available to the materials scientist. Specifically, a large number of examples of the use of X rays in *in situ* experiments with metallic materials can be found in the literature, as presented in Figure 2.1 It shows the results of a query taken on Web of Science online platform on 15/07/2014 using search keywords: *in*, *situ,* X, ray, diffraction, metallic, alloys.

In *in situ* experiments using X-rays, setups involving linear or area detectors are mostly used, with the samples being maintained at fixed positions. Such experiments also require a high flux probe, and are mostly done on synchrotrons given that such sources normally have a higher flux than other X-ray sources. This type of experiment is commonly known as time resolved X-ray diffraction (TRXRD), and have been used to follow phase transformations during heating, isothermal and cooling conditions, and in the study of crystallographic changes in metallic sample surfaces under specific atmospheric conditions (DAI et al., 2008; ELMER et al., 2005;

FEUGEAS et al., 1999; KOMIZO; TERASAKI, 2011; ROCHA; HIRSCH, 2005; SANTELLA et al., 2007; ZHANG; TERASAKI; KOMIZO, 2009; ZHANG et al., 2011).

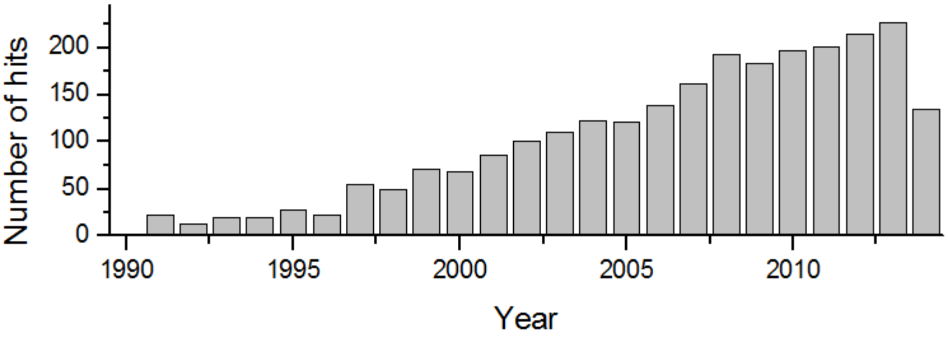

Figure 2.1: Number of search results for the query: *in, situ,* X, ray, diffraction, metallic, alloys. The number of hits was plotted for every year from 1990 to 2014. The query was made on Web of Science online platform on July 15th, 2014.

Following the interest of the materials scientist in *in situ* experiments, beamlines have been modified or equipped with heating sources, reactors or mechanical actuators proper for metallic samples testing. The ID11 beamline at ESRF, for example, has the diffraction setup required for TRXRD as well as accessory equipment to subject the sample to specific thermal and mechanical conditions ("ID11 - Materials science beamline," 2014). In Bessy, an energy dispersive beamline capable of *in situ* heating experiments is available since 2005 (GENZEL et al., 2007), and in APS a high energy X-ray diffraction beamline is also equipped with a range of sample stages allowing thermal and mechanical testing of samples (HAEFFNER; ALMER; LIENERT, 2005).

Those diffraction beamlines are equipped with sample stages specially designed to allow complex *in situ* experiments. Equipment assembly restrictions at beamlines constrain the size and power of these stages, limiting the range of experiments that can be performed On the other hand, the field of thermomechanical physical simulation is familiar to the materials scientist and the metallurgy industry, with powerful and versatile thermomechanical simulators available commercially. The XTMS installation, proposed in 2007, follows a different strategy: building a diffraction experimental station around a thermomechanical simulator. The project was idealized by Antonio Jose Ramirez Londono and funded by the oil and gas company, Petrobras, with the approval of the Brazilian National Petroleum Agency, ANP. Such installation was added to the existing XRD1 diffraction beamline at the Brazilian Synchrotron Light Laboratory, and opened for users on January 2013.

2.2. Physical Simulation

The physical simulation of materials in the XTMS beamline is performed by a custom made Dynamic Systems Inc. Gleeble® simulator. This system is well known to the materials scientist and have been used in the simulation of a variety of metallurgical processes such as welding heat affected zones, stress relief, hot ductility, hot cracking, hot conformation and thermo-mechanical fatigue (FERGUSON et al., 2009; MANDZIEJ, 2010). The Gleeble® system can also be used to achieve singular thermomechanical conditions which allow the activation of specific metallurgical phenomena, one example being its use in the construction of isothermal transformation (TTT) diagrams (XIAO et al., 2005) and continuous cooling transformation (CCT) diagrams (BARCELLONA; PALMERI, 2009).

2.3. Crystallography

According to the classification proposed by the International Union of Crystallography, crystalline materials are materials that "essentially have a diffraction pattern with narrow and intense peaks" (IUCR, 1992). This definition is interesting for its inclusion of quasi-periodic crystals (materials whose atoms are ordered, but not arranged in a three-dimensional periodic fashion), but the majority of crystals have three dimensional periodicity in its atomic arrangement. Only the second group will be treated in this work.

As already mentioned, this second group is characterized by a spatially periodic organization of the constituent atoms or molecules and can be represented as a discrete and periodical space (Figure 2.2).

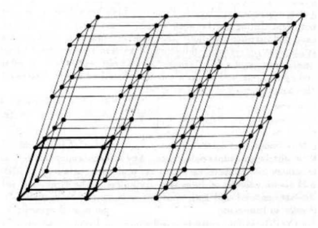

Figure 2.2: Spatial representation of a crystal as a discrete space.

These spaces comply with a number of symmetry operations and therefore it is interesting to classify them according to the operations they respect. There are two basic types of symmetry, the translational symmetries and the point symmetries. Translation symmetries are defined using the Bravais lattices, which are discrete spaces determined by the symmetry operation

$$\mathbf{R}_1 = n_1\mathbf{a_1} + n_2\mathbf{a}_2 + n_3\mathbf{a}_3\,, \qquad \text{Equation 2.1}$$

where $\mathbf{R}_1$ is a vector which, when applied at the origin of the periodical space, gives the position of a point in the space, $\mathbf{a_1}$, $\mathbf{a_2}$ and $\mathbf{a_3}$ are vectors and n_1, n_2 and n_3 are integers. Given the generality of n_1, n_2 and n_3, the origin of the space is arbitrary. Being the numbers, a, b and c the modules of the vectors $\mathbf{a_1}$, $\mathbf{a_2}$ and $\mathbf{a_3}$ respectively, and α the angle between $\mathbf{a_2}$ and $\mathbf{a_3}$, β the angle between $\mathbf{a_1}$ and $\mathbf{a_3}$, and γ the angle between $\mathbf{a_1}$ and $\mathbf{a_2}$, seven primitive lattice arrangements which fill the entire space can be defined based on relationships between a, b, c, α, β and γ:

1. Cubic $a = b = c$, $\alpha = \beta = \gamma = 90\,°$;
2. Tetragonal $a = b \neq c$, $\alpha = \beta = \gamma = 90\,°$;
3. Hexagonal $a = b \neq c$, $\alpha = \beta = 90\,°$, $\gamma = 120\,°$;
4. Orthorhombic $a \neq b \neq c$, $\alpha = \beta = \gamma = 90\,°$;
5. Rhombohedral $a = b = c$, $\alpha = \beta = \gamma \neq 90\,°$;
6. Monoclinic $a \neq b \neq c$, $\alpha = \beta = 90\,°$, $\gamma \neq 90\,°, 120\,°$;
7. Triclinic $a \neq b \neq c$, $\alpha \neq \beta \neq \gamma \neq 90\,°$.

To increase generality, these groups can be associated with one of three additional translation symmetries, which can be separated in three groups:

$$\text{Base Centering: } \mathbf{R}_2 = \frac{1}{2}\mathbf{a}_1 + \frac{1}{2}\mathbf{a}_2, \qquad \text{Equation 2.2}$$

$$\text{Body Centering: } \mathbf{R}_2 = \frac{1}{2}\mathbf{a}_1 + \frac{1}{2}\mathbf{a}_2 + \frac{1}{2}\mathbf{a}_3, \qquad \text{Equation 2.3}$$

$$\text{Face Centering: } \mathbf{R}_2 = \frac{1}{2}\mathbf{a}_1 + \frac{1}{2}\mathbf{a}_2, \mathbf{R}_3 = \frac{1}{2}\mathbf{a}_1 + \frac{1}{2}\mathbf{a}_3, \mathbf{R}_4 = \frac{1}{2}\mathbf{a}_2 + \frac{1}{2}\mathbf{a}_3. \qquad \text{Equation 2.4}$$

A lattice carrying such translational symmetries is known as a Bravais lattice. Lattices carrying only one translation symmetry are known as primitive (P), while those carrying a basic translational symmetry (Equation 2.1) plus one of the translational symmetry operations described in Equations Equation 2.2, Equation 2.3 or Equation 2.4 are called base centered (C), body centered (I) and face centered (F) respectively. Every possible Bravais lattice in three dimensions that fill the entire space can be created either with one of the primitive lattices or by combining each primitive lattice with one of the additional symmetry operations. Since many of the different translational symmetry combinations are redundant, fourteen different Bravais lattices are defined: Cubic (P, I and F), Tetragonal (C and I), Hexagonal (P), Orthorhombic (P, C, I, and F), Rhombohedral (P), Monoclinic (P and C) and Triclinic (P).

These groups define all possible translation symmetries but to completely represent a crystal, other symmetry operations must be defined, such as rotation axes, mirror planes and point symmetries. To do so, point groups are used. A point group is defined as a group of "symmetry operations that maintain at least one point of the space fixed" (HAHN et al., 2005). There are 32 possible point groups in three dimensions. Combining the point groups with the Bravais lattices and excluding redundancies, 230 groups are obtained, called space groups. Necessarily any crystalline phase with periodical atomic arrangement fit in the symmetry description of one of these 230 groups. The space group is identified either by the Bravais lattice plus the point group symmetry operations represented through the Hermann-Mauguin notation, or by a space-group number (HAHN et al., 2005). Armed with the above information it is possible to establish an initial standard classification and description of a crystalline phase.

The primary repeating unit, or asymmetric unit of a crystal, is the set of atoms in which the symmetry operations described by the space group are applied to generate the crystal in space. This set is known as the unit cell. To completely define the unit cell, it is necessary to define the unit cell lattice parameters as the scalars a, b, c, α, β, and γ mentioned above, and then locate the atoms in sites within the unit cell through fractional coordinates ($x|\mathbf{a}_1|$, $\mathrm{y}|\mathbf{a}_2|$, $\mathrm{z}|\mathbf{a}_3|$). The positions of atoms in the unit cell must satisfy the symmetry operations described by the space group. Besides positions, other relevant information are required, as the occupation factor of an atom on a site and its vibration amplitude parameter. Finally, the complete identification of a crystallographic phase occurs when the following parameters are identified:

- Space Group;
- Lattice Parameters ;
- Atomic Parameters (position, occupation and displacement factor).

While several possibilities exist, most metallic solid solutions have one of three crystalline structures described on Table 2.1. They are commonly named through their Bravais lattice instead of their space group, identified as face centered cubic (FCC), body centered cubic (BCC) and hexagonal close packed (HCP). These structures are illustrated in Figure 2.3. Even so, a general representation of crystals is still required in this work given that most precipitates, such as the σ phase in duplex steels (YAKEL, 1983), metallic carbides (FANG; VAN HUIS; ZANDBERGEN, 2009; YAKEL, 1987), and martensitic phases (BHADESHIA, 2001), have more complex structures.

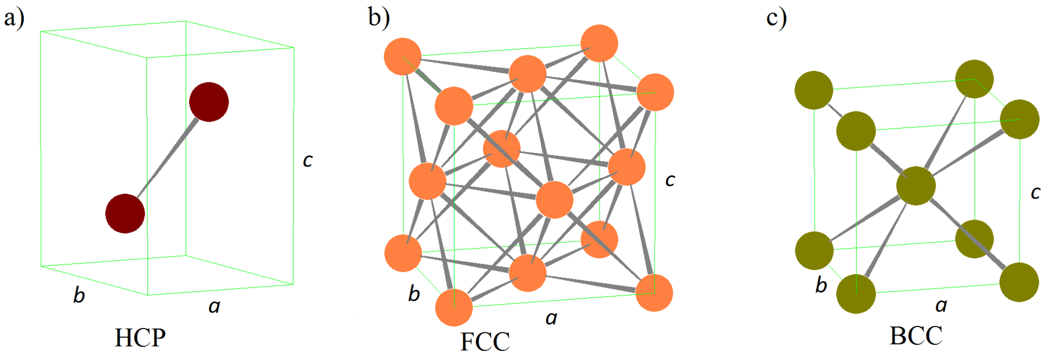

Figure 2.3: Schematic representation of the unit cell of the most common crystallographic phase for metallic solid solutions. The green lines show the unit cell edges. a) HCP, b) FCC, c) BCC.

Table 2.1: Crystalline structure of the most common crystallographic phases for mettalic solid solutions.

FCC structure – space group Fm-3m (#225) – $a = b = c$, $\alpha = \beta = \gamma = 90$ °

Atomic parameters:

Site	***x***	***y***	***z***	**Occupation**	**Atomic Displacement Factor**
Site 1	0	0	0	1	~0.25
Site 2	½	½	0	1	~0.25
Site 3	0	½	½	1	~0.25
Site 4	½	0	½	1	~0.25

BCC structure – space group Im-3m (#229) – $a = b = c$, $\alpha = \beta = \gamma = 90$ °

Atomic parameters:

Site	***x***	***y***	***z***	**Occupation**	**Atomic Displacement Factor**
Site 1	0	0	0	1	~0.25
Site 2	½	½	½	1	~0.25

HCP structure – space group P6$_3$mmc (#194) – $a = b \neq c$, $\alpha = \beta = 90$ °, $\gamma = 120$ °

Atomic parameters:

Site	***x***	***y***	***z***	**Occupation**	**Atomic Displacement Factor**
Site 1	⅓	⅔	¼	1	~0.25
Site 2	⅔	⅓	¾	1	~0.25

To ease interpretation of diffraction measurements, it is interesting to define sets of periodical parallel planes of atoms in the crystal structure. These sets can be identified using the base $\mathbf{a}_i$. Starting from the postulate that one of the planes of a set must intercept the origin of the $\mathbf{a}_i$ base, if the next plane intercepts the axes defined by the base in positions $|\mathbf{a}_1|/h$, $|\mathbf{a}_2|/k$ and $|\mathbf{a}_3|/l$, this set of planes is identified by scalars h, k and l. The distance between two adjacent planes, hereinafter called d-spacing, will be given by Equation 2.5:

$$d = \left| \frac{\mathbf{a}_1}{h} + \frac{\mathbf{a}_2}{k} + \frac{\mathbf{a}_3}{l} \right| . \qquad \text{Equation 2.5}$$

The origin position of the $\mathbf{a}_i$ set is arbitrary, but once defined in a unit cell, it must be repeated in all unit cells to respect symmetry, and if a plane intercepts one origin, it must intercept all. Therefore the maximum distance between two planes is given by $|\mathbf{a}_1+\mathbf{a}_2+\mathbf{a}_3|$, or the distance between two origins. Besides, the number of planes between two origins is an integer, and therefore, h, k and l must be integers. If one plane of a set contains one of the $\mathbf{a}_i$ vectors, the correspondent index is said to be zero. The h, k, and l numbers are known as the Miller indexes (CULLITY, 1956).

As Equation 2.5 does not depend on the number of atoms in the unit cell or their positions, the only important factors for its calculation are the primitive Bravais lattice and the lattice parameters. In this work, it is interesting to define the d-spacing for three Bravais lattices, the cubic, tetragonal and hexagonal ones:

$$\text{Cubic: } \frac{1}{d^2} = \frac{h^2 + k^2 + l^2}{a^2} , \qquad \text{Equation 2.6}$$

$$\text{Tetragonal: } \frac{1}{d^2} = \frac{h^2 + k^2}{a^2} + \frac{l^2}{c^2} , \qquad \text{Equation 2.7}$$

$$\text{Hexagonal: } \frac{1}{d^2} = \frac{4}{3}\left(\frac{h^2 + hk + k^2}{a^2} \right) + \frac{l^2}{c^2} . \qquad \text{Equation 2.8}$$

Throughout this work, concepts like planes, directions and plane families of a given *hkl* set will be referenced. Despite being different concepts, all can be described through Miller indexes. It is interesting to define each one properly, and how they will be shown in terms of notation.

- Plane is a single plane inside the unit cell. It is positioned in the unit cell so that it intercept axes $\mathbf{a}_1$, $\mathbf{a}_2$ and $\mathbf{a}_3$ at $|\mathbf{a}_1|/h$, $|\mathbf{a}_2|/k$ and $|\mathbf{a}_3|/l$, as described three paragraphs above, and identified as (*hkl*);

- Direction is defined by a vector $\frac{\mathbf{a}_1}{h}+\frac{\mathbf{a}_2}{k}+\frac{\mathbf{a}_3}{l}$ constructed in the unit cell coordinate system. It is identified as [*hkl*].

- Plane family identifies all sets of planes with a particular orientation regarding the unit cell. Given the symmetry operations existing in the unit cell, sets of planes with different *hkl* values can belong to the same family as, for example in cubic crystals, where the sets of planes identified by 100, 010, 001, -100, 0-10, and 00-1 all belong to the same family. The number of members in a family is called its multiplicity. Plane families are identified as {*hkl*}.

When working with hexagonal cells, it is common to use four Miller indexes instead of three. Such notation for the hexagonal lattice is called Miller-Bravais. In this notation, the indexes are identified as *h*, *k*, *i* and *l*, where the index *i* is a redundant index lying along the $-(\mathbf{a}_2+\mathbf{a}_1)$ vector. Therefore, *i* is always equal to $-(h+k)$.

2.4. X-ray Diffraction

When an X-ray photon is directed to a material, it will interact with the material component elements in an atomic level. Several types of interaction may happen, but under XTMS experimental conditions, the most probable one will be the elastic scattering of the incident photon by the atom electronic shell, known as Thomson scattering. When the electrons are distributed in space in an ordered periodical fashion, as in a crystal, the photons scattered by different electrons will mostly suffer destructive interference, although in some directions, the spacing between the scattering electrons will be equal to a multiple of the photon wavelength, and in these directions, the scattered X-ray beam will be much more intense than in the surrounding directions due to constructive interference. This phenomena is known as X-ray diffraction (CULLITY, 1956). By observing how the diffracted beams are scattered in space, their positions, intensity and divergence, several conclusions may be drawn on how the atoms are organized in a crystalline material.

In order to indicate how the arrangement of atomic planes is related to the scattered beams in a periodical atomic arrangement, a simple model is proposed in Figure 2.4:

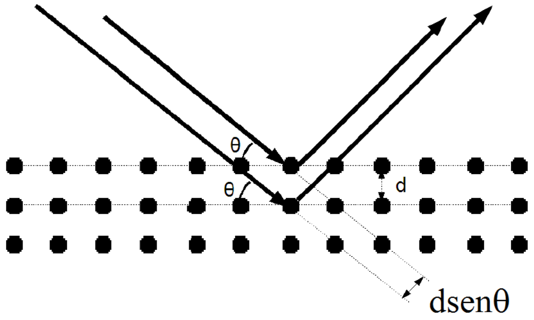

Figure 2.4: Schematic representation of the scattering of an incident X-ray beam by two planes of atoms

The angle between the incident beam and a single diffracted beam can be described by Bragg's Law (CULLITY, 1956):

$$\lambda = 2d \sin\theta \,. \qquad \text{Equation 2.9}$$

In this equation, λ is the incident beam wavelength, d is the spacing between the scattering atomic planes and θ is the angle between the incident beam and the planes, known as Bragg's angle when Bragg's Law is satisfied. Within a single crystalline sample, several different plane sets can diffract, which are identified by the Miller indexes as mentioned in the section above. Despite the orientation relationship between the crystal structure and the incident beam, diffraction may only occur if Bragg's Law is satisfied. If a sample is ideally polycrystalline, there will be a grain oriented in every possible orientation for a 4π solid angle and hence, there will be a diffracted beam whenever possible. Diffracted beams will be distributed in conic surfaces with central axes along the incident beam and opening angles 4θ, with θ respecting Bragg's Law. These are known as the Debye-Scherrer cones.

If these angles are measured, and the incident beam wavelength is known, the values of *d*-spacing can be calculated for each peak. If the crystalline structure and the *hkl* values are known, the lattice parameters can be derived as well.

The intensity of diffraction peaks is dependent on several instrumental and sample parameters, and can be calculated based on the crystalline structure the characteristics of the measuring equipment. If a volume V_p of a certain phase is diffracting, the intensity of a peak originated on a plane family $\{hkl\}$ can be derived from Equation 2.10:

$$I_{p\{hkl\}} = \frac{e^4}{r^2 m_e^2 c^4} \frac{V_p}{v_p^2} M_{p\{hkl\}} \left| F_{p\{hkl\}} \right|^2 P_{p\{hkl\}} A\left(\theta_{\{hkl\}}\right) L\left(\theta_{\{hkl\}}\right) Pol\left(\theta_{\{hkl\}}\right), \qquad \text{Equation 2.10}$$

where e is the electron charge;
r is the distance between the sample and the detector;
m_e is the electron mass;
c is the speed of light;
$\theta_{\{hkl\}}$ is the Bragg's angle for the $\{hkl\}$ plane family;
v_p is p phase unit cell volume;
$M_{p\{hkl\}}$ is the multiplicity factor for the $\{hkl\}$ plane family of p phase;
$F_{p\{hkl\}}$ is the structure factor of for the $\{hkl\}$ plane family of p phase;
$P_{p\{hkl\}}$ is the preferred orientation factor for the $\{hkl\}$ plane family of p phase;
$A(\theta_{\{hkl\}})$ is the absorption factor;
$L(\theta_{\{hkl\}})$ is the Lorentz factor;
and $Pol(\theta_{\{hkl\}})$ is the polarization factor.

In this equation, most factors can be represented by mathematical functions, allowing the establishment of an analytical equation relating the diffracted beam intensity and given values in the list above. For example, the structure factor is described by the equation of an electromagnetic wave corresponding to the sum of the spherical waves scattered by the atoms in the unit cell. Its value squared is equivalent to the intensity of the wave. It can be written as:

$$F_{\{hkl\}} = \sum_{n}^{N} \sum_{a}^{A} o_{an} f_a e^{2\pi i(\mathbf{K}.\mathbf{r}_n)} e^{-M_{an}} \qquad \text{Equation 2.11}$$

where N is the number of atomic sites in the unit cell;

A is the number of different elements present on site n;

o_{an} is the occupation fraction of element a on site n;

f_a is the atomic scattering factor of atom a;

K is the vector (h,k,l);

$\mathbf{r}_n$ is the fractional position of atom a in the unit cell coordinate system;

M_{an} is the atomic displacement factor of atom a at site n;

Depending on the Bravais lattice and atomic positions, $F_{p\{hkl\}}$ may be zero for some **K**s, even through $\theta_{\{hkl\}}$ satisfy Bragg's Law. This is called extinction.

As shown on Equation 2.10, the intensity of the peaks of a phase is proportional to the volume fraction of that phase in the observed volume. Therefore, after disregarding the terms on Equation 2.10 that are constant for all phases and plane families, it can be shown that:

$$V_p \propto \frac{1}{n_{p\{hkl\}}} \sum_{\{hkl\}}^{n_{p\{hkl\}}} \frac{I_{p\{hkl\}}}{R_{p\{hkl\}}}, \qquad \text{Equation 2.12}$$

where

$$R_{p\{hkl\}} = \frac{M_{p\{hkl\}} \left|F_{\{hkl\}}\right|^2 P_{\{hkl\}} A(\theta_{\{hkl\}}) L(\theta_{\{hkl\}}) Pol(\theta_{\{hkl\}})}{v_p^2}. \qquad \text{Equation 2.13}$$

The volume fraction of a single phase on the observed volume can be calculated as:

$$F_p = \frac{V_p}{\sum_p V_p} \qquad \text{Equation 2.14}$$

and therefore

$$F_p = \frac{\frac{1}{n_{p\mathbf{K}}}\sum_{\mathbf{K}}^{n_{p\mathbf{K}}}\frac{I_{p\mathbf{K}}}{R_{p\mathbf{K}}}}{\sum_p \frac{1}{n_{p\mathbf{K}}}\sum_{\mathbf{K}}^{n_{p\mathbf{K}}}\frac{I_{p\mathbf{K}}}{R_{p\mathbf{K}}}}. \qquad \text{Equation 2.15}$$

Similar methodologies have been published in the literature simplifying the above equation for special cases such as austenite and ferrite (CARROUGE, 2002; LEEM et al., 2001), but to analyze other phases, the values of $R_{p\{hkl\}}$ must be calculated for all present peaks of all phases. At least two peaks for each phase must be measured for a good statistical evaluation of phase volume fractions (GNÄUPEL-HEROLD; CREUZIGER, 2011).

Quantification methods such as the Rietveld method use this mathematical approach in order to determine phase volume fractions. However, the application of Rietveld analysis requires specific measurement procedures and specially prepared samples, also requiring the observation of several diffraction conditions (YOUNG, 1993). This diminishes its applicability on the experiments normally performed at the XTMS installation. In addition, while Rietveld method excels in the determination of atomic information inside the unit cell, its use in textured samples is limited (FERRARI; LUTTEROTTI, 1994; GARIN; MANNHEIM, 2005).

Another quantification method, which is empirical, is based on the measurement of a mixture of the material to be analyzed and a known standard phase. If the relative intensity between the observed diffraction conditions of the phases to be quantified and of the standard material is known, the relative phase composition can be defined (SMITH; JOHNSON, 2000). However, this method requires the mixture in a powder form, and its application for polycrystalline bulk materials is limited. Therefore, the phase volume fractions will be calculated in this work by the use of Equation 2.15.

Another important characteristic of diffraction measurements is that the intensity of a single diffraction cone is spread around the Bragg's angle. When the cones are measured along a plane (called diffraction plane), the intensity as a function of 2θ will be distributed in a peak, the center of this peak corresponding to the Bragg's angle. The total intensity will be the peak integrated area minus the background.

In order to measure this intensity numerically, a profile function is fitted to the intensity distribution curve. There are several possible functions yielding different results depending on the sample, experimental conditions, and required analysis. The most commonly used profile functions are Gaussian, pseudo-Voigt, Voigt, and Pearson VII (LANGFORD, 1987).

The diffraction peak profile carries information about the material. Grain size and lattice distortions are the major factors affecting the peak spread. While grain size is a specific quantity, lattice distortions are related to how large the distribution of interplanar spacings regarding the average value is, which can be affected by several different lattice defects. The effect of such defects on the lattice is known as microstrain, which is characterized by short range strain variations in the lattice, as opposed to macrostrain, which correspond to long range homogeneous strain. Figure 2.5 shows a schematic representation of an undistorted lattice, a strained lattice, and a lattice containing microstrain, as well as their effects on diffraction peaks.

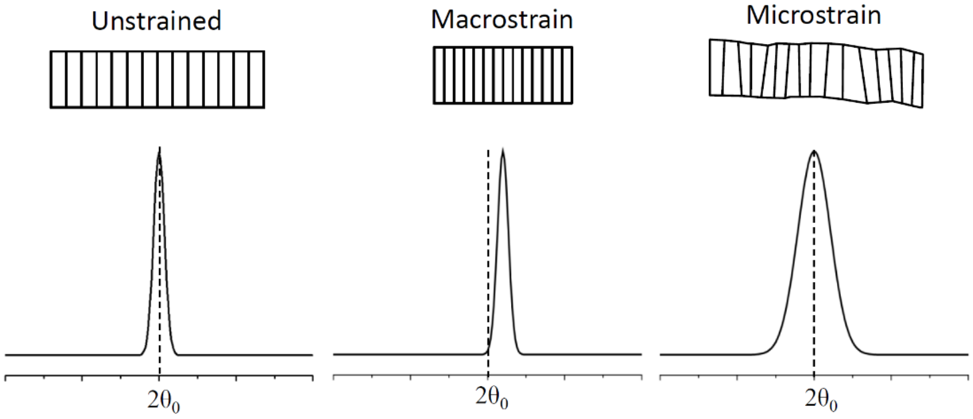

Figure 2.5: Effects of long range and short range strain in a diffraction peak. $2\theta_0$ correspond to the Bragg angle for an unstrained sample.

A comprehensive list microstructural elements causing microstrain includes (KRIVOGLAZ, 1969; UNGÁR, 2004):

1. Dislocations;
2. Stacking Faults;
3. Twins;
4. Grain boundaries;

5. Sub-grain boundaries;
6. Coherency strains;
7. Chemical heterogeneity;
8. Point defects;
9. Precipitates and inclusions.

Table 2.2: Effect of microstructural elements on diffraction peaks. Adapted from Ungár (2004).

Sources of strain	Peak Aberrations				
	Peak shift	Peak broadening	Peak Asymmetry	Anisotropic peak broadening	Peak shape
Dislocations		X	X	X	X
Stacking Faults	X	X	X	X	X
Twinning	X	X	X	X	X
Microstresses		X			
Long range internal stresses	X		X		
Grain boundaries	X	X			
Sub-boundaries	X	X			
Internal stresses	X				
Coherency strains	X	X	X		
Chemical heterogeneities	X	X	X		
Point defects					X
Precipitates and inclusions			X		X

Many of the items in the list above also cause other distortions on diffraction peaks, such as peak shift (as in the case of macrostrain), peak asymmetry, anisotropic peak broadening, and changes in peak shape (UNGÁR, 2001, 2004). Table 2.2, adapted from Ungár (2004) shows the effects of several elements of the microstructure on diffraction peaks. Due to the experimental setup used in this work, peak shape and peak asymmetry cannot be consistently determined through an experiment, and the data analysis will focus on peak shifts, peak broadening and anisotropic peak broadening.

Peak broadening is often determined numerically by a diffraction peak full width at half its maximum value (FWHM). This value will be represented in this text as $\beta(2\theta)$. If $\beta(2\theta)$ is known, crystallite size and microstrain can be determined mathematically.

Crystallite size is inversely proportional to the width of diffraction peaks, i.e., the larger the crystallite size, the narrower the diffraction peaks. The relationship between both is described by Scherrer equation (LANGFORD; WILSON, 1978; SCHERRER, 1918):

$$\beta_{size}(2\theta) = \frac{K\lambda}{L\cos\theta}, \quad \text{Equation 2.16}$$

where *K* is a constant and *L* is the average crystallite size in a perpendicular direction to the measured planes. K varies with crystallite shape, size distribution and profile function used, and is limited from 0.62 to 2.08 (LANGFORD; WILSON, 1978).

The effect of lattice distortions on peak broadening can be evaluated by the partial derivation of Bragg's Law:

$$\partial\lambda = 2\partial d\sin\theta + 2d\cos\theta\partial\theta. \quad \text{Equation 2.17}$$

Dividing both sides by the Bragg's Law yields:

$$\frac{\partial\lambda}{\lambda} = \frac{\partial d}{d} + \cot\theta\partial\theta. \quad \text{Equation 2.18}$$

Treating the partial derivatives as the spread of the measured quantities, and considering a monochromatic beam:

$$\left|\frac{\Delta d}{d}\right| = \cot\theta\frac{\beta_{strain}(2\theta)}{2}. \quad \text{Equation 2.19}$$

Considering that the spread in d spacing caused by lattice distortions can be written as a spread in strain

$$\left|\frac{\Delta d}{d}\right| = 2 < \varepsilon >, \quad \text{Equation 2.20}$$

the strain spread can be correlated to peak broadening as follows:

$$<\varepsilon>=\frac{\beta_{strain}(2\theta)}{4\tan\theta}. \qquad \text{Equation 2.21}$$

Broadening of a diffraction peak will also be caused by the incident beam characteristics and measurement geometry used. The final spread and shape of a diffraction peak will be a convolution of all factors causing the spread. In order to use this spread as a source of information on sample characteristics, the contributions of different factors must be discriminated. Given that the behavior of broadening as a function of 2θ is different depending on its origin, some techniques involving the observation of several peaks on different 2θ angles are able to separate the contributions, such as the Williamson-Hall (WILLIAMSON; HALL, 1953) plot or the Warren-Averbach (WARREN, 1969) deconvolution method. Although useful in most cases, these techniques require the observation of several peaks, and in the case of Warren-Averbach, the observation of peaks of same plane family and different orders. The application of such techniques in experimental conditions where only a small number of peaks are observed is limited. Still, if crystallite size and microstrain contributions to a single peak are orders of magnitude different, the lesser contribution can be neglected. Crystallite size of the phases present in metallic alloys can vary from a few nanometers, such as in precipitates, to hundreds of micrometers, such as in some annealed Ni and Ti alloys. Table 2.3 shows the diffraction peak width caused by several crystallite sizes and several microstrain values.

Table 2.3: Peak broadening due to microstrain and crystallite size. Results were calculated using $K = 1$, $\lambda = 0.1033$ nm, at $2\theta = 30$ °.

Crystallite size	β_{size}(°)		$<\varepsilon>$	β_{strain}(°)
5 nm	1.2		**2.10^{-6}**	0.00012
50 nm	0.12		**2.10^{-5}**	0.0012
500 nm	0.012		**2.10^{-4}**	0.012
5 µm	0.0012		**2.10^{-3}**	0.12
50 µm	0.00012		**2.10^{-2}**	1.2

In this work, microstrain analysis is performed in FeMnSiCrNi SMA and SMSS samples. The average crystallite size in these samples is on the tenths of micrometers both in the SMA (OTUBO et al., 1999) and in the SMSS (ESCOBAR; RAMIREZ; MEI, 2012). Given this crystallite size and the typical observed microstrain of 10^{-4}, $\beta_{size} << \beta_{strain}$, and therefore the crystallite size contribution is disregarded.

Although the contribution from experimental broadening still must be considered, if it's value is known and a Gaussian profile function is assumed for the incident beam intensity profile and for the microstrain distribution, and if a Gaussian function is used to fit the observed peak, the spread contributions from microstrain and the experiment geometry can be deconvolved by the use of Equation 2.22 (ARFKEN; WEBER, 2005):

$$\begin{cases} \beta_{sample}(2\theta) = \sqrt{\beta_{observed}(2\theta)^2 - \beta_{instrument}(2\theta)^2} \\ \beta_{size}(2\theta) << \beta_{strain}(2\theta) \Rightarrow \beta_{sample}(2\theta) = \beta_{strain}(2\theta) \end{cases} . \qquad \text{Equation 2.22}$$

Given the constraints presented by the experimental geometry used in this work, the broadening analysis will be focus on single peak analysis, rather than on whole pattern fitting.

2.5. Phase Transformations

Phase transformations happen when a phase is no longer the minimum possible Gibbs free energy configuration for the material. These transformations can be characterized both by changes in atomic arrangements (such as physical state transitions) and changes in the materials properties (such as magnetic phase transitions). In this work only solid-solid transformations of the former case will be studied. As defined by Doherty (1992), solid-solid phase transformations can be separated in two categories, polymorphous changes and precipitation reactions. In polymorphous changes there is a change in crystal structure, which affects all atoms of the material. Precipitation reactions will happen when some of the atoms dissolved in a phase are no longer soluble. These atoms coalesce forming a new phase until the original phase is not supersaturated anymore.

In both cases, there is a migration of interface between the old phase and the newly formed phase, which is caused by the migration of atoms from one phase to the other. There are two ways for this migration to occur. In the first one, atoms migrate through random thermally activated movements through the phases, in other words, diffusion. If an atom has less energy in a phase than in other, it will probably stay in that phase. If not, it will probably move to the new phase. In the second one the new phase grows in the old one by a shear like movement of all atoms in the interface. The first type of transformation is known as diffusive, while the second one is known as displacive.

In both cases the transformation is driven by a Gibbs free energy reduction from the original to the final atomic arrangement. The Gibbs free energy of a phase can be calculated through Equation 2.23

$$G = U + PV + W - TS \ , \qquad \text{Equation 2.23}$$

where G is the Gibbs free energy, U is the internal energy, P is the pressure, V the volume, W is the work done to the phase, T is absolute temperature, and S is the entropy. In transformations between solid phases the pressure and volume term is much smaller than the internal energy, and can be neglected. In most cases, the work can also be neglected, but since it will be important in some of the experiments reported in this work, it will always be considered.

A phase transformation starts by the formation of nuclei of a new phase. These nuclei can form either inside a grain of the parent phase, where the nucleation is said to be homogeneous, or in grain boundaries, interfaces, lattice defects, free surfaces, etc., where it is said to be heterogeneous. Most nucleation processes in solid-solid transformations are heterogeneous, taking place in sites that locally increase the free energy of the initial phase, like crystalline defects, interfaces or grain boundaries. If a nucleus forms in one of those sites, the local free energy increase will dissipate through the formation of the nucleus and contribute to the free energy reduction. The free energy reduction involved in the formation of a nucleus of volume V is described by Equation 2.24:

$$\Delta G = V\Delta G_V + A\delta + \Delta G_d \, , \qquad \text{Equation 2.24}$$

where ΔG_V is the free energy difference between the parent phase and the newly formed phase, A is the area of the nucleus interface, δ is an interfacial energy term and ΔG_d is the energy released in heterogeneous nucleation. If the nucleation is homogeneous, the value of ΔG_d is zero. In solid-solid transformations, δ varies widely from very low values, in coherent interfaces, and high values for incoherent ones (PORTER; EASTERLING, 1992). As ΔG_V and ΔG_d are negative, for small enough nuclei, $A\delta$ is higher than the module of $V\Delta G_V+\Delta G_d$, and the free energy increases, instead of decreasing. Therefore, these small nuclei are not stable and will dissolve back to the parent phase. Assuming the nuclei are spherical, there is a critical volume in which the ΔG start to decrease, and nuclei with volumes equal or higher than this volume are stable and will continue to grow. The dependence between ΔG and the radius of a nucleus is shown in Figure 2.6.

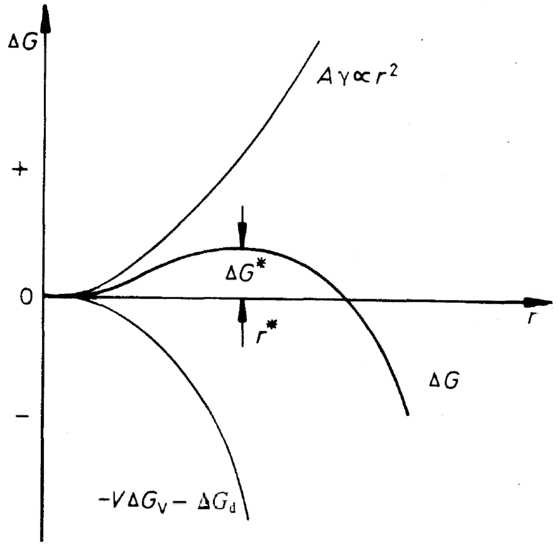

Figure 2.6: Gibbs free energy variation with the radius of a spherical nucleus.

By differentiating Equation 2.24 in radius, the critical radius for the new nuclei will be

$$r^* = \frac{2\delta}{\Delta G_V + \Delta G_d}, \qquad \text{Equation 2.25}$$

while the energy barrier ΔG^* will be

$$\Delta G^* = \frac{16\pi\delta^3}{3(\Delta G_V + \Delta G_d)^2}. \qquad \text{Equation 2.26}$$

If the transformation by which the nuclei are being formed is diffusive, the number of nuclei formed per unit of time N can be calculated through Equation 2.27:

$$N = fC_0 \exp\left(-\frac{\Delta G^*}{kT}\right), \qquad \text{Equation 2.27}$$

where k is the Boltzmann constant, T is the absolute temperature, C_0 is the atomic density of the newly formed phase and f is the rate at which nuclei become supercritical. The term f depends on how many atoms a nucleus can receive per unit time and will be proportional to the area of the nucleus and the rate at which atoms cross the matrix/nucleus interface, in other words, the rate of diffusion.

Diffusion is characterized by a flux of material through a solid solution. This flux can be defined as the vector field **J**, where $|\mathbf{J}(x,y,z)|$ is the mass being transported per unit time through the plane perpendicular to the direction of **J**. The flux will occur in a manner which decreases chemical activity gradients. In most cases, these gradients will be proportional to the chemical composition gradients (SHEWMON, 1989), and **J** can be written as:

$$\mathbf{J} = -D\nabla c, \qquad \text{Equation 2.28}$$

where D is the diffusion constant and c is the chemical composition of a solute in a point in space. D varies with temperature and can be defined by the empirical equation

$$D = D_0 \exp\left(-\frac{Q}{N_a kT}\right), \qquad \text{Equation 2.29}$$

where D_0 and Q are empirical parameters depending on composition, but not on temperature, and N_a is Avogadro's number. Since **J** changes ∇c, **J** itself will change through time. Analytical solutions for **J** as a function of time require several assumptions on the material, and are normally limited to very short time scales. Still, at a single instant, Equation 2.28 is valid.

The flux is also proportional to stress/strain gradients. In a homogeneous material under an inhomogeneous stress field, different regions of the material will have different elastic strain energies, and therefore, a potential energy gradient is created. Atoms solved in the material will tend to move to regions where the potential field is minimal, and therefore **J** will also be dependent on the elastic energy gradient (SHEWMON, 1989), as shown on Equation 2.30:

$$\mathbf{J} = -\left(\frac{Dc}{kT}\right)\nabla W \,, \qquad \text{Equation 2.30}$$

where W is the potential energy, characterized in this case by the elastic energy at a point in space.

Looking back at Equation 2.27, f will be proportional to the value of **J** at the interface between the matrix and a nucleus of a new phase; therefore, the nucleation rate will be proportional to both chemical activity and strain energy gradients. If the transformation forming the new nuclei generates more than one new phase, the equations presented are still valid, but must be calculated independently for each phase.

Looking at Equation 2.27, it can be seen that the kinetics of transformation due to formation of new nuclei gets higher as the temperature is reduced. On the other hand, f gets higher with temperature increase, as can be seen on Equation 2.28 and Equation 2.29. As for stress assisted diffusion, for typical Q values (SHEWMON, 1989), the growth of D with temperature in Equation 2.29 overcomes the inverse temperature term in Equation 2.30. Therefore, stress assisted diffusion also increases with temperature, but not at the same rate as composition gradient diffusion. Comparing Equation 2.27, Equation 2.28 and Equation 2.29, it can be concluded that transformation kinetics is limited by nucleation at high temperatures and by diffusion in lower ones.

As for displacive transformations, these are better described using a phenomenological crystallographic approach (WAYMAN, 1992). As all atoms in the interface go through the same displacement, the new atomic arrangement has a defined orientation relationship with the previous arrangement. The thermodynamics of nucleation in displacive transformations is similar to that of diffusive nucleation, presented earlier, but as in the displacive case the interfaces are coherent, the value for interfacial energy δ is low. Furthermore, considering the nuclei spherical is an unrealistic approximation, whereas highly eccentric ellipsoids are a better model. The nuclei will still have a critical size, and once they become critical, their growth is not dependent on diffusion, but on the speed at which an atomic plane can rearrange itself in the new phase. Therefore, within a single grain, grain growth in displacive transformations happens extremely fast (BHADESHIA, 2001). Still, as nuclei have different driving energies, not all grains transform at the same time.

Most displacive transformations in steels or ferrous alloys happen through the transformation of a FCC Bravais lattice to a BCC, BCT or HCP lattice. The first two cases are fundamentally the same, given that the formation of BCT happens through the trapping of interstitial atoms of the parent phase in specific interstices of a BCC phase. This generates an anisotropic lattice distortion that transforms the unit cell from a cube to a tetragon (BHADESHIA, 2001). The orientation relationships between the crystalline structures of the FCC and BCC or BCT phases can be either described by the Kurdjumov-Sachs or the Nishiyama-Wasserman (NISHIYAMA, 1978) orientation relationships:

Kurdjumov-Sachs: $(111)_{\mathrm{FCC}} \| (011)_{\mathrm{BCC/BCT}}$, $[\bar{1}01]_{\mathrm{FCC}} \| [\bar{1}\bar{1}1]_{\mathrm{BCC/BCT}}$
Nishiyama-Wasserman: $(111)_{\mathrm{FCC}} \| (011)_{\mathrm{BCC/BCT}}$, $[\bar{1}\bar{1}2]_{\mathrm{FCC}} \| [0\bar{1}1]_{\mathrm{BCC/BCT}}$.

In the FCC to HCP transformations, the orientation relationships between the parent phase and the nuclei can be described through the Shoji-Nishiyama relationship (NISHIYAMA, 1978):

Shoji-Nishiyama: $(111)_{\mathrm{FCC}} \| (0001)_{\mathrm{HCP}}$, $[1\bar{1}0]_{\mathrm{FCC}} \| [11\bar{2}0]_{\mathrm{HCP}}$.

The martensitic transformations analyzed in this work are all displacive.

2.6. Materials Analyzed

2.6.1. FeMnSi shape Memory Alloys

Shape Memory Alloys (SMA) are alloys typically composed of two phases, austenite and martensite. At room temperature these alloys normally present metastable austenite or/and twinned martensite. The material studied in this work is part of the FeMnSi family of alloys, in which the austenite phase, also known as γ, has a FCC structure and the martensite, also known as ε, has a HCP structure. When subjected to sufficient stress, the austenite will transform to martensite, or the twinned martensite will become untwined. In both cases, the change in crystalline structure allows a change in morphology, as well as localized stress relief, which reflects in the macroscopic deformation of the material and its plasticity. After this transformation, if the material is heated up to a temperature in which the ε phase is less stable than the γ phase, the martensite structure will transform back to austenite through a reversible crystallographic transformation, and the material will recover its initial shape. When cooled back to room temperature, the austenite may either be retained or transformed, again by a displacive transformation, to twinned martensite, keeping its recovered shape (LAGOUDAS, 2008; OTSUKA; WAYMAN, 1998). Figure 2.7 illustrates this phenomenon.

In the FeMnSi SMA family, the most interesting compositions include Cr and Ni to improve corrosion resistance (OTUBO et al., 1999), but in FeMnSiCrNi SMAs, BCC/BCT martensite (α') may be formed either by γ→α' or ε→α' stress induced transformations. While the γ→ε transformation is reversible and therefore fundamental to the shape memory effect (ARRUDA; BUONO; ANDRADE, 1999; SATO; SUNAGA; MORI, 1977), the martensitic transformations γ→α' or ε→α' are not (JAMES; HANE, 2000), and the strain provided by the α' formation is not recoverable.

Recovery evaluations for FeMnSiCrNi alloys show that the ideal temperature for recovery is about 600 °C (OTUBO et al., 1999), a temperature at which all the ε phase generated through a displacive transformation would have transformed back to γ.

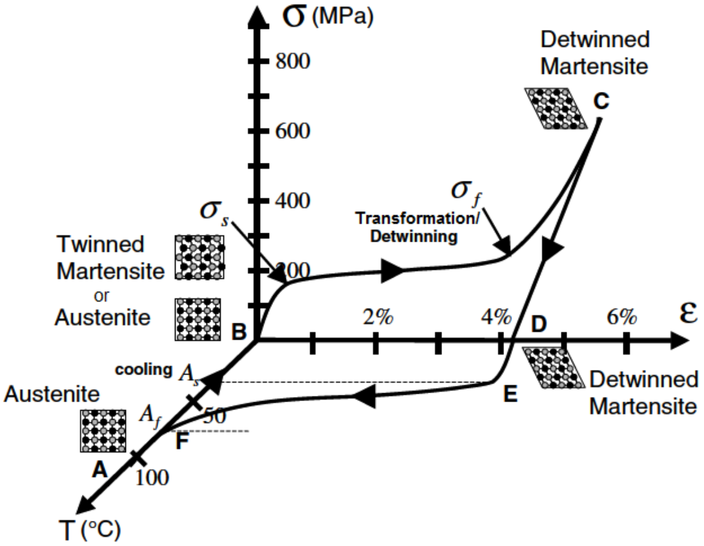

Figure 2.7: Transformations present on the deformation and recovery process on a shape memory alloy. σ is stress, ε is strain and T is temperature. Adapted from (LAGOUDAS, 2008)**.**

2.6.2. Super Duplex Stainless Steel

Duplex and superduplex stainless steels are widely used in the paper, chemical, and petrochemical industries due to their interesting combination of mechanical and environmental performance. The microstructure of these materials consists of a mixture of austenite phase (γ, FCC) and ferrite (α, BCC) (Figure 2.8), which are stabilized by a careful addition of various alloying elements. Such addition leads to a complex phase diagram leading to the potential disadvantage of precipitation of undesirable phases, particularly sigma phase, which forms within the temperature range from 650 °C up to 950 °C (CALLIARI; ZANESCO; RAMOUS, 2006; MICHALSKA; SOZAŃSKA, 2006). At these temperatures, the ferrite phase decomposes through the diffusive eutectoid transformation α→γ*+σ, the α→γ* being a polymorphous transformation and α→σ a precipitation reaction. The σ phase is rich in Fe, Cr and Mo and will nucleate mainly on the α/γ interfaces (ESCRIBA et al., 2009). The γ* is a FCC phase with a different chemical composition from the initial γ, mostly having a smaller Cr content. In similar steels (UNS32205) γ* has been observed both in γ/α interfaces, probably formed through the growth of γ* at a γ grain boundary, and inside α grains, probably nucleating heterogeneously on nitrides(RAMIREZ; BRANDI; LIPPOLD, 2001).

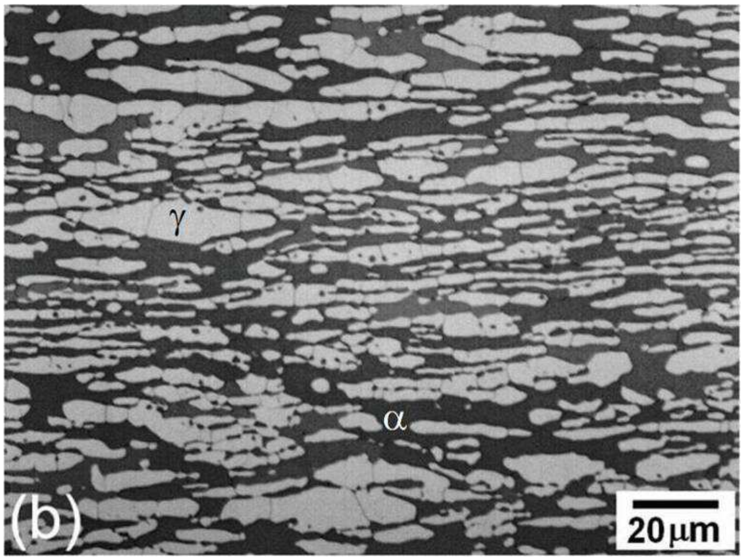

Figure 2.8: Microstructure of the UNS S32750 Superduplex material used in the as received state. Adapted from (SANTOS, 2012)

2.6.3. Super Martensitic Stainless Steel

Supermartensitic stainless steels are low C martensitic alloys of strategic importance for the oil and gas industry due their good corrosion resistance, elevated yield strength with reasonable toughness and improved weldability, when compared with conventional martensitic steels (KVAALE; OLSEN, 1999; LANGE; ROGNE, 2003). From a fundamental point of view, their main feature is their high hardenability, i.e., its propensity to undergo a martensitic transformation induced by temperature during cooling, even at very low cooling rates. In its typical industrial delivery condition, this steel has a martensitic matrix (α' BCC / BCT) with a fraction of metastable austenite, which is achieved through a series of heat treatments (γ FCC) (LANGE; ROGNE, 2003). However, if the material is brought to the fully austenitic condition at high temperature and subsequently cooled, its microstructure will be completely martensitic (KONDO et al., 1999). The formation of martensite can create residual stresses within the material.

3. INSTRUMENTATION, MATERIALS AND METHODS

3.1. Initial Setup

3.1.1. XTMS installation

The experiments reported in this work were all carried out in the XTMS installation, which is currently installed at custom built hutch at the LNLS XRD-1 beamline. The XTMS facility consists of an advanced thermomechanical simulator, specially designed and built to be used for X-ray diffraction experiments. This simulator, called Gleeble® 3S50 was co-developed by the American company Dynamic Systems Inc. (DSI) and the scientific and engineering teams from LNNano and LNLS for the purpose of performing thermomechanical tests on samples of macroscopic dimensions, while simultaneously performing X-ray diffraction and laser dilatometry measurements in order to follow real time phase transformations and other phenomena of interest for materials scientists. Figure 3.1 shows the experimental setup, which is located at the LNLS experimental hall.

The Gleeble® 3S50 simulator allows the application of load, both in compression and tension, and adjustment of sample temperature under a controlled atmosphere, allowing the simulation of complex, dynamic processes. The technical specifications of the simulator are shown in Table 3.1.

Its design was based on the commercially available thermomechanical simulators Gleeble®, which are fabricated and commercialized by DSI. However, this specific simulator was custom designed to allow its use in diffraction measurements. This system has a unidirectional symmetric stroke system to ensure that the sample position illuminated by the X-ray beam does not change in the load application direction due to deformation, as well as a different chamber design so that incident beam can reach the sample and diffracted beams are accessible to detectors.

Figure 3.1: XTMS superior view. The non shaded region shows the experimental hutch.

Table 3.1: XTMS Simulator specifications

Maximum Sampling rate	200 Hz
Thermal testing capabilities	
Maximum heating rate	500 °C/s
Maximum temperature	Sample melting point
Compatible thermocouples	K, J, R, S, T
Maximum cooling rate (Sample T. > 300 °C)	Normal: 70 °C/s
	LN_2: 120 °C/s
Temperature resolution	Type K TC: 0.2 °C
	Type S TC: 1.5 °C
Load testing capabilities	
Maximum Force	44 kN
Force resolution	0.2 kN
Stroke range	200 mm
Stroke resolution	0.01 mm
Laser dilat. range	Initial diameter ± 1 mm
Laser dilat. resolution	0.002 mm

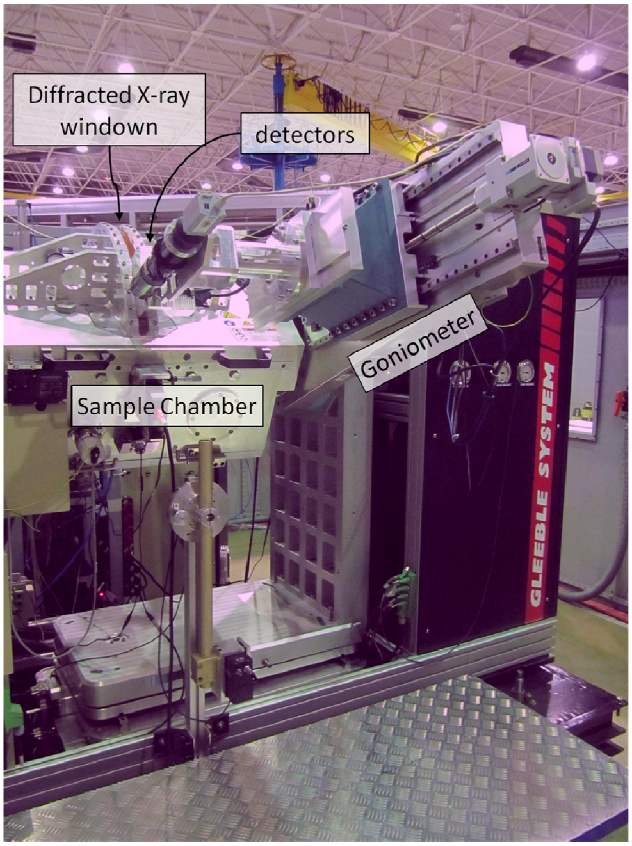

Figure 3.2: XTMS sample chamber and goniometer. Detectors and the diffracted X-ray window are shown.

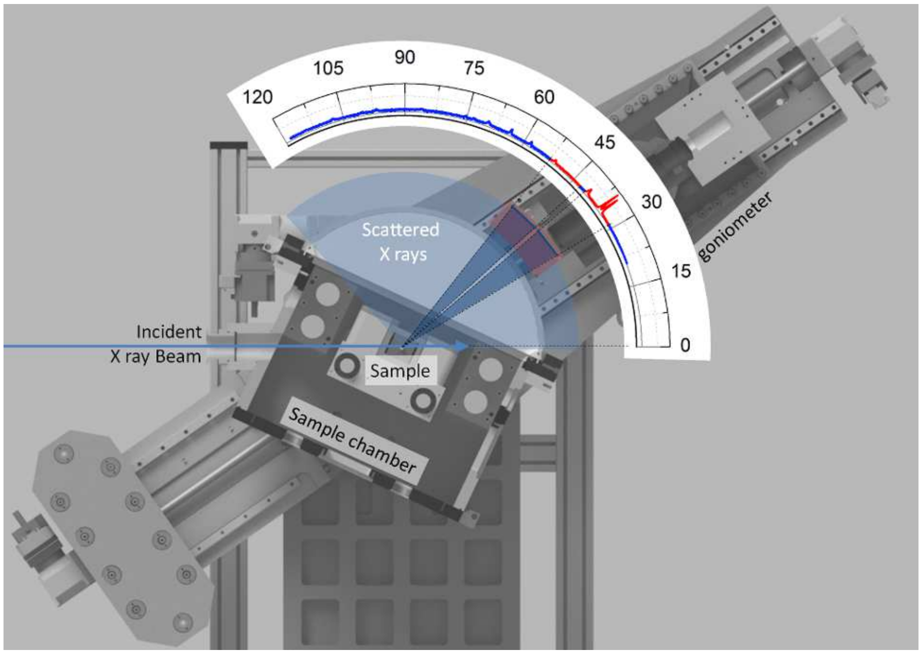

Figure 3.3: Schematic representation of diffraction data collection with a sample loaded in the simulator. The diffraction angular region covered by the actual two linear detectors is highlighted in red.

A high-resolution Huber® goniometer (1.25×10^{-5} °) is assembled around the simulator. The goniometer is built on an alignment table which enables the placement of its diffraction plane turning axis on the sample surface. Figure 3.2 shows the goniometer and sample chamber, while Figure 3.3 shows a representation of the lateral cross section of the simulator with the goniometer assembled around it.The detectors are placed on the red tinted casing and the goniometer allows their positioning at the desired angle regarding the incident beam, as well as adjusting the detector distance from the sample, which grants the choice of best relationship between simultaneously recorded arc and angular resolution. Detectors can be positioned in an angular region from 0 ° to about 150 ° relative to the incident beam. In this work, diffraction measurements were performed using either one or two Mythen1K detectors. These are fast, high efficiency Si based linear detectors with 1024 pixels 50µm wide. Positioned at 361 mm distance from the sample, which is the minimum possible value, each Mythen 1K detector allows the simultaneous measurement of an angular region of about 10 °.

In addition, diffraction measurements can be performed in detector scan mode to acquire data from a wide portion for measuring a wide portion of the diffracted beam. These measurements are not suitable for TRXRD due to the fact that different regions of the diffraction angle are measured at different times, but may be used in situations of thermodynamic equilibrium, or sufficiently slow kinetics, ensuring a more complete observation of the diffraction pattern of the samples. In this text, measurements with the detector fixed are referenced as acquisitions and detector scans through 2θ are referenced as scans. A comparison between the two cases is shown schematically in Figure 3.4**.**

Besides the possibility of TRXRD measurements, the simulator features allow the complementary measurement and control of other test conditions. These include the simultaneous application, control and measurement of sample stress/strain and temperature, as well as other variables such as chamber vacuum, etc. Figure 3.5 shows a picture of the sample chamber with indications on how the facility different components and features interact with the sample.

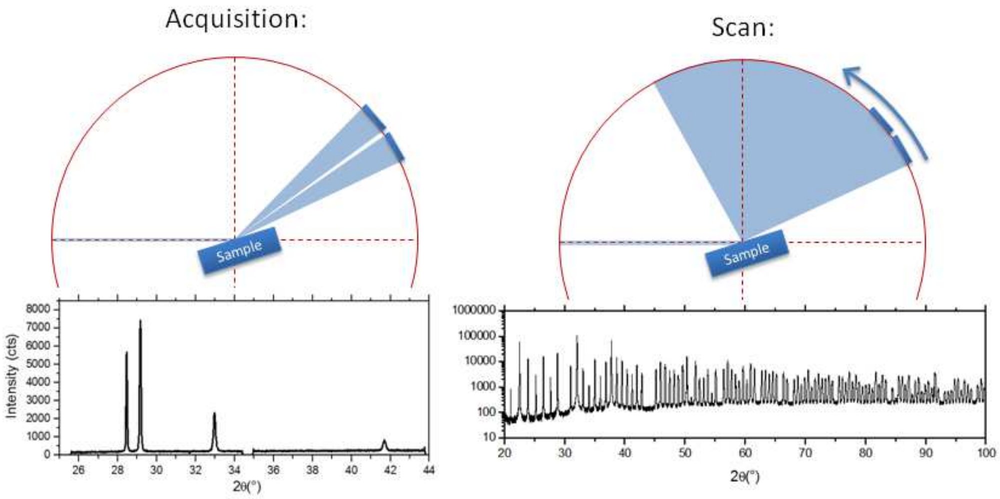

Figure 3.4: Schematic representation of diffraction measurement methods at XTMS. The insets show real measurements made with a superduplex stainless steel sample (acquisition) and a Y_2O_3 sample (scan).

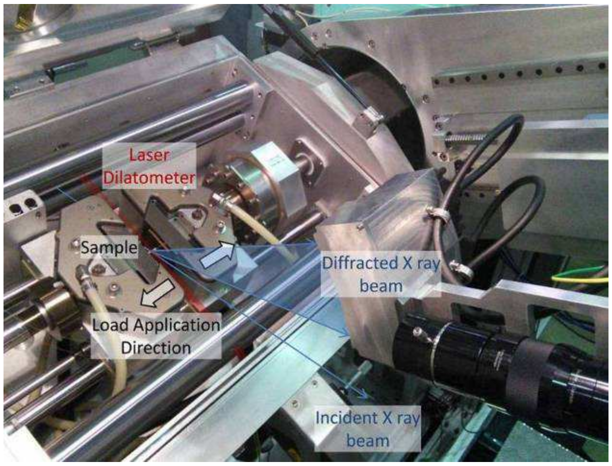

Figure 3.5: Sample chamber. Sample position is shown, as well as a schematic representation of the measurement of X-ray diffraction, dilatommetry, and the load application direction.

Experiment control is based on two computers, one responsible for the thermomechanical simulator and the other responsible for the X-ray detectors, goniometer, incident beam conditioning and equipment positioning, being controlled by the Spec® software. The integration between the two control systems is done by software co-developed by LNNano and LNLS teams with participation from the author, called SyncSim.

A test is programmed in steps, in which the user determines how three control variables should evolve, the sample temperature (PTemp), the mechanical variable, which can be stroke (distance between the jaws), strain (calculated from the stroke or from the specimen diameter, which is measured by the non-contact dilatometer), or load (PRAM), and the diffraction data collection procedure. Figure 3.6 schematically illustrates a test.

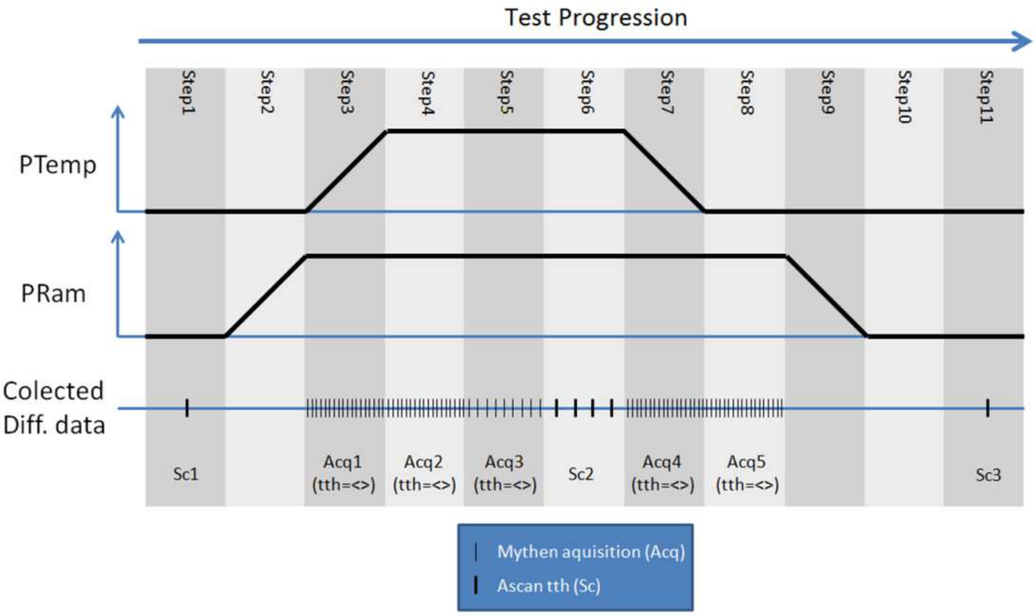

Figure 3.6: Schematic representation of a programmed test on XTMS.

The test is programmed in SyncSim software. This software creates a set of independent commands for each of the control computers with instructions on what must be done in each step. Once the computers receive their instructions, they start the test, collecting data as a function of time. Each computer has an independent clock and therefore, at the end of the test, the data must be synchronized regarding collection time. When the instructions for a step are completed by one of the computers, it sends a message to the other. When both computers receive their messages, both go to the next step. This process is illustrated in the flowchart of Figure 3.7. Controlling the equipment in this fashion ensures that diffraction collection happens at the same time as thermomechanical conditions are acquired.

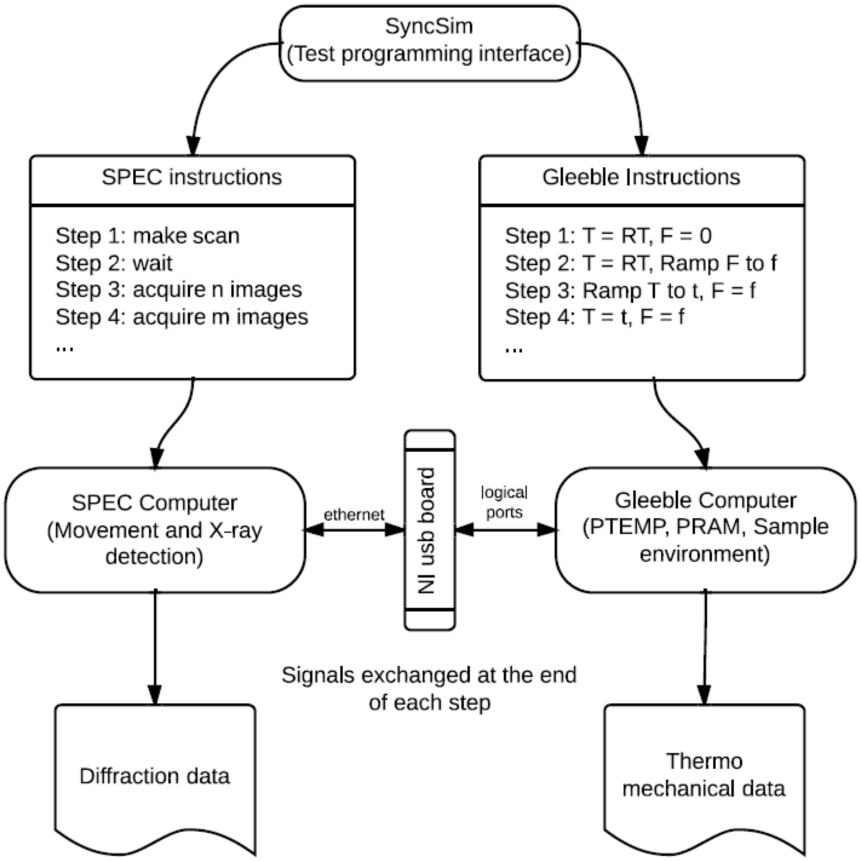

Figure 3.7: Flowchart representing the control of a test.

The data collected by Spec is organized in a three-dimensional structure, the three dimensions being: diffraction angle, intensity, and time. The data collected by the thermomechanical simulator computer is organized in various two-dimensional structures containing the evolution with time of variables such as stroke, strain, force, stress, temperature, etc. As the data recorded by both computers are organized in terms of their internal clocks, if the temporal difference between booth clocks is known, the diffraction and thermomechanical data can be synchronized and correlated.

3.1.2. XRD1 Beamline

The LNLS Synchrotron is composed of a 1.37GeV electron storage ring, working with a typical after injection current of 250 mA. The XTMS installation is located at a specially built hutch at the XRD1 beamline, sharing this beamline X ray beam with a heavy duty powder diffractometer. The XRD1 photon source is a 1.67 T bending magnet followed by optics comprised of a Rh coated silicon X-ray mirror and a double bounce Si(111) monochromator. The optics of this beamline is similar with the ones at other LNLS diffraction beam lines, such as XRD2 (GILES; YOKAICHIYA, 2003) and XPD. The first mirror provides vertical focalization whereas the second monochromator crystal is used for horizontal focalization and beam positioning. The sample position inside the thermomechanical simulator of the XTMS installation is located 17 meters away from the monochromator second mirror.

Energy resolution at the beamline is of 5 eV at 8 keV and the energy range of the beamline covers from 5 keV to 14.5 keV. The focalized X-ray beam size at the sample position has a full width at half maximum of 3.6 mm horizontally and 1.2 mm vertically. The beam intensity profile at typical working conditions is shown on Figure 3.8. Focalization can be adjusted to obtain a shorter and wider beam. In addition, XTMS is equipped with motorized incident beam slits which allow for smaller beam size selection, at the cost of reduced flux. Figure 3.9 shows the photon flux at the sample position for the energy range available at the beamline.

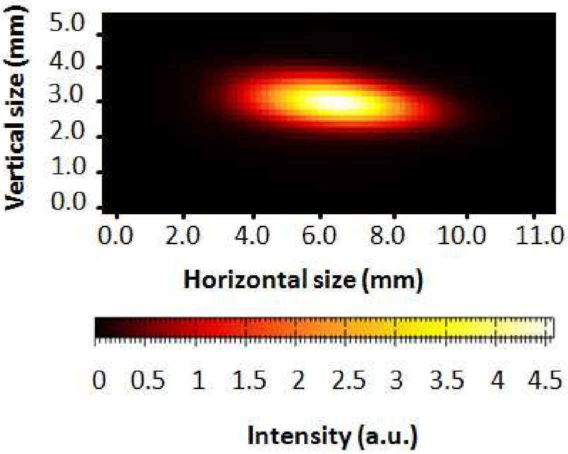

Figure 3.8: X-ray beam intensity profile at sample position. Measurement was done with a Pilatus 100K detector at 10 keV incident beam energy.

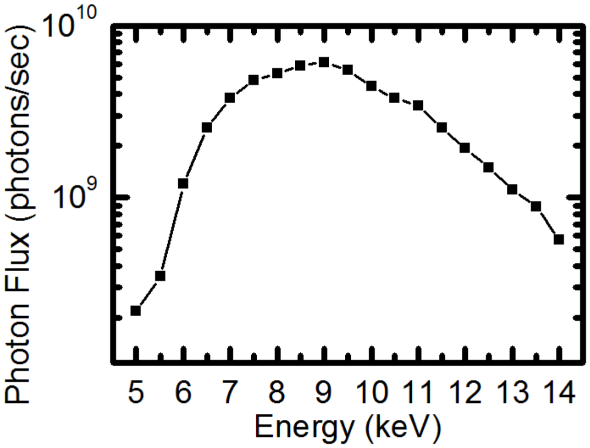

Figure 3.9: **Photon flux at the sample position as a function of energy. Counts were collected with a photodiode, with the beam at maximum possible focalization, without slits.**

3.2. Materials and Procedures

3.2.1. Installation Commissioning and Characterization

High quality crystalline oxide powder samples, Y_2O_3 and CeO_2, provided by the Brazilian Institute of Nuclear Energy Research (IPEN), were used to commission and evaluate the installation. These samples exhibit little lattice distortion along the grains, with a low Δd/d value, and a large enough size so that peak broadening by the sample can be disregarded. Hence these samples are appropriate for measurements of peak position and instrumental broadening. Table 3.2 shows the crystallographic properties of these materials, measured at the XPD beamline at LNLS.

Table 3.2: **Standard samples used in the characterization of the diffraction measurements done at the installation.**

Standard sample	Lattice Parameter (Å)	Crystallite average size (Å)	Space group (ITC #)
Y_2O_3	a = 10.604193(6)	3447	Ia-3 (206)
CeO_2	a = 5.41147	6147	Fm-3m (225)

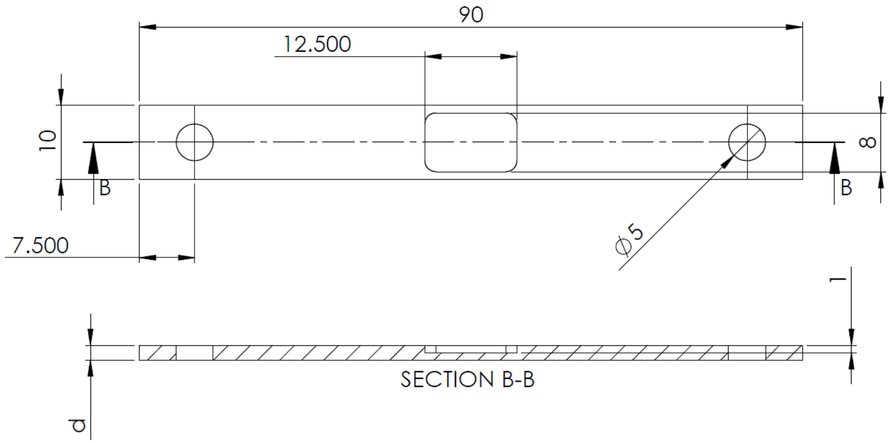

Figure 3.10: Sample holder design for standard powder samples. The powder is deposited in the central cavity. Dimensions are shown in mm. d is either 2 mm or 5 mm.

The standard samples are positioned on a sample holder that mimics the typical design of tested metallic samples (Figure 3.10). The sample alignment and measurement procedures are reproduced in the installation with the standard samples to check the quality and accuracy of the diffraction data collected according to the acquisition and scan methods.

3.2.2. Stress Induced Phase Transformation Study in Shape Memory Stainless Steels

The shape memory stainless steel studied is an experimental SMA developed by Prof. Dr. Jorge Otubo from the Brazilian Technological Institute of Aeronautics (ITA). The starting material is obtained as bars with a 10.25 mm diameter. The chemical composition of the samples is shown in Table 3. The alloys are processed by hot rotary forging until reaching a final diameter of 7.6 mm. The obtained bar is solubilized at 1050 °C for 40 minutes and water quenched, and then machined to the shape of specimens used (Figure 3.11). The sample surface used in the diffraction measurements is ground up to a granulometry 1200 in order to remove the layer strained by the machining process. Previous characterizations of similar alloys under similar tests show a grain size distribution around tenths of microns (OTUBO, 1996).

Table 3.3: Chemical composition of the shape memory stainless steel used. Composition is shown as mass percentage.

%Fe	%Mn	%Si	%Cr	%Ni	%C
balance	14.2	5.3	8.8	4.65	0.008

The performed experiment consisted of a strain test up to 0.04 at a strain rate of 0.0001666/s. The energy used in the incident beam was 10 keV. During deformation, diffraction data was collected in the 2θ region between 32 ° and 42 °, where the most intense peaks of the present phases in the material are located. 16 acquisitions, each with 15 second exposure, were made. Before and after deformation 2θ scans from 27 ° to 117 ° were collected.

The Sample was then submitted to a shape recovery cycle, in which it was heated up to 550 °C at a rate of 0.166 °C/s, kept at this temperature for 600 s and then cooled to room temperature at the same rate. Diffraction data was not collected through this cycle. Stress, strain and temperature were measured through the whole test at an acquisition rate of 20 Hz.

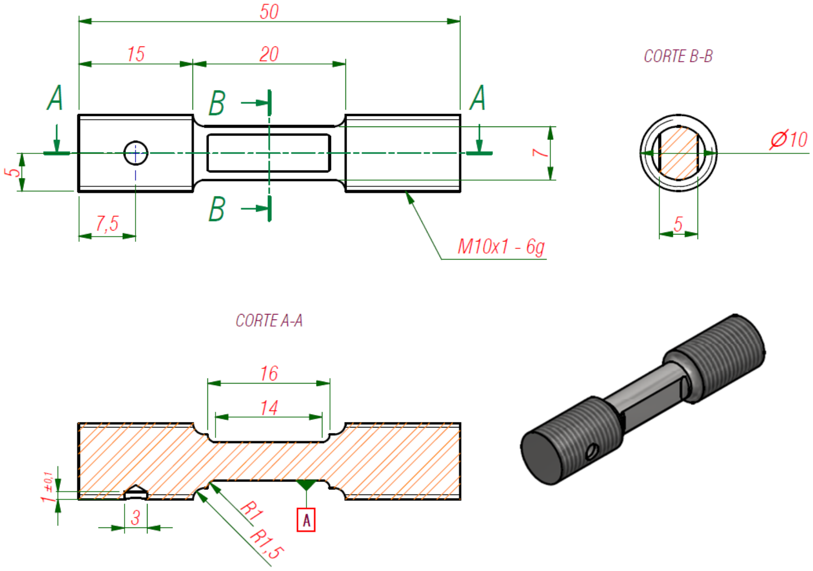

Figure 3.11: Specimen design used on the shape memory stainless steel samples. Dimensions are shown in mm.

3.2.3. Ferrite decomposition Study on Superduplex Stainless Steel UNS S32750

The ferrite decomposition study in superduplex stainless steels (SDSS) UNS S32750 was conducted in commercial 6 mm thick plate donated by Outokumpu, with chemical composition shown in Table 3.4, as provided by the manufacturer. Samples were machined following the design shown in Figure 3.12. The surface used for diffraction was sanded up to 2000 granulometry and polished with 1µm diamond paste. Previous characterization of the same alloy shows an average grain size of 10 µm (SANTOS, 2012).

Table 3.4: Chemical composition in weight percentage of the Super Duplex stainless Steel UNS S32750.

%Fe	%C	%Si	%Mn	%Cr	%Ni	%Mo	%Cu	%N	%P	%S
balance	0.02	0.25	0.78	24.9	6.88	3.79	0.34	0.26	0.023	0.001

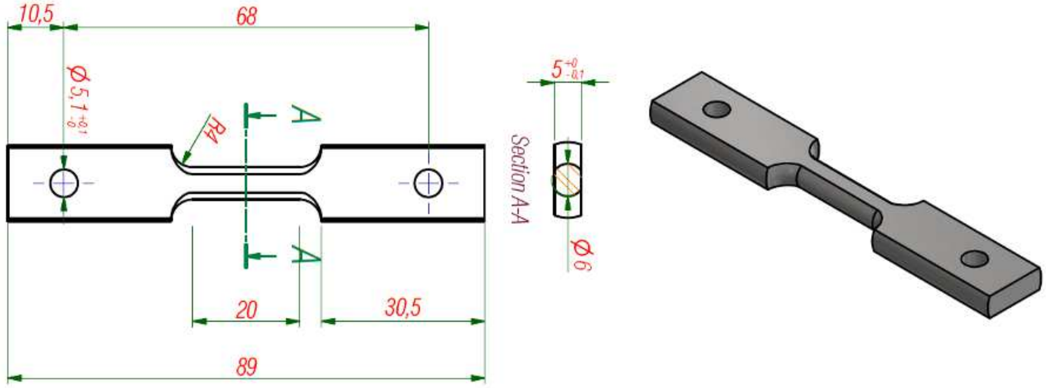

Figure 3.12: Specimen design used on the Super Duplex stainless Steel samples. Dimensions are shown in mm.

Five specimens were used to obtain stress strain curves at temperatures of 700 °C, 750 °C, 800 °C, 850 °C and 900 °C. These specimens were heated up to the test temperatures at a 100 °C/s heating rate and strained at a 0.0033/s (0.2/min) strain rate. From the curves, the yield strength of the material at the tested temperatures was derived. Following, ten tests consisting of the same methodology were made: The samples were heated to the test temperature at a 100 °C/s rate, and kept at this temperature until complete ferrite decomposition occurred. Since decomposition kinetics is different depending on temperature, the plateau duration was different for each temperature. The samples were then rapidly cooled to room temperature. The incident beam energy was 10 keV. During the high temperature plateau, diffraction data was continuously collected in the angular region from 32 ° to 42 °. Acquisition rate changed throughout the test, being initially one acquisition every 5 s at the first eighth of the plateau, one acquisition every 15 s until the half of the plateau, and one acquisition every 30 s until the end of the plateau. Two tests were done for each temperature, one with the sample under load and the other with the sample free of force. Due to possible sample creep, force rather than stress was used as the mechanical control mode. Forces used corresponded to fractions of the yield stress. At higher temperatures, the fractions were lower to avoid or minimize creep. The temperatures, stresses and plateau duration times used are shown on Table 3.5:

Table 3.5: Isothermal ferrite decomposition test conditions.

Test Temperature (°C)	Applied Load (MPa)	Yield Strength percentage	Plateau duration (s)
700	0	0	10800
	240±8	100±3%	10800
750	0	0	7200
	200±8	100±4%	7200
800	0	0	2400
	120±8	75±5%	2400
850	0	0	3600
	80±8	70±7%	3600
900	0	0	7200
	40±8	40±8%	7200

3.2.4. Phase Transformations and Stress Relief on Supermartensitic Stainless Steel SuperCr13

The used supermartensitic stainless steel SuperCr13 was supplied by Villares Metals as hot rolled and annealed sheets. The chemical composition measured is shown in

Table 3.6. Samples were machined according to the design shown in Figure 3.13, then austenitized at 1050 °C for 30 minutes and air-cooled. The surface used for diffraction was sanded up to 2000 granulometry and polished with 1μm diamond paste. Previous characterization of the same alloy shows a grain size of 10 μm (ESCOBAR, 2013).

Table 3.6: Chemical composition in weight percentage of the Supermartensitic stainless Steel SuperCr13.

%Fe	%C	%Si	%Mn	%Cr	%Ni	%Mo	%N
balance	0.024	0.26	0.48	12.02	5.9	1.93	0.0129
%P	**%S**	**%Ti**	**%Nb**	**%Cu**	**%W**	**%V**	
0,027	0.002	0.13	<0.02	0.09	<0.05	0.04	

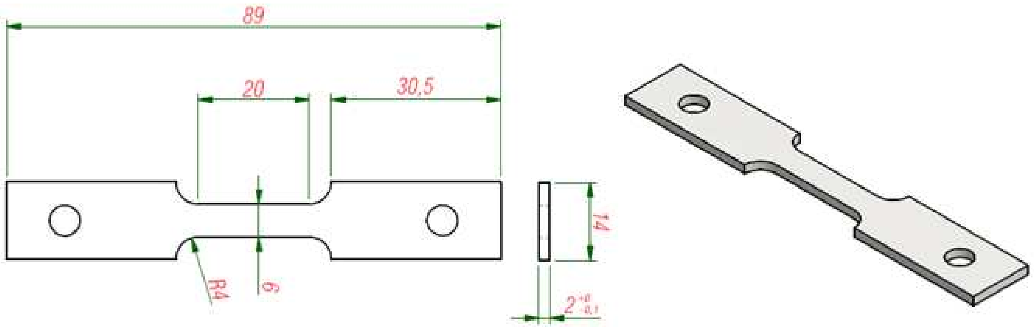

Figure 3.13: Specimen design used on the Supermartensitic Stainless Steel samples. Dimensions are shown in mm.

The performed test consisted of a quasistatic heating and cooling curve, both at a rate of 0.166 °C/s (10 °C/min). Heating went from room temperature to 950 °C, immediately followed by cooling to room temperature. The aim of the experiment was to compare dilatometry and diffraction data taken simultaneously. However, the results obtained allow the observation of residual stress relief by heating. The incident beam energy was 12 keV, and acquisitions were continuously collected every 5 s. Two Mythen 1K detectors were used, and diffraction data was collected from 2θ = 24.3 ° to 34.3 ° and 34.8 ° to 44.8 °.

3.3. Software Platforms Used

During the work, software and routines were developed on different platforms. The platforms used in different stages of this work were:

- Data processing: MSExcel©, Matlab© and IgorPro©;

- Data analysis: XPert HighScore Plus© and IgorPro©.

The routines were programmed in different languages depending on the platform used. In platforms Matlab© and IgorPro© the dedicated programming languages were used. Visual Basic© and Pascal languages were used along with MSExcel© and XPert HighScore Plus©, respectively used.

4. RESULTS AND DISCUSSION

4.1. Sample Design for XTMS Installation

Samples are assembled on the Gleeble 3S50© through a set of steps which grants high control on strain tests while also allowing the application of high electrical currents. Each sample side is placed between two copper or stainless steel fittings, which are then encased in steel frames, and finally set on the simulator jaws. The simulator, as delivered by DSI, had fittings which offered several possibilities in the sample cross section, as cylindrical, rectangular (flat bars) and square. Square fittings do not allow the selection of the angle between the incident beam and the sample surface, which, for reasons presented later, is important in the adjustment of diffraction geometric parameters. In order to allow this selection, a fitting system was developed by the XTMS developing team at LNNano with participation of the author, which is composed by four parts in each side of the sample: Two parts are fixed relative to the steel frame, and two can revolve around the load application direction, all fitting together through conical adjustments (Figure 4.1). In addition a pin warrants for the axial load to be transferred to the sample, avoiding its sliding between the grips. The main advantage of this system is that the fixed and revolving fittings have angular scales, allowing angular adjustment with a resolution of 0.5 °. However, the maximum axial force this system can hold is about 10 kN.

If cylindrical fittings are used, this angle can also be adjusted, as well as being able to hold up to 40 kN force, although they have the issue of requiring large amounts of material for samples, which limits their application for experimental alloys, such as the shape memory stainless steels here studied. Therefore, a second fitting design was developed, based on appendixes that allow using the sample design shown on Figure 3.11 with cylindrical fittings. This fitting is shown on Figure 4.2.

Both systems allow the rotation of samples around the axis that intersects the geometric center of the sample cross section and is parallel to the load application direction. The discussions on sample design and measurement geometry were always conducted considering these fittings, whereas the presented results were obtained using them.

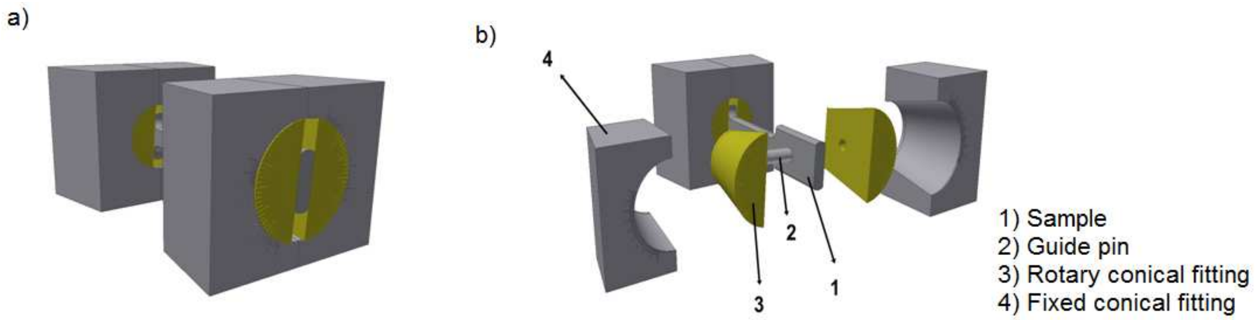

Figure 4.1: **Conical rotary fitting system. a) shows the sample positioned on the system in the way it would be assembled in the simulator. b) shows an exploded view identifying the composing parts.**

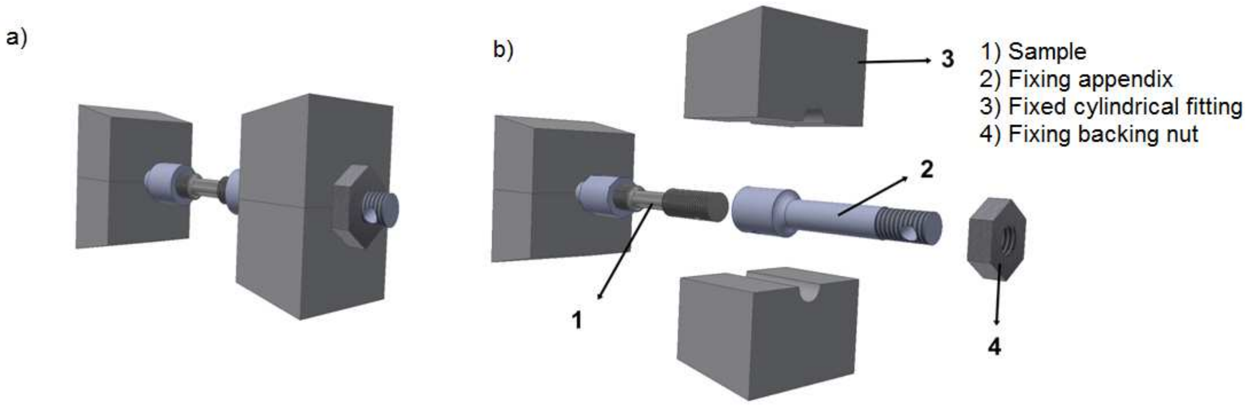

Figure 4.2: **Cylindrical fitting system with appendixes. a) shows the sample positioned on the system in the way it would be assembled in the simulator. b) shows an exploded view identifying the composing parts.**

Regarding samples, most standardized sample designs have either a circular or rectangular cross section (ASTM E 8M, 2013). Both cross sections have disadvantages concerning the requirements of a reliable simultaneous stress and diffraction measurements. The circular cross section is very limiting in terms of diffraction. In a measurement taken in such a sample, the minimum measurable angle is defined by the angle in which the entire irradiated sample region is contributing for a diffraction peak (Figure 4.3). For smaller angles, there still would be intensity, but beams originated in some irradiated regions would have to cross a large distance through the sample, being highly absorbed, and would not contribute to measured intensity. The minimum acquisition angle is determined by the sample surface tangent at the point in which the incident beam's lower edge hits the sample. If the sample has a radius r, the incident beam has a vertical thickness w, and the incident beam center axis is a distance h lower than the sample surface along the vertical direction (as drawn on Figure 4.3), this angle can be calculated using Equation 4.1:

$$2\theta_{\min} = \frac{\pi}{2} - \sin^{-1}\frac{r - h - \frac{w}{2}}{r}. \qquad \text{Equation 4.1}$$

Considering a set of reasonable experimental values for these three variables such as h = 0.75 mm, w = 1 mm and r = 3 mm, the minimum diffraction angle would be 54 °, which is higher than the most intense peak positions for typical FCC, BCC and HCP metallic crystalline structures if an incident beam energy of 8 keV is used. Besides, other complications arise, such as asymmetries in the diffracted beam and different incident beam absorption for each irradiated sample position at each diffraction angle.

On the other hand, the rectangular cross section samples, pose a challenge for stress measurement. Within the XTMS installation, stress and strain are calculated based on the laser dilatometer measurement. Such system measures the sample projection normal to the laser propagation direction. Figure 4.4 shows a schematic representation of a square sample with the incident X-ray and laser beams.

The laser measurement can be correlated with the sample cross section area if the angle φ is known, but slight variations in φ can lead to large variations in the calculated area. If it is assumed that the strain distribution on the sample is homogeneous, strain determination is independent on the sample area and can be calculated solely by the variation of the laser measurement. Stress, on the other hand, requires the knowledge of sample area. Using the fitting systems presented earlier, a change in the X-ray beam incident angle also changes φ. The resolution in the determination of this angle is limited, and therefore the calculated stress resolution is also limited.

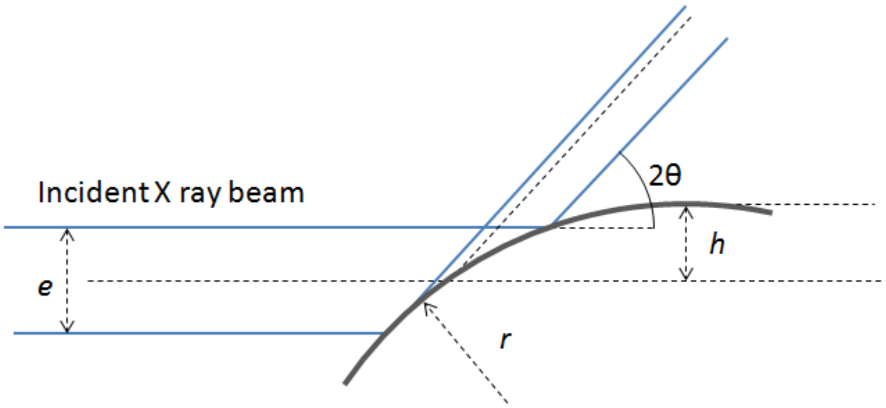

Figure 4.3: Schematic representation of an X-ray beam diffracted by a round sample.

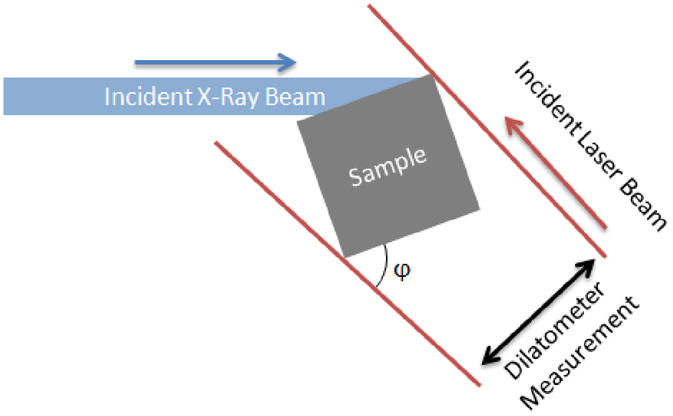

Figure 4.4: Schematic representation of a rectangular sample being irradiated by an incident X-ray beam and measured by laser dilatometry simultaneously.

To overcome the limitations with square and circular cross sections, a hybrid design was developed. This basically consists of a cylindrical body with parallel and symmetric flat surfaces. An illustration of a hybrid sample is shown on Figure 4.5. The sample sides on Figure 4.5 are compatible with the conical fittings, but designs compatible with the cylindrical fitting system can also be used, provided that the sample cross section at its center is kept the same.

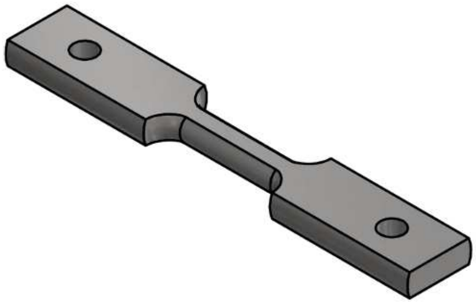

Figure 4.5: Hybrid sample design for the XTMS installation.

The main idea behind this design is that the incident X-ray beam hits the sample in a flat surface while the laser hits its cylindrical sides. This allows the calculation of stress to be independent of angle φ, but since the angle between X-ray and laser beams is fixed, this independence only holds for incident X-ray beam angles above a certain value. For angles below this value, the laser measurement would be done from the flat surfaces edges, and the dependence would exist again. For a sample cross section with 3 mm circular radius and 5 mm thickness between the flat surfaces the minimum angle of incidence would be ~8.5 °.

Even so, the determination of stress at the X-ray irradiated volume can only be made if the strain field is homogeneous. In order to make assertions over this homogeneity, finite element calculations were performed in a sample with the design shown in Figure 3.12 using a mesh interval value of ~1μm. The calculations were done by Vinicius Mastelaro Rodrigues from CPM-LNNano using Consol™ software. The material simulated properties were based on the stress strain curve from a FeMnSi SMA, shown on Figure 4.6, using a 0.33 Poisson ratio. Figure 4.7 shows the results for an applied tension of 500MPa. The strain tensor ε_{11} component in the sample cross section is shown in a color scale.

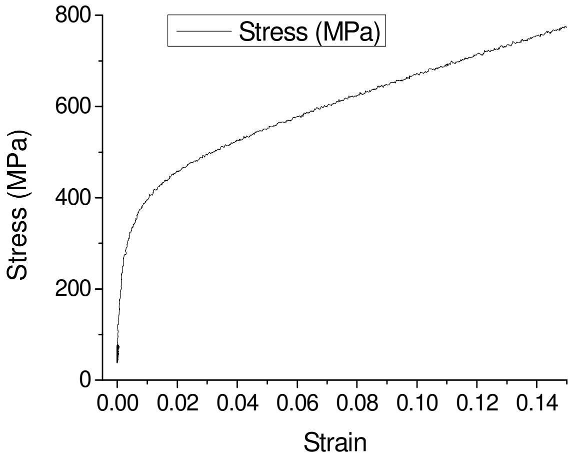

Figure 4.6: stress strain curve used in the strain field finite element calculations on hybrid design samples.

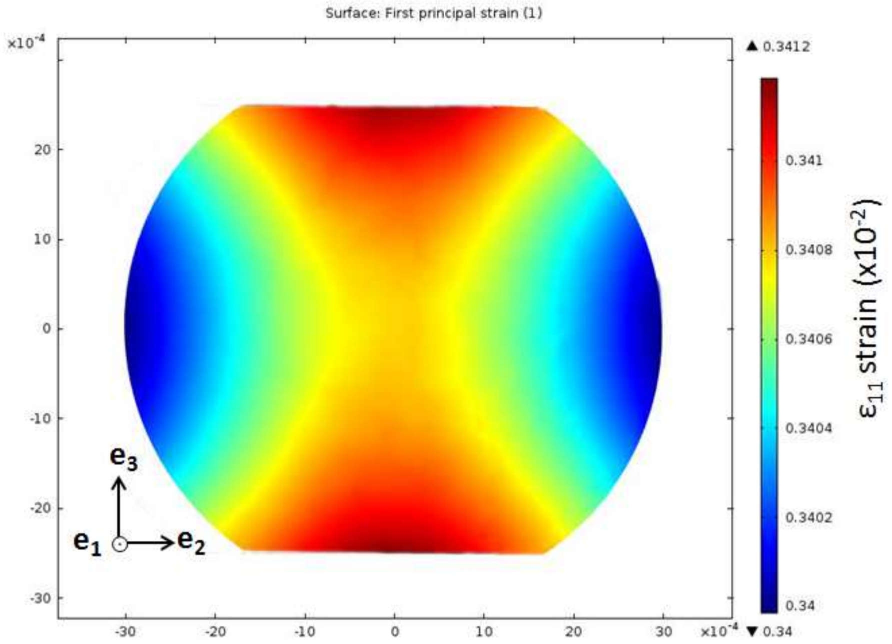

Figure 4.7: ε_{11} strain field component at the sample cross section, when under 500MPa tensile stress, as calculated by finite element method.

As displayed on Figure 4.7, there is an inhomogeneity in the strain field, although looking at the scale, the maximum variation is ~10^{-5}. For this sample design, this difference is negligible if compared to the simulator strain resolution. Therefore, for practical effects, the strain field can be considered homogeneous. Despite its small mesh interval, this simulation does not account for variations in mechanical properties through the sample body. In real samples there will be larger inhomogeneities on the strain field based on microstructure variations and crystallite orientations.

Another important consideration is the temperature gradient at the sample irradiated region. In the simulator, the grips that hold the sample are in most cases kept at ~25 °C. As stated before, sample temperature is controlled through the passage of an electrical current, adjusted so the sample region where the thermocouple is attached reaches the programmed temperature. Therefore, a thermal gradient exists along the free span between these grips, with a maximum temperature at the sample center.

Defining the length of the sample region in which its cross section area has a minimum value as the reduced cross section length, the shorter the value of this length, the steeper the thermal gradient will be. Given that the incident beam FWHM in the horizontal direction is around 3 mm, the reduced cross section length must be set so that the temperature variation in a region ±1.5 mm around the sample temperature control point is low enough that it won't affect diffraction data. This temperature gradient can be made less steep by correct combination of sample design, grips material and even peak temperature. Given the typical metallic alloys thermal expansion coefficient and the available resolution in the diffraction measurements done at the XTMS facility, the irradiated region ideally should have less than 10 °C temperature variation. In order to verify that, measurements were made in UNS G10200 steel samples with three different values for the reduced cross section length, 15 mm, 20 mm and 25 mm. Three type K thermocouples were welded in each sample, one at its center, which was used to control temperature, and the others spaced 1.5 mm at each side of the central one. The samples were heated up to 900 °C at a 0.166 °C/s rate. The difference between the control temperature and the mean value of the temperatures measured by the other thermocouples was calculated for the three samples, and is shown on Figure 4.8. As observed on this Figure, in order to minimize the thermal gradient, it makes sense to use the highest possible reduced cross section length value, but the higher this length, the lower will be the simulator maximum possible cooling rate without having to use forced cooling using inert gas or LN_2. To verify these rates, the same samples were heated to 1300 °C, and let cool down freely with no passage of current. Figure 4.9 shows the temperature as a function of time for the three samples.

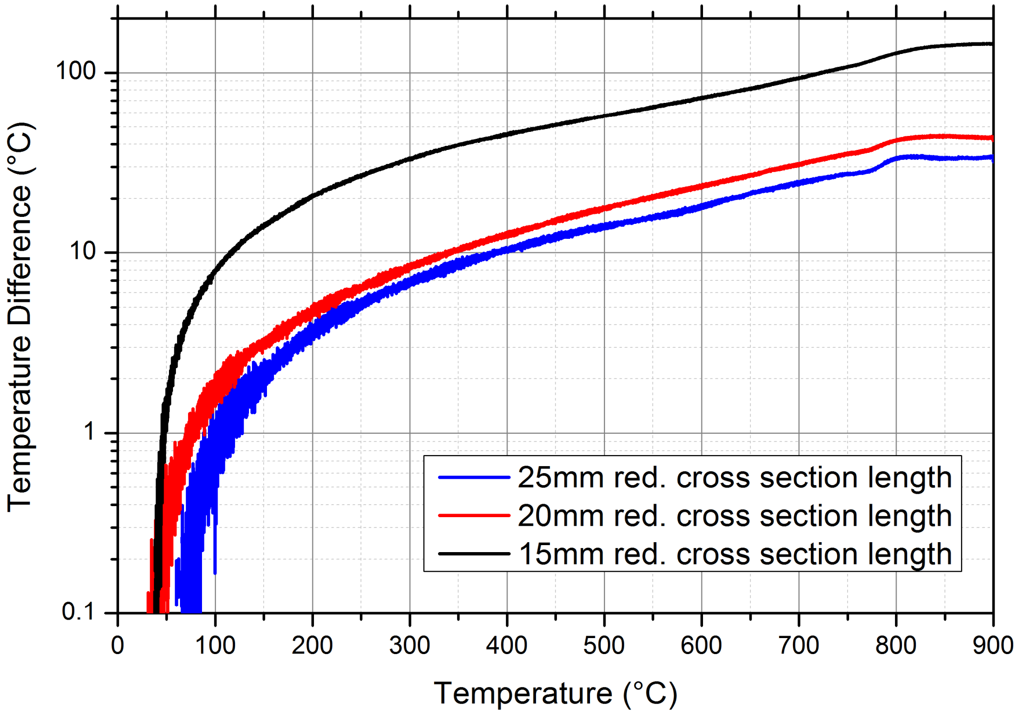

Figure 4.8: **Difference between the temperatures at the control point and at ±1.5 mm, plotted as a function of control temperature. Results are plotted for various sample reduced cross section lengths.**

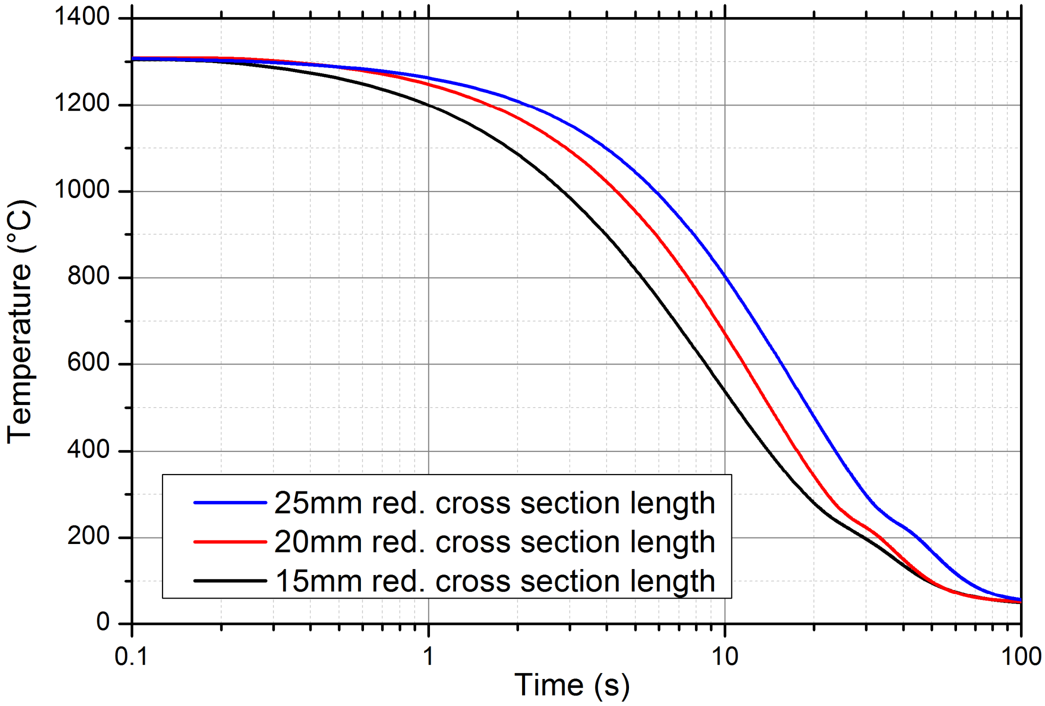

Figure 4.9: **Control temperature of a sample as a function of time during free cooling. Results are plotted for various sample reduced cross section lengths.**

As can be seen on Figure 4.8, for all reduced cross section lengths, a temperature difference less than 10 °C in a 3 mm wide region is only achievable up to a certain control temperature. On samples with 20 mm and 25 mm reduced cross section lengths, when control temperatures are higher than this threshold, the horizontal beam size can be reduced to minimize temperature variation in the measured region. For the 15 mm reduced cross section length, the temperature difference is too high, and reducing beam width would only work for very narrow incident beams, greatly reducing incident intensity. Therefore this reduced cross section length possibility is not preferable considering the others. The temperature difference between the 20 mm and 25 mm samples is not considerably high, but the achievable cooling rate in the first reduced cross section length is much higher than in the second, therefore, given both constraints, the optimal sample design for most experiments has a 20 mm reduced cross section length.

However, the results shown on Figure 4.8 and Figure 4.9 will be different for different materials, whereas each experiment has specific requirements in terms of measured region temperature resolution and cooling rate. Therefore different values for the reduced cross section length can be used depending on the experiment requirements.

4.2. Characterization as a Diffraction Instrument

The detectors used in the installation are positioned in the goniometer so that a known point in their surface is tangent to a circle centered in the goniometer turning axis, with a typical 361 mm radius. This point is called the detector central pixel. The detector is positioned so that its pixels lie along the diffraction plane. If the vector pointing from the intersection between the diffraction plane and the goniometer turning axis to the detector center is at a known angle to the incident beam vector, a 2θ value can be associated to each pixel of each detector. This is how intensity as a function of 2θ curves are obtained either in acquisitions or scans. To obtain correct measurements, it is imperative to position the sample irradiated region at the goniometer turning axis. The goniometer positioning is independent on the simulator positioning, and both are independent on the incident beam position. The alignment procedure is better understood if three different Cartesian reference frames are associated with the incident beam, sample and goniometer. The incident beam reference frame is fixed and defined as $\mathbf{e_x}$, $\mathbf{e_y}$ and $\mathbf{e_z}$. The incident beam travels along $\mathbf{e_z}$, and $\mathbf{e_x}$ is perpendicular to the diffraction plane. $\mathbf{e_y}$ is perpendicular to $\mathbf{e_z}$ and $\mathbf{e_x}$ and points in the vertical direction. The goniometer reference frame is defined through vectors **x**, **y** and **z**, parallel to $\mathbf{e_x}$, $\mathbf{e_y}$ and $\mathbf{e_z}$ respectively. Additionally, the goniometer has five degrees of freedom, three of them along directions **x**, **y** and **z**, one rotation degree of freedom around vector **x**, named $2\theta_g$, and one linear degree of freedom lying on the **yz** plane and positioned at an angle $2\theta_g$ from **z**, identified by its position *detd*, which allows to change the distance between the detector and the goniometer turning axis. The simulator reference frame is defined by $\mathbf{gl_x}$, $\mathbf{gl_y}$ and $\mathbf{gl_z}$, respectively parallel to $\mathbf{e_x}$, $\mathbf{e_y}$ and $\mathbf{e_z}$, having linear degrees of freedom along $\mathbf{gl_x}$ and $\mathbf{gl_y}$. The reference frames are shown on Figure 4.10.

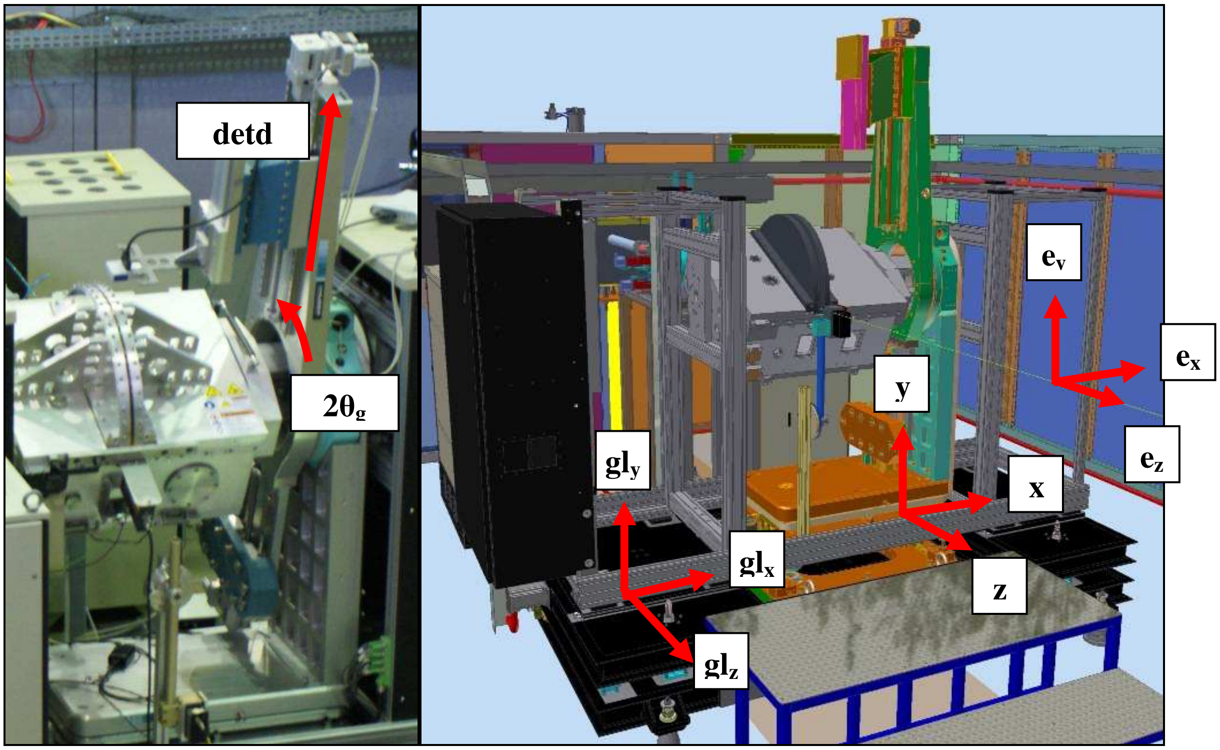

Figure 4.10: Incident beam, simulator and goniometer reference frames and movement degrees of freedom.

The alignent procedure is concluded when all reference frames are accordingly aligned and centered at the same point. The first step is to align the goniometer regarding the incident beam. **x** and **y** origins are aligned by observing the incident beam position in the goniometer reference frame using the detectors. $2\theta_g$ is defined as zero when **z** points along the $\mathbf{e_z}$ direction and the value of *detd* is defined as the distance between the detector center pixel and the goniometer turning axis. Afterwards, a standard sample is loaded in the simulator. By scanning the simulator horizontal position regarding the incident beam, the sample center position in the other reference frames is found, and $\mathbf{gl_x}$ is aligned. By scanning the simulator in the vertical direction (Figure 4.11), the point along $\mathbf{gl_y}$ where the sample highest edge hits the beam can be found.

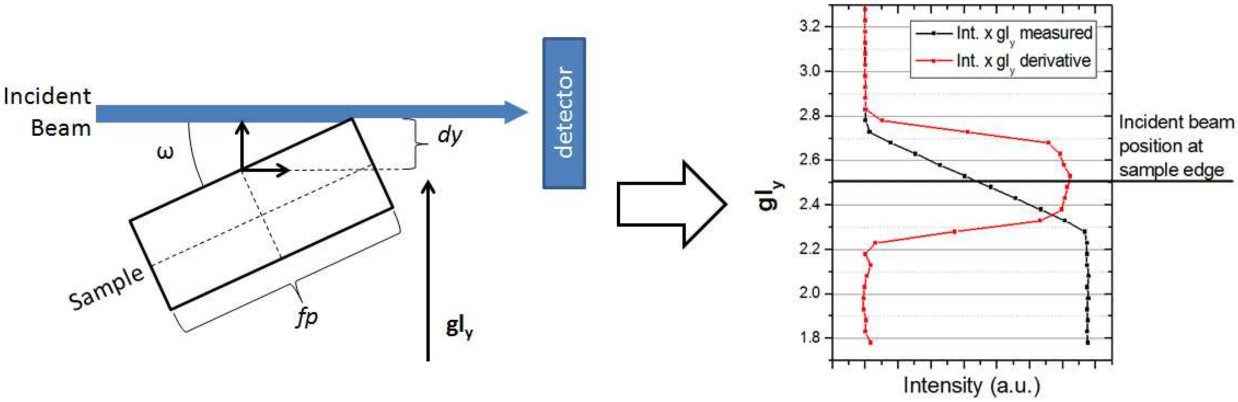

Figure 4.11: Schematic representation of the method to determine the y position of a sample regarding the incident beam.

This point, hereinafter called y_{edge}, can be found by fitting a peak function in the intensity by $\mathbf{gl_y}$ curve derivative. If the sample dimensions and the incident beam angle of incidence ω are known, the sample can be moved a distance $-dy$ from this point along $\mathbf{gl_y}$ so that the incident beam hits the sample surface center in the vertical direction. Defining *fp* as the sample width as shown on Figure 4.11, *dy* will be given by

$$dy = \frac{fp}{2}\sin\omega . \qquad \text{Equation 4.2}$$

Finally, by positioning the detector at a $2\theta_g$ position equal to the expected value $2\theta_{exp}$ of a peak from the standard sample, the **z** origin is adjusted so that the standard sample peak hits the detector at its central pixel, hence positioning the **z** origin at the point in which the incident beam hits the sample. In terms of diffraction, the most delicate part of this alignment is in the values on the diffraction plane, *i.e.* the y and z values for all reference frames. Figure 4.12 is a schematic representation of all reference frames projected in the diffraction plane in a misaligned and aligned condition.

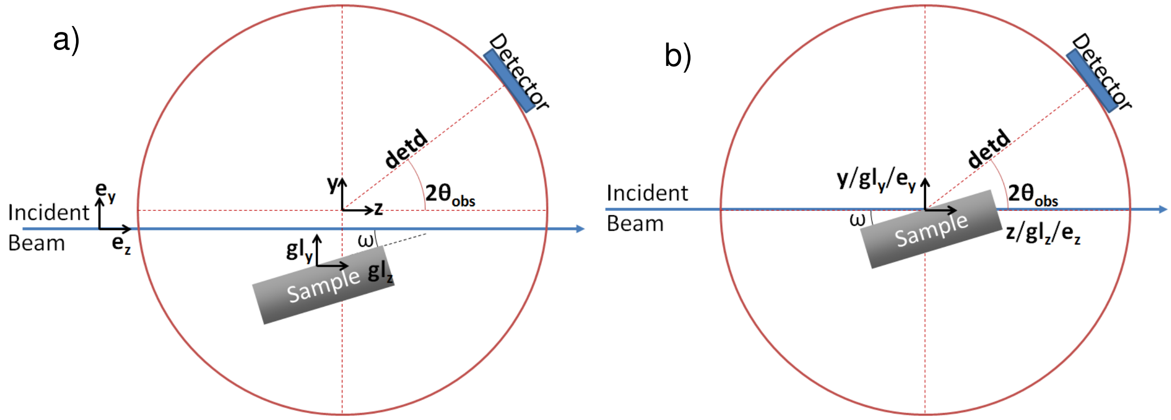

Figure 4.12: Misaligned (a) and aligned (b) installation components. Reference frames are projected in the xy plane.

Once this alignment is finished, the condition mentioned in the beginning of this section is satisfied, that is, the irradiated sample region is at the goniometer turning axis, and each pixel in the detector can be attributed to a diffraction angle 2θ using Equation 4.3:

$$2\theta = 2\theta_g + \tan^{-1}\left(\frac{(p - p_c)\times 0.05}{detd}\right).$$

Equation 4.3

In Equation 4.3, p is a pixel position, defined as an integer between 0 and 1279, p_c is the center pixel position, that is, the position at which the incident beam hits the detector when $2\theta_g$ is zero, and *detd* must be defined in millimeters. A scan is obtained by collecting intensity by 2θ curves at several $2\theta_g$ positions, and concatenating the curves obtained at each $2\theta_g$. If all steps described above are performed correctly, the goniometer, the incident beam and the sample should be aligned, which means that 2θ measured values are correct. In order to verify this, measurement of standard samples can be used. Figure 4.13 shows a scan performed with a standard Y_2O_3 sample, in which all present peaks were fitted using Pearson VII function. The fitted curves, background and peak positions are also shown. On the inset, the difference between the fitted and the measured curves is plotted as a function of 2θ.

Fitted peak positions were extracted and the equivalent d-spacing was calculated using Equation 2.9. The values were plotted with the expected d-spacing for these samples and are shown in Figure 4.14. A linear fit done in the plotted data is also shown. As can be seen in the fit errors values, the installation achievable resolution in lattice parameter calculation is approximately 10^{-5} Å. However, each new sample loaded in the simulator will have its reference frame positioned in a different point from the one in the sample used for alignment. The origin for $\mathbf{gl_x}$ and $\mathbf{gl_y}$ can be determined in the same way they were in the standard sample. In order to determine $\mathbf{gl_z}$, an indirect approach is used. If the sample is loaded using the fittings described in the previous section, the sample central axis will be in the same position as the standard sample axis. Defining the module of the distance between the reference frame origin and the sample cross section center in the **z** axis as *cz*, this value can be calculated for the standard sample and for a new sample loaded in the simulator (Figure 4.15) through Equation 4.4:

$$cz = \frac{p}{2}\sin\omega, \qquad \text{Equation 4.4}$$

where *p* is the sample thickness in the direction perpendicular to the irradiated surface.

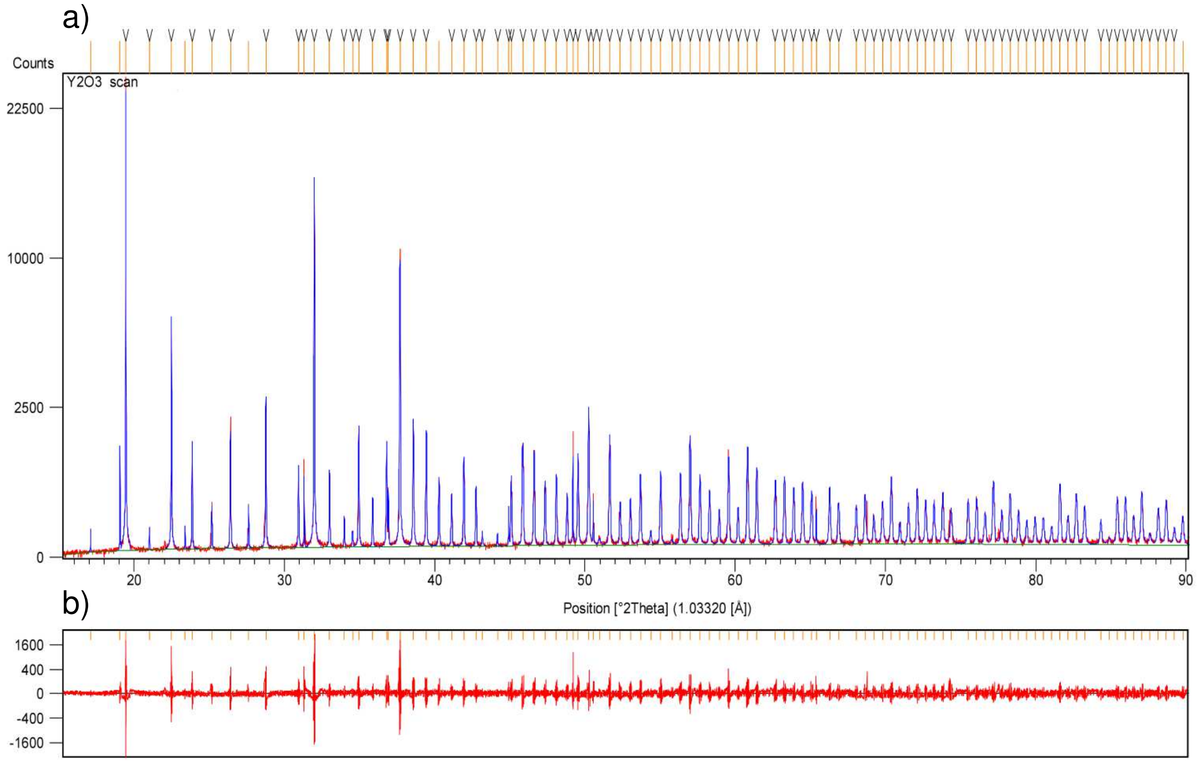

Figure 4.13: a) Measured intensity scattered by a Y_2O_3 standard sample as a function of 2θ. Measurement is shown in red, fitted peaks are shown in blue, peak positions are shown at the top. b) Measured intensity minus calculated intensity.

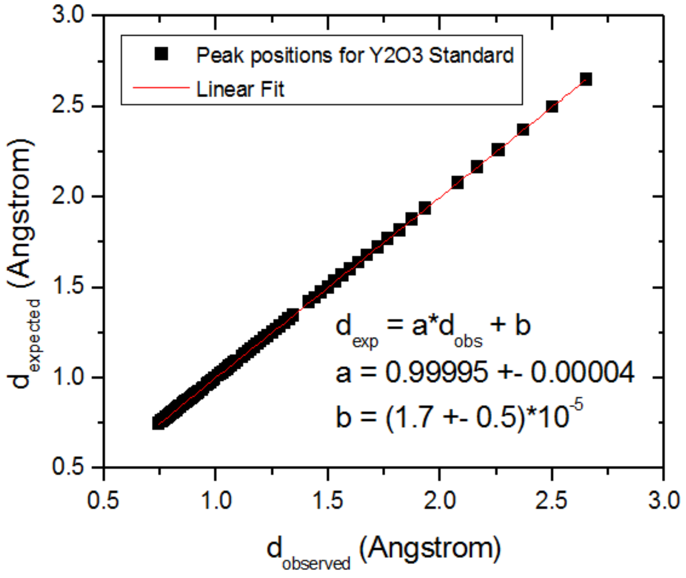

Figure 4.14: Measured d-spacings by expected d-spacings for an Y_2O_3 sample (Diffraction measurement shown on Figure 4.13). Data linear fit is shown in red, fit results are shown in the graph.

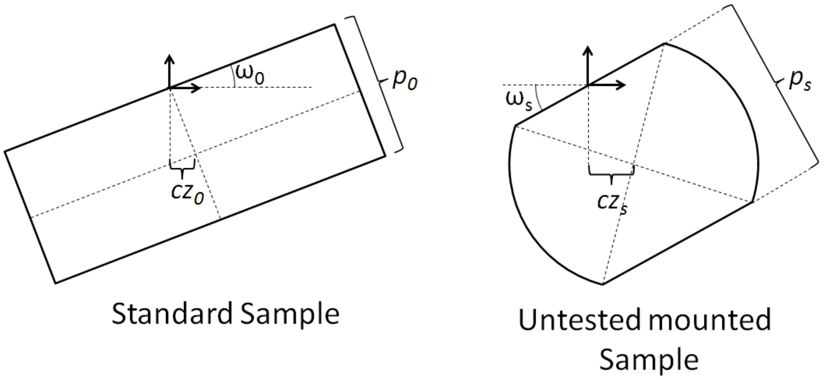

Figure 4.15: Relationship between z position in an alignment standard sample and an unaligned loaded sample

If cz is calculated in both cases, the correction necessary to align an untested sample is given by

$$dz = cz_0 - cz_S = \frac{p_0}{2}\sin\omega_0 - \frac{p_s}{2}\sin\omega_s \, . \qquad \text{Equation 4.5}$$

Once aligned, the determination of 2θ is done as described above, and peaks diffraction angle can be found reliably. However, if the sample shape changes during the experiment, it will become misaligned. The experiments done in the XTMS installation involve changes in temperature and strain and both processes will affect the sample dimensions. Assuming that the shape change is homogeneous along the sample cross section, being it an increase or decrease in area, the diffraction surface will move in a direction perpendicular to the surface plane. The incident angle will be the same, and the goniometer **y** position will still be aligned regarding the incident beam, but **y** and **z** will be misaligned regarding the sample reference frame (Figure 4.16). This will cause a displacement $\Delta 2\theta$ so that the observed $2\theta_{obs}$ value will be equal to the real value ($2\theta_{real}$) plus $\Delta 2\theta$. Such displacement can be calculated using Equation 4.6:

$$\Delta 2\theta = \tan^{-1}\left(\frac{\phi - \phi_0}{\phi_0} . \frac{p}{detd} . \frac{\sin 2\theta_{obs}}{\sin \omega}\right), \qquad \text{Equation 4.6}$$

where ϕ is the sample diameter, ϕ_0 is the initial sample diameter and p is the initial sample thickness. Since the value of ϕ is being constantly measured by the laser dilatometer during the experiment, its value can be used to correct $2\theta_{obs}$ once the results are obtained. Figure 4.17 shows the measured and corrected peak positions for a BCC {110} peak measured during a strain test of a SMA. The positions are plotted as a function of sample diameter variation. The force applied on the sample is shown as well.

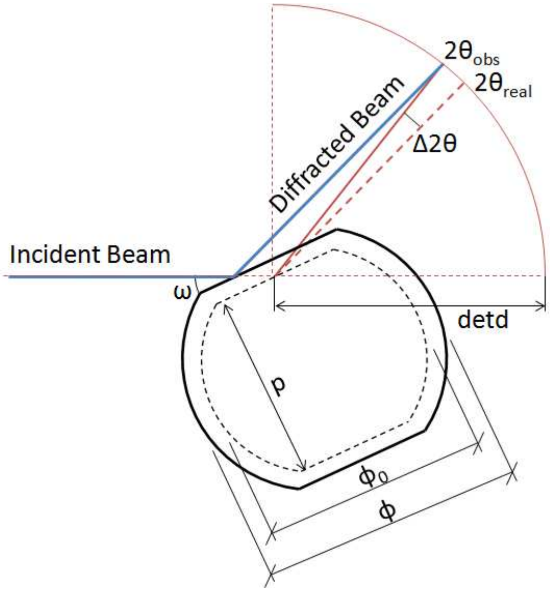

Figure 4.16: Schematic representation of how changes in the sample cross section area affect diffraction peak measured angle.

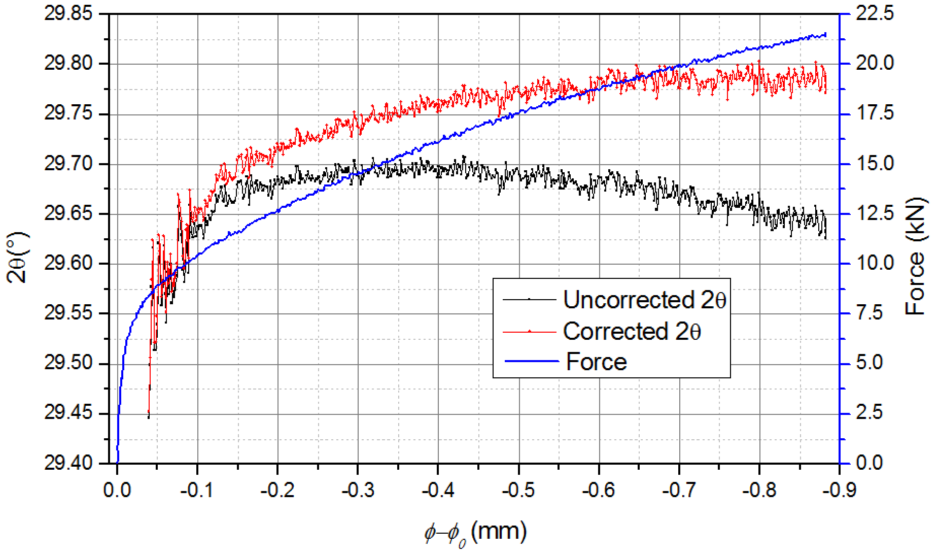

Figure 4.17: Force, uncorrected and corrected peak positions as a function of diameter variation during a deformation test. Correction was performed using Equation 4.6. The BCC phase is created due to a stress assisted transformation, and only appear after a diameter change of 0.04 mm.

Observing specifically the uncorrected peak position, after a diameter reduction of 0.4 mm, the peak 2θ angle starts to decrease. According to Equation 2.9, this would mean that the unit cell d-spacing is increasing with force, which is unreasonable given that this spacing is being measured perpendicular to the force application direction. The corrected values deliver more sensible results. For small deformation and/or heating experiments, the ϕ change will be small enough that the correction will be around 0.001 °, which has the same order of magnitude of the installation 2θ resolution. However, in some cases as the example above, this correction is essential to achieve plausible conclusions.

With careful alignment and corrections, diffraction angle can be measured precisely, but a complete characterization of the XTMS installation diffraction capabilities involves the description of measurement geometry, instrumental peak broadening, diffracted intensities, etc.

The measurement geometry used in the installation is mostly characterized by two factors: the fixed angle of incidence ω and the lack of diffracted beam focalization, the latter one present in conventional geometries like Bragg-Brentano and Guinier. Diffraction peaks collected in this geometry will have different characteristics if compared to data from conventional diffractometers, some of them detrimental to peak analysis. However this geometry is still preferable, given that it is advantageous to get data on large ranges of 2θ simultaneously, which is incompatible with sample rocking geometries. Figure 4.18 illustrates the diffraction of a parallel incident beam by a sample positioned at a fixed incidence angle.

As illustrated, every sample region along the diffraction plane will diffract at the same angle 2θ, but since each region is at a different position regarding the goniometer turning axis, each diffracted beam will reach the detector at a different 2θ position, creating a spread in the measured peaks. This spread, which is caused by the diffraction geometry used, can be determined by the angular distance between the center of diffraction peaks originated in the edges of the sample illuminated area, hereinafter named β_{geo}. Considering β_s as the peak broadening due to the sample, and that the incident beam and the beam diffracted by a single crystallite have Gaussian profiles, the final observed peaks will be a convolution of three functions: a Gaussian with width β_{geo}, a function which describes the density of crystallites contributing to diffraction along the direction **u** (as defined on Figure 4.18), and a Gaussian with width β_s. Given this description, this geometry will be problematic if two conditions are simultaneously met: if β_s is smaller than β_{geo} and if the number of crystallites diffracting along the **u** direction is not homogeneous.

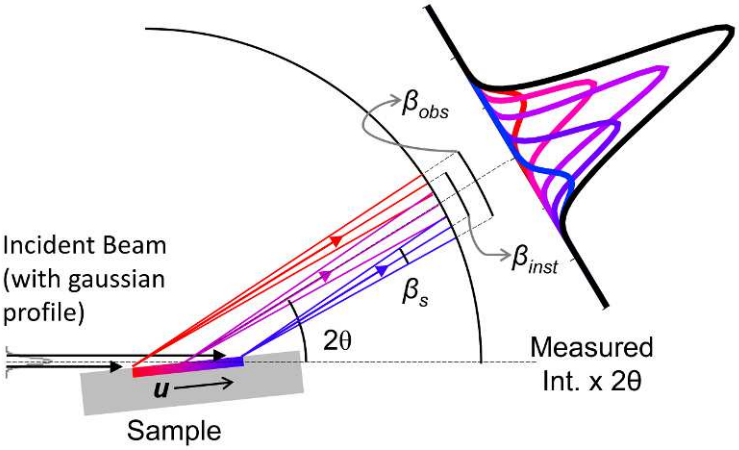

Figure 4.18: Diffraction geometry used in the XTMS installation. Sample regions are color coded, and diffraction curves from different regions are shown in equivalent colors. In this representation, the incident beam is considered to have no divergence.

For most samples, it is unlikely that different sample surface regions will have different phase populations, or even different textures. Even so, the inhomogeneity in crystallite distribution described above can be met due to different circumstances. If the observed volume is not large enough, this inhomogeneity will be caused by lack of statistical significance in the observed diffraction peaks, i.e., for a sufficiently small volume, there is no probabilistic guarantee that there will be a diffracting crystallite for every portion of the irradiated area. This is the case for the CeO_2 standard samples. The high absorption of these samples severely limits the incident beam penetration, limiting the observed volume, while the large crystallite size and small microstrain grants very sharp peaks. Figure 4.19 shows the effect of lack of statistics on measurements on the CeO_2 sample. The measurements were taken with the incident beam slits open 0.5 mm by 0.5 mm. The difference between the three measurements is the sample position along the $\mathbf{gl}_x$ direction (sample length). The jagged intensity distribution in 2θ is caused by a non-homogeneous diffracting crystallite distribution along the sample surface. The fact that this distribution changes with sample position shows that this is not a sample feature, but rather a statistic one. Another factor that influences the lack of statistics is crystallite size. The smaller the crystallite size, the higher is the probability of having crystallites contributing to diffraction along the whole observed volume

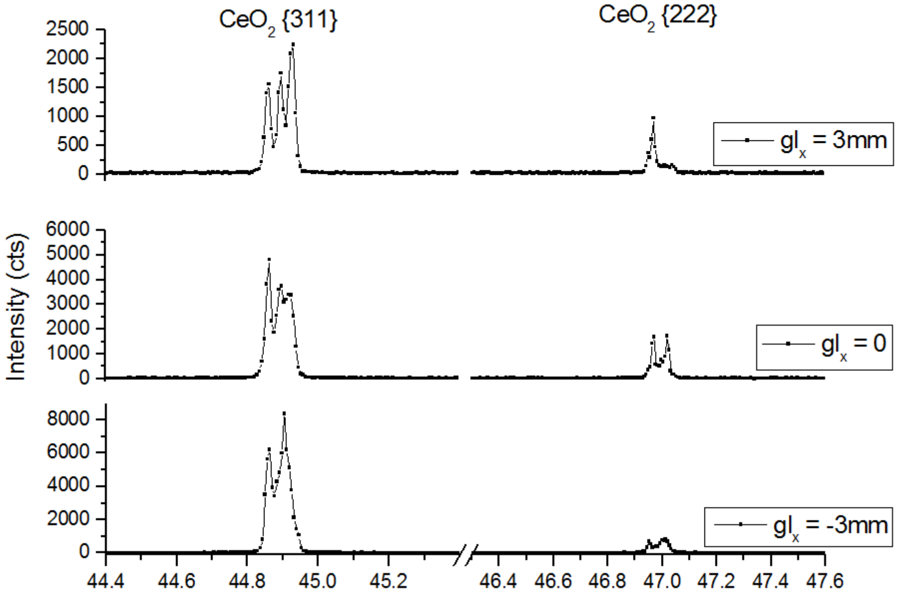

Figure 4.19: Measurements of {311} and {222} peaks from a CeO_2 standard sample. The wavelength used was 1.239 Å. The three curves were taken at different positions of the same sample.

For most metallic samples, the value for β_s is high due to microstrain, and crystallite size is small enough that statistics is not a problem. However, when some alloys are subjected to high enough temperatures, recovery and crystallite growth processes start to occur, decreasing β_s and sampling statistics, and peak features as the ones present on Figure 4.19 may be observed. To minimize this issue, it is interesting to increase the observed volume as much as possible. This can be done by increasing the incident beam size. In the horizontal direction, beam size must be limited due to thermal gradients inherent to the Gleeble® simulator, as explained on the previous section. In the vertical direction, an increase in the beam size will increase β_{geo}. This parameter is one of the factors affecting the total peak broadening caused by the instrument, namely β_{inst}, the other being the incident beam divergence. As stated in section 2.4, this broadening is ideally minimized to allow good microstrain or crystallite size determinations. β_{inst} can be calculated analytically through Equation 4.7:

$$\beta_{inst} = 2\beta_{div} + \beta_{geo} \, , \qquad \text{Equation 4.7}$$

where β_{div} is the incident beam divergence. Considering that this beam is focused on the sample, and calculating β_{geo} as a function of measurement geometry parameters such as beam size at sample position and angle of incidence (described schematically on Figure 4.20), β_{inst} as a function of 2θ is given by:

$$\beta_{inst}(2\theta) = 2\beta_{div} + 2\tan^{-1}\left(\frac{w}{2detd} \frac{\sin(2\theta - \omega)}{\sin\omega} \right) \qquad \text{Equation 4.8}$$

where w is the incident beam FWHM in the vertical direction at the sample position.

In order to verify this model, a scan was measured on an Y_2O_3 sample loaded on the simulator. The sample was positioned at an incident angle of 15 °, and the vertical slit was adjusted to 0.25 mm, yielding an incident beam with 0.18 mm FWHM, as measured by collecting an acquisition of the incident beam with the detector positioned at $2\theta_g = 0$. As discussed in the previous chapter, the peak broadening originated in this sample can be neglected if compared to the typical instrumental broadening, therefore the observed broadening can be directly associated with the instrument. The peaks FWHM as a function of 2θ are plotted in Figure 4.21. The red curve in this Figure was calculated using Equation 4.8 with parameters $\beta_{div} = 0.0065$ °, $w = 0.18$ mm and $\omega = 15$ °. The consistency between the model and the collected data shows that if the measurement parameters are known, the instrumental broadening can be reliably calculated analytically using Equation 4.8, allowing the deconvolution of β_{inst} and β_{sample} as described in Equation 2.22.

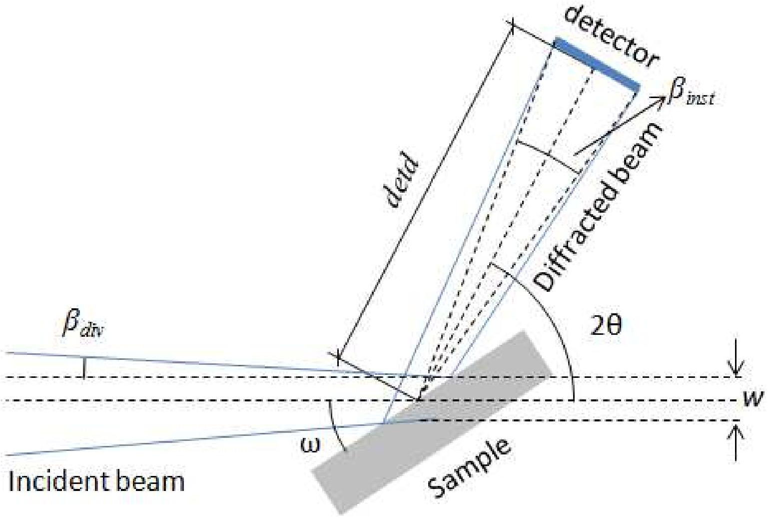

Figure 4.20: Diagram showing the geometric parameters involved in instrument peak broadening.

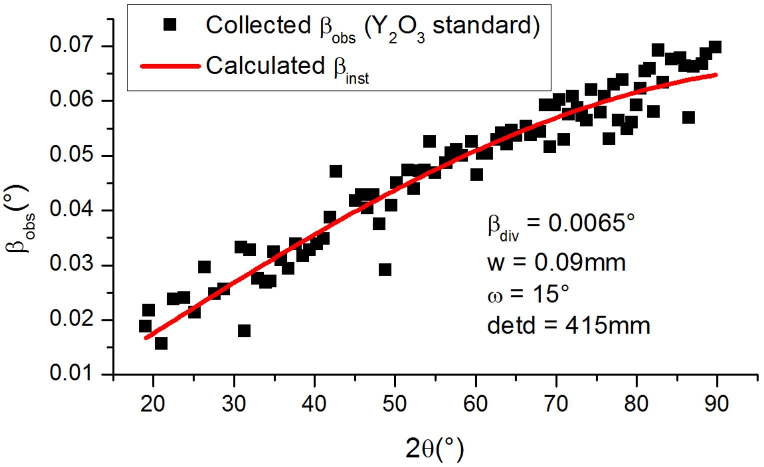

Figure 4.21: Measured and calculated peak widths as a function of 2θ, collected from an Y_2O_3 sample. Calculated values were obtained using Equation 4.8. Parameters used are shown in the graph.

Taking into account the need to maximize the observed volume and minimize instrumental broadening, an optimal configuration for incident beam conditioning and sample assembly uses incident beam slits of 2 mm or 3 mm in the horizontal direction depending on sample material, reduced cross section length and test temperature, 0.5 mm in the vertical direction, and an incident angle of 15 °. Depending on the material analyzed and the experiment goal, these values can be changed to optimize grain statistics or instrumental broadening.

Another important aspect of the XTMS installation is how peak intensities behave at different diffraction angles. In this sense, the main aspect is the absorption of scattered beams as a function of 2θ. The transmission of an X-ray beam travelling through a medium is given by Equation 4.9 (CULLITY, 1956):

$$\frac{I}{I_0} = e^{-\mu . tr}, \qquad \text{Equation 4.9}$$

where I_0 is the incident intensity, I the intensity after traveling through a distance tr and μ is the medium X-ray absorption coefficient. In XTMS, both the incident and diffracted beam paths are in vacuum. There is a polymer window separating the sample chamber from the detectors, but since the window distance to the sample is constant in 2θ, the absorption in the diffracted beam will always be the same. The atmospheric path variation between the window and the detector is in the order of millimeters, and the absorption suffered by diffracted beams on this path can be neglected. Therefore, the main absorption suffered by diffracted beams comes from their interaction with the sample. Given the fixed angle of incidence measurement geometry, photons scattered by the sample must travel a distance inside it, and the larger this distance, the larger will be the absorption suffered by the photons. If a beam travels through a distance *tr* inside the sample and is scattered at an angle 2θ, it has to travel a distance *tr'* to come out at the sample surface (Figure 4.22).

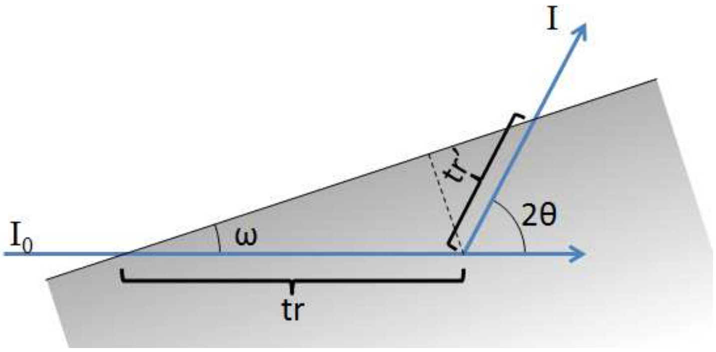

Figure 4.22: Path of an X-ray beam scattered by a solid sample with a flat surface.

The intensity of the transmitted beam will be:

$$I = I_0 e^{-\mu.tr} e^{-\mu.tr'}, \qquad \text{Equation 4.10}$$

but *tr'* can be written in terms of *tr* as

$$tr' = \frac{tr \sin\omega}{\sin(2\theta - \omega)}. \qquad \text{Equation 4.11}$$

Therefore the intensity of a scattered beam will be

$$I = I_0 e^{\mu.tr} e^{-\left(1+\frac{\sin\omega}{\sin(2\theta-\omega)}\right)} = cnt.e^{-\left(1+\frac{\sin\omega}{\sin(2\theta-\omega)}\right)}, \qquad \text{Equation 4.12}$$

where *cnt* is a constant value. Absorption will affect the analysis of peak intensities, but as shown in Equation 2.12, the absolute intensity of peaks is not used, but rather their relative values. Therefore, the constant *cnt* can be dropped and the intensity distribution as a function of 2θ will not depend on the material analyzed or on the distance traveled by the incident beam.

Figure 4.23 shows a measurement made on a SMA sample in which the effect of absorption is evident. The red curve was calculated using Equation 4.12 with ω equal to 18.2 °, and it shows the consistency between the absorption model and the measured intensities.

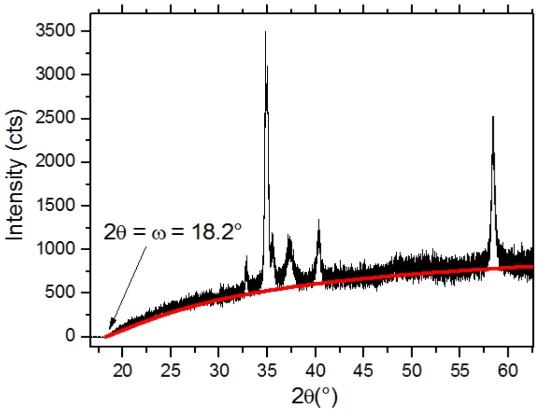

Figure 4.23: Diffraction curve of a SMA sample. The red curve was calculated with Equation 4.12 using ω equal to 18.2 °.

Despite the fact that the absorption coefficient of a material is not important in the determination of peak intensities, it still is important in the determination of the measured volume. The higher this coefficient, the lower will be the penetration of an X ray beam inside the material. It can be stated that the probability of a photon scattered after travelling a distance x from the surface being detected is proportional to $\frac{I}{I_0}$. Therefore, most of the collected X-rays will come from a depth in which this value is close to one. Since the relationship between absorption and distance described on Equation 4.9 is an inverse exponential, it is not possible to define a distance in which the transmission will be zero, but a good approximation is to use the attenuation length, that is, the distance in which the transmission is $\frac{1}{e}$. Figure 4.24 shows the attenuation length of various metals as a function of energy. The three materials studied in this work are steels, and as can be seen on this Figure, the measured volume for these materials will be restricted to a depth of approximately 10μm, since the attenuation length of steels will be very close to that of pure Iron.

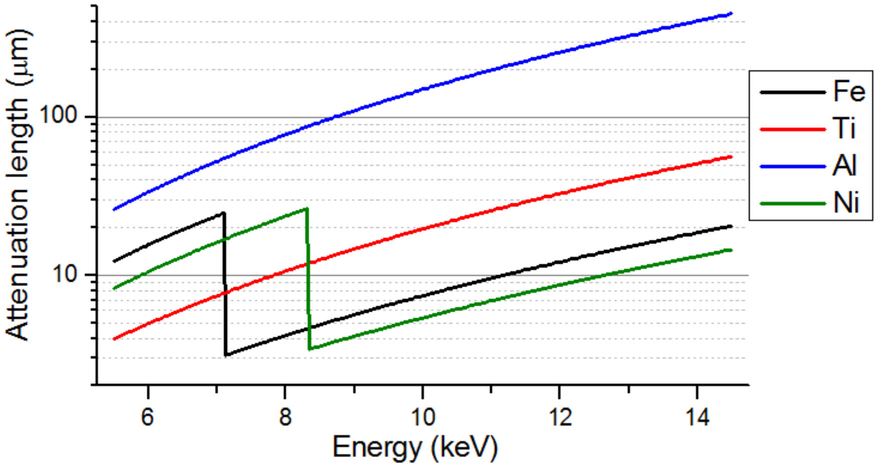

Figure 4.24: Attenuation length as a function of energy for various pure metals. Source:(HENKE; GULLIKSON; DAVIS, 1993)

The absorption can be used to determine the angle of incidence. As shown on Equation 4.12, when $2\theta \leq \omega$, $\frac{I}{I_0} = 0$. In an acquisition taken with $2\theta_g \sim \omega$, two regions are clearly defined, one where $I(2\theta) = 0$ and one where $I(2\theta) \neq 0$ (Figure 4.25). The 2θ value in the transition between the two regions is equal to ω. Given typical noise values on the detector, this value can be determined with a 0.1 ° resolution.

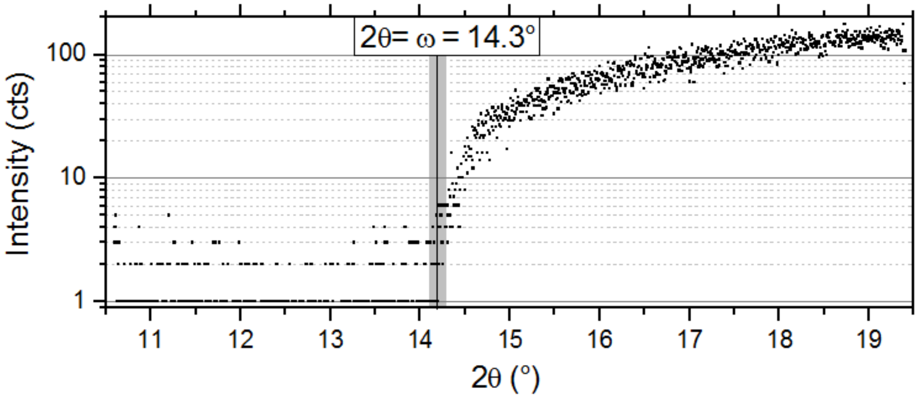

Figure 4.25: Intensity scattered by a sample as a function of 2θ when this angle is close to ω. The measurement made with a supermartensitic stainless steel sample revealed a ω of 14.3 °. The gray band indicates the resolution in its determination.

As discussed earlier in this section, the angle of incidence ω plays a major role in the alignment steps. However, given that the determination of ω has a limited resolution, it is interesting to investigate the error propagation from the resolution of ω to the resolution of 2θ. As shown before, the goniometer can be aligned with a standard sample with very high resolution. The alignment of new samples, on the other hand, depends on the indirect determination of two main values, *dy* and *dz*, which are highly dependent on ω. If a standard deviation *σ* is attributed to each parameter involved in the determination of *dy* and *dz*, the standard deviation on these values will be given by:

$$\sigma_{dy} = \sqrt{(\sigma_{yedge})^2 + \left(\frac{fp}{2}\sin\omega_s\right)^2\left(\left(\frac{\sigma_{fp}}{fp}\right)^2 + \left(\frac{\cos\omega_s}{\sin\omega_s}\sigma_\omega\right)^2\right)}, \qquad \text{Equation 4.13}$$

$$\sigma_{dz} = \sqrt{\left(\frac{p_0}{2}\sin\omega_0\right)^2\left(\left(\frac{\sigma_{p0}}{p_0}\right)^2 + \left(\frac{\cos\omega_0}{\sin\omega_0}\sigma_\omega\right)^2\right) + \left(\frac{p_s}{2}\sin\omega_0\right)^2\left(\left(\frac{\sigma_{ps}}{p_s}\right)^2 + \left(\frac{\cos\omega_s}{\sin\omega_s}\sigma_\omega\right)^2\right)} \cdot \quad \text{Eq. 4.14}$$

The standard deviation on each of these quantities is treated as equivalent to the error in their determination, that is, the resolution with which they were measured. Except for σ_ω, all other standard deviations involved in the calculation of σ_{dy} and σ_{dz} are small enough so they can be neglected. Therefore Equations Equation 4.13 and Eq. 4.14 can be simplified to:

$$\sigma_{dy} = \frac{fp}{2}\cos\omega_s \sigma_\omega , \qquad \text{Equation 4.15}$$

$$\sigma_{dz} = \sqrt{\left(\frac{p_0}{2}\cos\omega_0 \sigma_\omega\right)^2 + \left(\frac{p_s}{2}\cos\omega_0 \sigma_\omega\right)^2} . \qquad \text{Equation 4.16}$$

If typical sample sizes and angle of incidence are used, σ_{dy} will be ±0.007 mm and σ_{dz} will be ±0.004 mm. In order to verify the effect of σ_{dy} and σ_{dz} on the determination of 2θ, a displacement Δy and Δz from the aligned condition is assumed, which will create a displacement in 2θ as described by Equation 4.17:

$$\Delta 2\theta = 2\theta - \tan^{-1}\left(\frac{detd\sin(2\theta) - \Delta y}{detd\cos(2\theta) - \Delta z}\right). \qquad \text{Equation 4.17}$$

The standard deviation on Δ2θ will be given by:

$$\sigma_{\Delta 2\theta} = \left(\frac{\left(\frac{detd\sin(2\theta) - \Delta y}{detd\cos(2\theta) - \Delta z}\right)}{1 + \left(\frac{detd\sin(2\theta) - \Delta y}{detd\cos(2\theta) - \Delta z}\right)^2}\right)\sqrt{\left(\frac{\sigma_{\Delta y}}{detd\sin(2\theta) + \Delta y}\right)^2 + \left(\frac{\sigma_{\Delta z}}{detd\cos(2\theta) + \Delta z}\right)^2} . \text{Equation 4.18}$$

In the determination of $\sigma_{\Delta 2\theta}$ shown above, σ_{detd} was neglected, due to its small value and minor effect on $\sigma_{\Delta 2\theta}$. Taking Δy = 0.000±0.007 mm and Δz = 0.000±0.004 mm and using the typical *detd* of 361 mm, $\sigma_{\Delta 2\theta}$ will be given by:

$$\sigma_{\Delta 2\theta} = \left(\frac{(\tan(2\theta))}{1 + (\tan(2\theta))^2}\right)\sqrt{\left(\frac{0.007}{361\sin(2\theta)}\right)^2 + \left(\frac{0.004}{361\cos(2\theta)}\right)^2} . \qquad \text{Equation 4.19}$$

Figure 4.26 shows Δ2θ±$\sigma_{\Delta 2\theta}$ plotted as a function of 2θ. Since σ_{dy} and σ_{dz} are not zero due to the facility resolution limits, particularly in the measurement of ω, even if all alignment steps are performed correctly, it is not guaranteed that the 2θ resolution presented on Figure 4.14 will be met for untested samples. However, this is a 2θ scale error, that is, the Δ2θ caused by a misalignment will be a smooth continuous function, restricted to values inside the grey area on Figure 4.26. In other words, the goniometer and detector assembly still have a ~10^{-5} ° positioning resolution. The resolution on peak position determination is dependent on peak signal to noise ratio, peak shape, and on the profile function used. In ideal cases, it can reach this 10^{-5} ° resolution. If a peak position change is detected with a displacement that is smaller than $\sigma_{\Delta 2\theta}$ during an experiment, that change still exists, only the scale will have the $\sigma_{\Delta 2\theta}$ uncertainty.

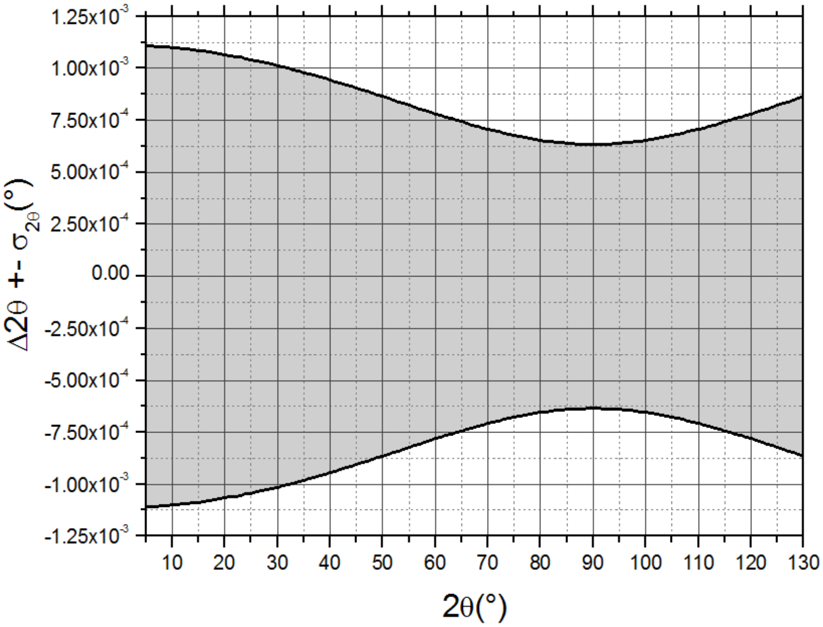

Figure 4.26: $\Delta 2\theta \pm \sigma_{2\theta}$ by 2θ plot. The gray region identify the region available to a non-zero displacement function Δ2θ(2θ) caused by alignment resolution limits.

4.3. Data processing and Analysis

The data measured in the XTMS installation and extracted from the thermomechanical simulation and X-ray detectors control computers require some processing before analysis techniques can be applied. Such data can be divided in two categories, the thermo-mechanical and the X-ray detectors acquisitions. The first processing step is to temporally synchronize the data belonging to both categories. As stated before, the X-ray detector data is organized in a three dimensional structure containing intensity, 2θ and time. Instead of working with several intensity vs. 2θ curves, for most cases it is more interesting to determine the present peaks characteristics and proceed to analyze these as a function of time. A diffraction peak can be in principle mathematically described by a peak function, and in turn, this function can be described by three principal characteristics, position, FWHM, and area. During this work, most data was analyzed using a Gaussian profile function. Figure 4.27 shows how such characteristics are related to a least squares fitted Gaussian curve in a measured diffraction peak.

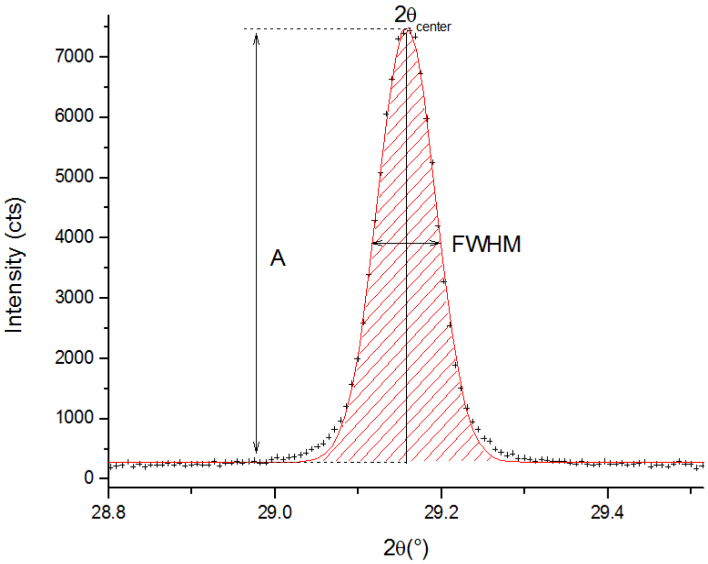

Figure 4.27: Peak fitting by a peak profile function. Experiment data is shown in black and fitted curve in red. The profile function main parameters are shown. The area is shown by the striped red region.

The philosophy of data processing in this work consists initially of finding the peaks present in each acquisition, whether in an automated manner or based on user input. Once found, one function selected by the user among several is fitted to the peaks using least squares method, and peak information is exported and correlated with thermomechanical data. Based on dilatometry data and certain other alignment information, peaks have their area, position and width corrected as described in the previous section, and finally, the data is ready for analysis. Figure 4.28 shows a flowchart illustrating this process. After processing, several analysis procedures can be applied to find relevant information, such as lattice parameters, phase fractions, microstrain, etc.

Given the large amount of data provided by the facility, these procedures are applied in an automated manner, with little need for user intervention. A number of different platforms are used in this process, such as Igor©, Matlab© and MS Excel© software and various programming languages such as Pascal, Visual Basic and C.

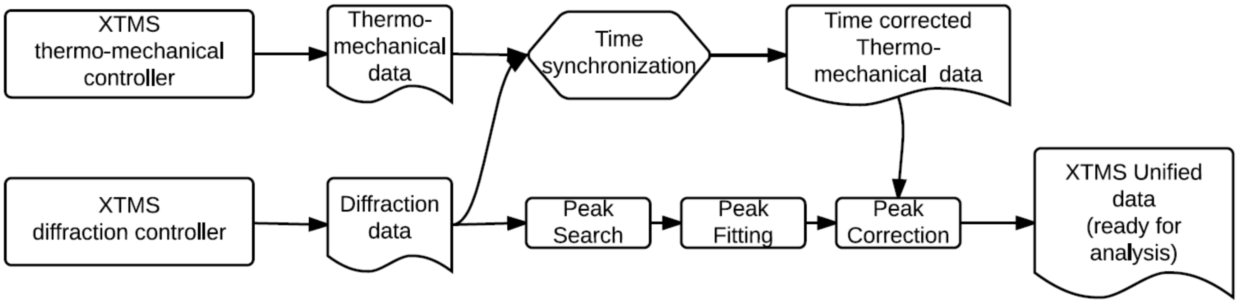

Figure 4.28: Flowchart indicating the data processing algorithm.

To perform this procedure two methodologies were developed: the first was created by the author, and involves the use of several software environments:

- In Matlab© data is temporally synchronized and reconditioned to assign a set of thermomechanical data to every X-ray detector acquisition. Other actions such as interpolation or concatenation of diffraction data can be performed. These are used in the assembly of scans based on acquisitions taken at different $2\theta_g$ values. The routine also reprints the data in a format compatible with HighScore©.

- In HighScore©, each acquisition is sequentially processed. During this processing, peak search and fitting occurs. This program allows the selection of various peak functions as well as peak search method and least-squares fitting procedure customization. Routines programmed by the author allow the identification of data in which fitting failed, or whose results deviate from the average behavior.

- The fitted results are exported to MSExcel©, where, based on information provided by the user, a macro organizes fitted peak results based on the phase and plane family that originated each peak. On this platform, the corrections described in the section above in Equation 4.6 and Equation 4.12 are performed.

This methodology uses powerful software which allow for fast data processing, great verstility in terms of fitting functions and high degree of success in fitting convergence. However, as several programs are involved in this method, its application may be cumbersome and time consuming. In addition, routine customization occurs mainly in the program code and therefore it is less accessible to users not familiar with programming.

The second approach aims to facilitate data vizualization and provide a less powerful but rapid data analysis environment. The core of this environment was programmed in Igor Pro® by Suresh. S. Babu and based on the routines used in reference BABU et al. (2005). Further development of this program was performed by CPM-LNNano team (Guilherme A. Faria and Leonardo Wu). This tool is simple to use and accessible to unexperienced users and allow the implementation of all the steps shown in the flowchart of Figure 4.28 up to peak fitting, all in a single interface. However, it is limited in the number of fitting functions available and in the peak fitting degree of success.

Once the raw data is processed using one of the previously described metodologies, the peak information can be analysed to obtain information about the material such as:

- Microstrain, which, when applicable, can be derived from Equation 2.22 and Equation 4.8.
- Lattice parameter, which can be derived from peak position through Equation 2.5, Equation 2.9 and Equation 4.6.
- Phase volume fractions, which can be derived through Equation 2.15 and Equation 2.13.

A few observations are important concerning the determination of lattice parameters and phase fractions. Lattice parameters will be derived from peak positions, and taking into account the resolution limit presented on Equation 4.18, d-spacing values will have a standard deviation described by

$$\sigma_d = \frac{d}{\tan\theta}\frac{\sigma_{\Delta 2\theta}}{2}. \qquad \text{Equation 4.20}$$

Hence, similarly to Figure 4.26, a curve can be constructed for σ_d as a function of d-spacing. This curve is shown on Figure 4.29. It is important to restate that this will be an error in the scale. d-spacing values from a single peak collected during a experiment can still be compared with a higher resolution than the presented one.

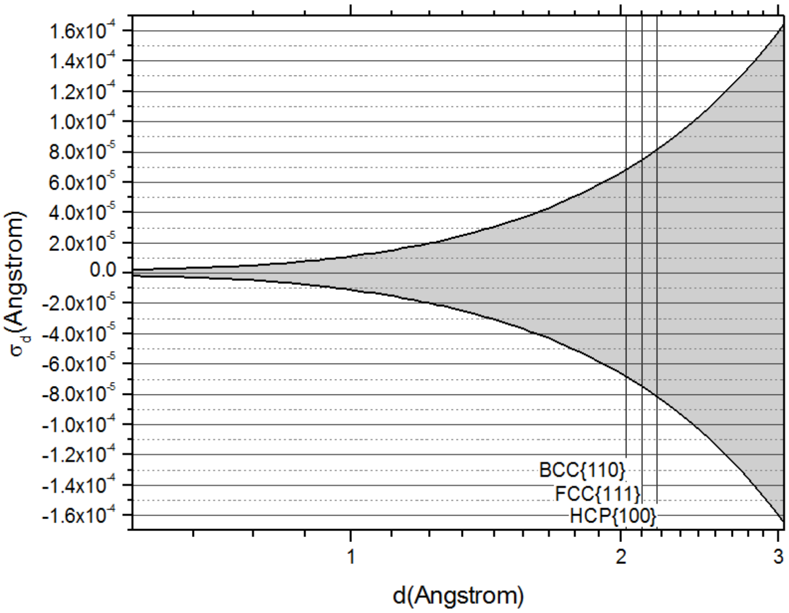

Figure 4.29: σ_d by d plot. The gray region shows the absolute value σ_d. In the graph, the d-spacing for the first peaks of typical metallic crystalline structures are shown.

As for phase volume fractions, those will be dependent on some characteristics of the XTMS installation, as shown on Equation 2.13. A few observations concerning these parameters are shown below:

- $A(\theta_{\{hkl\}})$ is known, being already applied in the data processing peak correction step.
- Since the incident beam is produced in a synchrotron and the diffraction plane is vertical, there will be no loss of intensity through polarization in the Thomson

scattering, and $Pol(\theta_{\{hkl\}})$ will be equal to one (ALS-NIELSEN; MCMORROW, 2011).

- The Lorentz factor $L(\theta_{\{hkl\}})$ will be the same as for other polycrystalline diffraction geometries, and given by Equation 4.21 (CULLITY, 1956):

$$L\left(\theta_{\{hkl\}}\right)=\frac{1}{4\sin^2\theta_{\{hkl\}}\cos\theta_{\{hkl\}}}. \qquad \text{Equation 4.21}$$

- One limitation arises when considering the prefered orientation factor $P_{p\{hkl\}}$, Which accounts for the material preferred orientation, or texture. This factor is normally represented mathematically through an orientation distribution function written as spherical harmonics in the three Euler angles. This information can be obtained by using Backscattered Electron diffraction (EBSD), associated to scanning electron microscopy, or through X-ray or neutron diffraction measurements in very specific geometries, not available at XTMS. With the measurements performed at the installation it is not possible to make quantitative assertions over this function. Still, in some cases, through the observation of the behavior of several peaks from the same phase, qualitative assertions can be made about the evolution of samples texture. When this is the case, phase fraction quantification won't be performed, given that the numerical value of $P_{p\{hkl\}}$ cannot be determined, and if a set of values is assumed, the relative phase volume fractions calculated would be biased. When no initial texture or its development during the test are expected, phase quantification calculations will be carried out considering the $P_{p\{hkl\}}$ value as one.

It is important to note that in this work, phase fraction results are only applicable to the observed volume, which is comprised of grains close to the sample surface and oriented in very specific directions. This will always be taken in consideration in the analysis performed.

With the considerations above, Equation 2.13 is simplified to:

$$R_{p\{hkl\}} = \frac{M_{p\{hkl\}}\left|F_{\{hkl\}}\right|^2}{v_p^2 4\sin^2\theta_{\{hkl\}}\cos\theta_{\{hkl\}}}. \qquad \text{Equation 4.22}$$

Another important observation concerns the calculation of $F_{p\{hkl\}}$. As shown in Equation 2.11, the value of $F_{p\{hkl\}}$ is dependent on site elemental fractional occupation, site position and atomic displacement factor. For the three main crystalline structures of metallic materials, FCC, BCC and HCP, crystallographic site quantities are locked by symmetry, and therefore all sites presented in Table 2.1 will have identical parameters. Also, since the inter-atomic distance and coordination number is the same for Fe and substitutional elements, the atomic displacement factors for different atoms can be considered the same, and can be taken out of the structure factor calculation as a constant, being disregarded as were the other constants in Equation 2.12.

For most cases, the main source of uncertainty in the $F_{p\{hkl\}}$ calculation will be the occupation factor o_{an}, since all the materials measured are solid solutions, and there is not a fixed occupation factor for the crystallographic sites. At the start of an experiment, if the material has only one phase, the chemical composition can be assumed to be homogeneous along the material, and if its value is known, $F_{p\{hkl\}}$ can be calculated without large errors. However, the studied materials fabrication method may introduce nano, micro and macro compositional gradients along the samples, and besides, as the tests evolve, chemical compositions will change through diffusion between regions with different temperatures, and between phases when more than one is present. Therefore, an uncertainty must be associated with the value of o_{an}. This uncertainty is hardly predictable and will be different for each sample depending on its history. If the uncertainty values assumed for each sample are too low, a bias will be introduced in the final calculation of $F_{p\{hkl\}}$. Therefore, for the studied materials, it is assumed that all atoms, except for Fe, have a normal occupation distribution at each site with FWHM equal to half the expected occupation. This is a rather high value, not applicable in most cases, but in the analyses performed, a high uncertainty is preferable to a biased value. For Fe atoms, o_n is set as a balance value in order to keep the sum of occupation factors in a phase equal to one. With this composition distribution the occupation in each value at each site will have a standard deviation of

$$\sigma_{o_{an}} = \frac{o_{an}}{8\ln 2}. \qquad \text{Equation 4.23}$$

Assuming there is no covariance between $\sigma_{o_{an}}$ of different sites and atoms, the structure factor standard deviation will be

$$\sigma_{F_{\{hkl\}}} = \sqrt{\sum_{n}^{N}\sum_{a}^{A}\left(\sigma_{o_{an}} f_a e^{2\pi i(\mathbf{K}.\mathbf{r}_n)}\right)^2}\ . \qquad \text{Equation 4.24}$$

Finally, the standard deviation in the $R_{\{\mathrm{hkl}\}}$ value will be given by

$$\sigma_{R_{\{hkl\}}} = R_{\{hkl\}}\left(2\frac{\sigma_{F_{\{hkl\}}}}{F_{\{hkl\}}}\right). \qquad \text{Equation 4.25}$$

In the materials analyzed, considering only the composition standard deviation, a standard deviation from 0.1% to 3% in phase volume fraction is observed, depending on material composition and phase. In the volume fraction calculation, the acquisitions signal to noise ratio will also be a source of uncertainty and must be considered. In the experiments performed, the deviation introduced by noise in the collected diffraction intensities was normally higher than the effect of compositional deviations but still, both deviation sources were always considered.

4.4. Stress Induced Phase Transformation Study in Shape Memory Stainless Steels

The goal of this experiment was to observe the phase transformations involved in the deformation of a FeMnSiCrNi shape memory alloy. These materials present interesting shape memory properties and low cost, when compared with typical SMAs like Ni-Ti and Cu based alloys. In order to understand how the material can be used functionally, testing its capabilities in operating conditions is essential, but not enough, as only information on the crystallographic structure can give the insight on how the martensitic transformation is affecting the material macroscopic behavior. The experiment presented here is based in such conditions, being focused on the stress induced transformations happening during deformation.

Figure 4.30 shows how stress, strain and temperature evolved on the SMA material submitted to a deformation and recovery test. The stress variations during the sample deformation were caused not by the sample, but by an incorrect adjustment of the simulator force control parameters. It was not possible to repeat this test once the parameters were adjusted due to unavailability of beamtime, but despite the force variations, the stress and strain behavior were followed through the whole test, and stress average behavior is consistent with other experiments. After the heating cycle, the sample shows a recovery of 0.017 of the initial 0.037 plastic strain applied (Figure 4.30). This is consistent with previous results carried out with similar alloys (ARRUDA; BUONO; ANDRADE, 1999), where a recovery of 0.026 was reported after a total strain of 0.04.

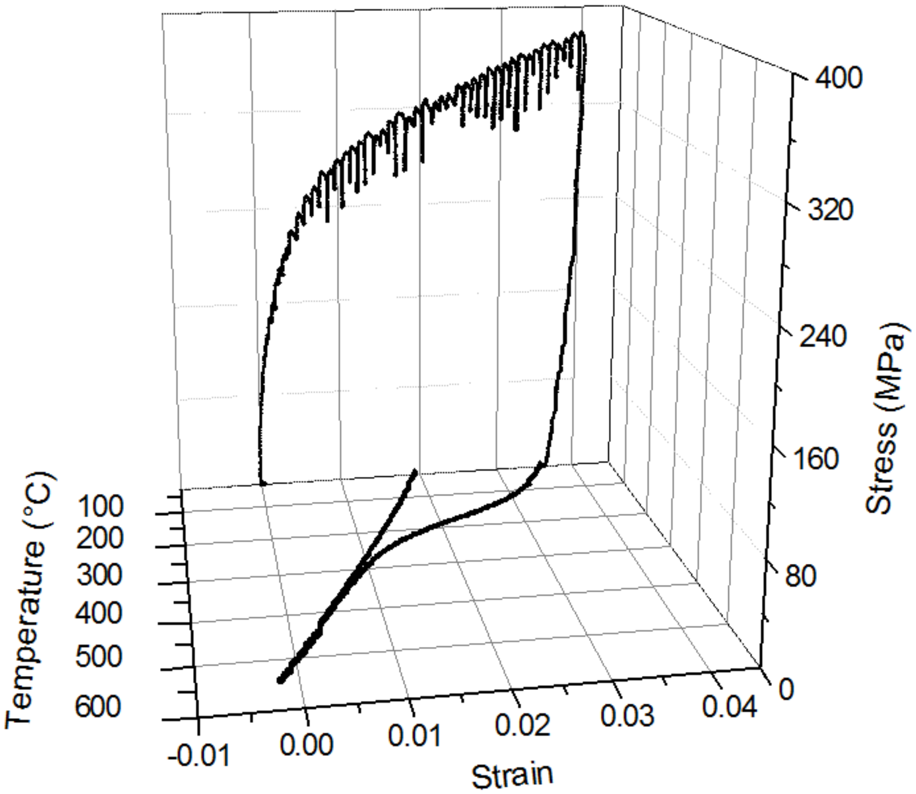

Figure 4.30: Stress, strain and temperature behavior in a deformation and recovery test in the SMA steel studied.

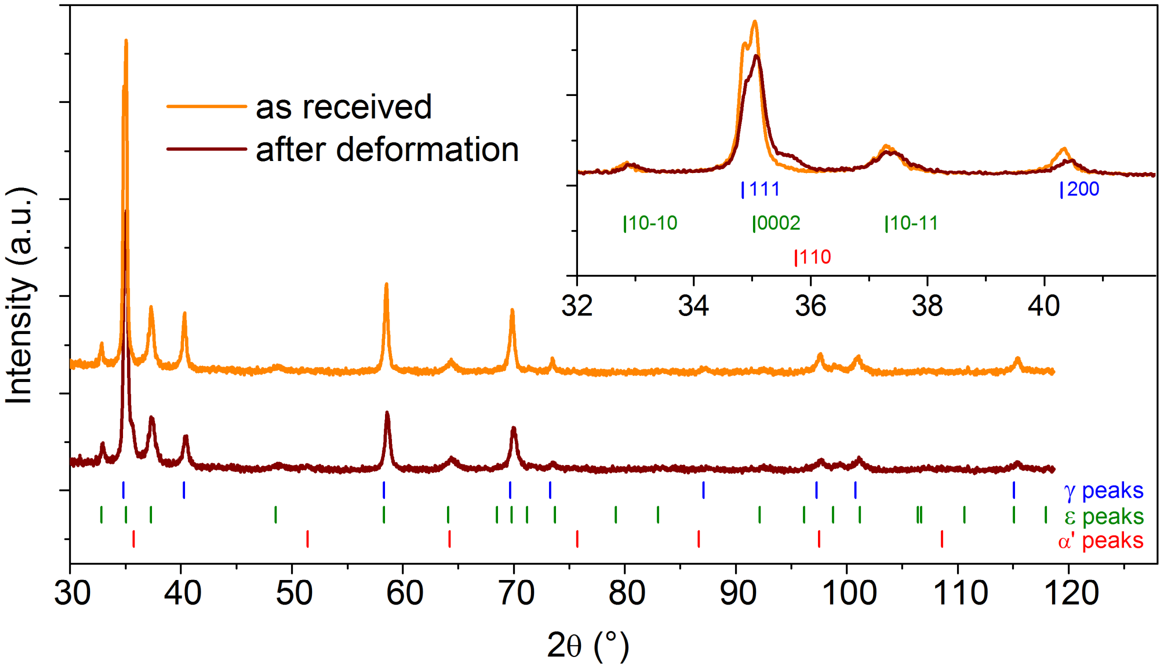

Figure 4.31: Diffracted intensity 2θ scan from the SMA sample as received, and after 4% strain. The inset shows the region measured during the *in situ* stage of the experiment. Bellow the graphs are the expected peak positions for the three structures.

Figure 4.31 shows scans taken before and after the test deformation step. The sample phase composition prior to the test shows the presence of γ and ε. Peak intensities for ε seem to indicate a highly textured state for this phase, preventing the application of Equation 2.15 for phase volume fraction determination. Notably, ε {0002} peak is much stronger and less wide than expected when compared to other ε peaks, suggesting that in addition to texture, the amplitude of lattice distortions for this phase is direction dependent. The scan after deformation shows that during the strain test there is formation of α'.

During the strain test, several acquisitions on the 2θ region between 32 ° and 42 ° were collected, and peak intensities on these acquisitions were derived using a Gaussian function through the application of the first processing method described on section 4.3. Despite the lack of reliability in phase volume fraction calculation, the phase transformations associated with stress can be understood by observing the variation of peak areas as a function of strain. Figure 4.32a shows the area variation as a function of strain for the three most intense peaks from all present phases, γ {111}, ε {0002} and α’ {110}. The peak area fluctuation was calculated as the difference between peak intensity at a given strain and its intensity at the beginning of the experiment. On Figure 4.32 b, the stress values on the sample as a function of strain are shown. The exposure time for each acquisition lasted 15s, and stress was taken as the mean of all stress values measured during this time period.

As can be observed on Figure 4.32a, once the elastic limit is reached, the intensity of γ {111} peak decreases steadily with increasing strain, while ε {0002} peak intensity increase, indicating a γ→ε transformation. For a strain above 0.01 peaks from α' phase can already be observed but with little intensity. Once the strain reachs 0.02 and for values above it, the intensity of ε {0002} peak stagnates, α' {110} intensity start to increase drastically, and the γ {111} intensity continues to decrease, indicating either γ→α' or γ→ε→α ' transformations.

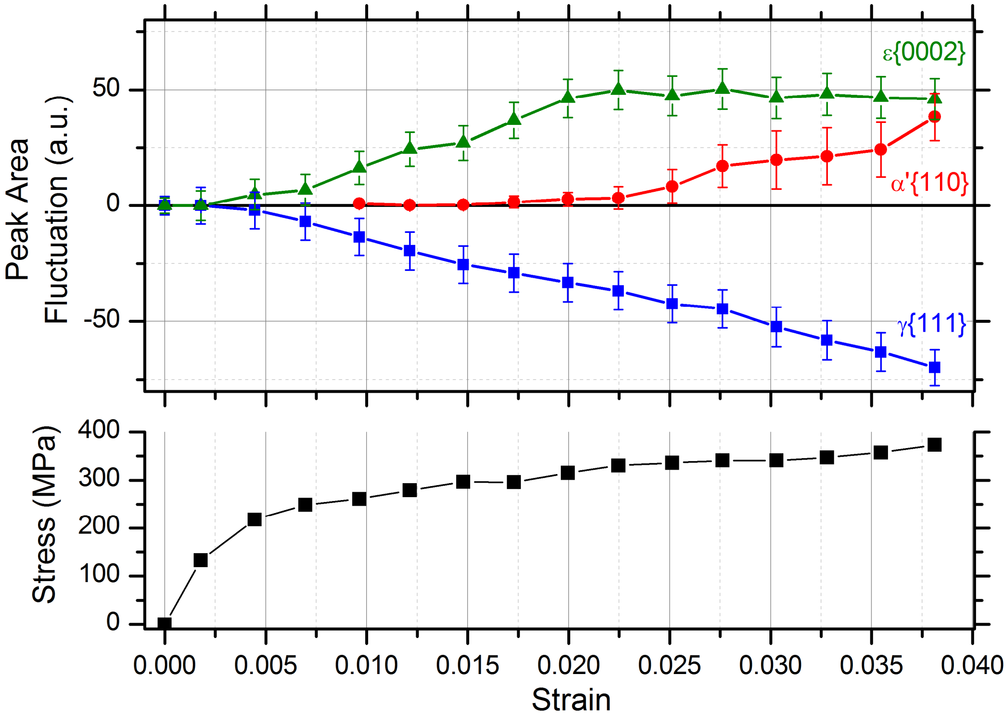

Figure 4.32: Peak area comparison for the three phases main peaks and stress applied at the sample as a function of strain.

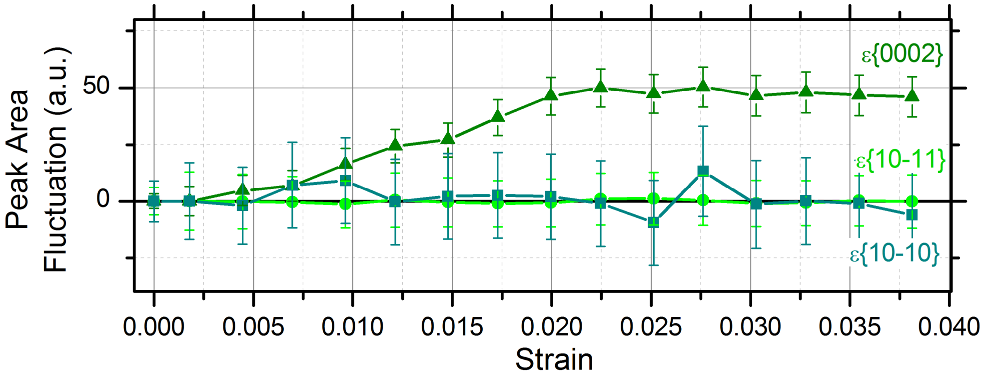

Figure 4.33: Peak area comparisons for three peaks from the ε phase as a function of strain.

The 0.02 strain mark is approximately the same point where the α' peak observed intensity begins to increase. If a direct correlation between strain and phase transformation is established, it can be stated that the first strain of 0.02 is associated with a γ→ε transformation, while the rest of the strain is associated with the formation of α' through either a γ→α' or γ→ε→α' transformations, which are not reversible. Therefore, the recovery of this material is limited due to the formation of α'.

Another interesting stress-induced transformation feature on this material can be seen in Figure 4.33, where the area fluctuation of three ε phase peaks as a function of strain is displayed. The only peak showing an evolution in intensity is {0002}. As stated on section 2.5, the displacive transformation γ → ε presents an orientation relationship between the parent γ phase and the formed ε phase, with the following orientation relationship: $(111)_\gamma // (0001)_\varepsilon$ and $[11\bar{2}]_\gamma // [1\bar{1}00]_\varepsilon$. If the distance between the successive planes along [110] in γ and [0001] in ε was the same, the parent γ phase would be sheared in ~19.5 ° along $[11\bar{2}]$ direction to form ε. This distance has been shown to be different in some ferrous alloys (NISHIYAMA, 1978), and this seem to be the case in this study, since, as seen on Figure 4.31, $d_{\gamma\{110\}} \neq d_{\varepsilon\{0002\}}$. Nonetheless, the difference is small enough so that it can be stated that the γ→ε transformation carries a strain along the $[11\bar{2}]$ direction in γ phase or [1-100] direction in ε phase. In a stress induced transformation, the transformation will happen in a way that minimizes stress. Since the stress application direction is perpendicular to the diffraction plane, the shear involved in the formation of ε grains diffracting in $\{10\bar{1}0\}$ and $\{10\bar{1}1\}$ conditions would contribute very little or nothing to a macroscopic strain along the load application direction, while grains diffracting in the {0002} condition would have a high contribution. Therefore, in this experiment, it is expected that close to none grains would form with $[10\bar{1}0]$ and $[10\bar{1}1]$ directions parallel to the diffraction plane. It is also important to note that the γ phase {111} plane family has a multiplicity of 8 while the ε phase {0002} plane family has a multiplicity of 2. Therefore, the application of uniaxial stress would induce a variant selection, and formation of texture. Since the stress application direction lies in the same plane as did the highest stresses involved in the sample surface machining, it can be stated that the sample machining itself caused the initial observed texture. As for the α' phase, only its main peak can be clearly defined, and thus it is not possible to say whether this phase is textured and once again, to determine phase volume fractions reliably.

4.5. Ferrite Decomposition Study on Superduplex Stainless Steel UNS S32750

The objective of this experiment was to observe the effect of elastic tension on the decomposition kinetics of ferrite phase (α) in the superduplex stainless steel UNS S32750, when exposed to the temperature range between 700 and 900 ^{o}C. As described before, when such steels are subjected to this elevated temperature range, the precipitation of new phases, as chi phase (χ), sigma phase (σ), and nitrides, among other is expected. In particular, sigma phase (σ) precipitation reaction in superduplex stainless steels presents an important challenge to metallurgist, because of its accelerated kinetics and damaging effect on the mechanical and environmental performance of the material. Sigma phase (σ) forms through the ferrite phase decomposition through a eutectoid transformation $\alpha \rightarrow \gamma^* + \sigma$, where γ^* is a new austenite phase. Therefore, the present study of ferrite decomposition forming austenite and sigma phases is based on the in-situ determination of present phases (ferrite (α), austenite (γ), and sigma (σ)) volumetric fraction by the use of x-ray diffraction data. Despite the expected difference in lattice parameter for γ and γ^*, caused by the different chemical compositions, it was not possible to differentiate peaks from both phases. In this section references to γ fraction should be understood as $\gamma + \gamma^*$

fraction. The method used for phase fraction quantification is based on Equation 2.15. The composition and crystalline structure of the σ phase used in Equation 2.10 is based on values reported by Yakel (1983). The present peaks in the observed 2θ region are shown in Figure 4.34. This is an acquisition taken from a sample at 750 °C after 400 s from the start of the temperature plateau, where the evidence of the three phases presence can be clearly seen.

The peaks used for quantification were α{110}, γ{111}, γ{200}, σ{140}, σ{022}, σ{122}, σ{141}, σ{331} and σ{222}. Despite recommendations by Gnäupel-Herold and Creuziger (2011), only one peak was used in the ferrite phase volume fraction determination. This may introduce a bias in fraction determination in case the preferred orientation factor in Equation 2.13 is not equal to one. One way to verify if the quantification based on only one peak is reliable is to compare the quantification results calculated from diffraction measurements with volume fraction measured with other techniques. To do that, the initial scan taken before heating in each test was used to quantify ferrite. Since the σ phase was not present, the only peaks used in quantification were α{110}, γ{111} and γ{200}. Other peaks from both phases were present on the scan, but since the objective was to check the fraction quantification done in the high temperature acquisitions, only the scan region between 32° and 42 ° was used. Ferrite was also quantified using a ferritscope before each test. This equipment allows the measurement of ferrite fraction through the evaluation of the magnetic permeability of a material. The ferrite volume fraction in a sample is calculated by comparing its permeability with that of a set of standards with different known ferrite contents. Figure 4.35 shows a comparison between the volume fraction results using both techniques.

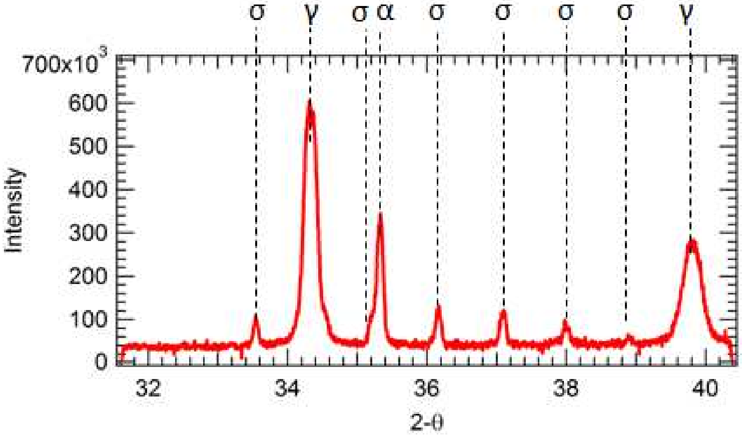

Figure 4.34: **Superduplex diffraction acquisition taken at 750 °C after 400s. Peaks observed are associated with their respective phases. From left to right, the identified peaks are σ{140}, γ{111}, σ{022}, α{110}, σ{122}, σ{141}, σ{331} σ{222} and γ{200}**

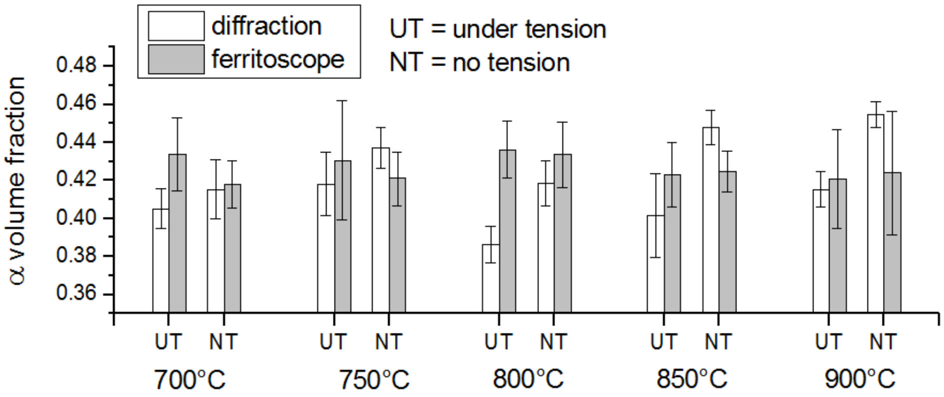

Figure 4.35: **Comparison between ferrite volume fractions determined by a ferritscope and by X-ray diffraction using the 2θ acquisition range shown in Figure 4.34. All samples were measured at room tempetarure prior to the test. The temperatures and tension state indicate the test in which each sample was used.**

In this Figure, samples are identified by the temperature in which they were tested and the stress condition during the test. For most cases, the measured volume fractions are within the error bars given by both techniques, and a significant difference is not observed, except for the sample UT800 °C. The observed difference of 0.039±0.018 in volume fraction could be due to preferred orientation, but could also be caused by sampling statistics, since the techniques used have different gauge volumes. While the gauge volume for X-ray diffraction is discussed on section 4.2, the gauge volume for the ferritscope used is a semi sphere with 3 mm radius. It is not possible to definitely associate the observed difference in sample UT800 °C to preferred orientation. Overall, the data in Figure 4.35 validate the quantification technique used. As for texture evolution during the experiment, in the samples in which no stress was applied this is not a concern, since there is no external effect which would affect crystallites of different orientations differently. In the samples under stress, the applied tension is elastic and crystallite rotation due to plastic strain will not happen. Therefore, the preferred orientation factor used was considered equal to one through the whole test for all tests, and $R_{p\{hkl\}}$ for the phases was calculated as described in Equation 4.22. Nevertheless, the elastic stress may still have an effect on the preferred crystallographic directions for the new phases to grow, but this effect is being disregarded due to simplicity.

Before reaching the temperature plateau, samples were heated at a 100 °C/s heating rate. Acquisitions were made every second during heating, but given the elevated heating rate, the 100 °C temperature variation during the exposure of a single acquisition was high enough that peaks were distorted due to lattice parameter expansion, and analysis of these acquisitions is not reliable. Still, mainly for the higher temperatures, the initial volume fractions observed for ferrite are less than the values observed at the start of the plateau, indicating that an observable volume fraction of ferrite had already transformed during heating. This is shown on Figure 4.36 a, where the ferrite fraction determined by diffraction is shown for the ten samples. Fractions were determined using the diffraction measurement at room temperature and the first measurement of the plateau. Figure 4.36 b shows the difference between the fractions determined at room temperature minus the one determined at high temperature, and it can be observed that the difference is only considerable for the 850 °C and 900 °C samples.

The phase volume fraction evolution with time at the temperature plateau is shown in Figure 4.37 to Figure 4.41, where the fraction for all phases is shown as a function of time. The zero in the time scale marks the start of the isothermal plateau.

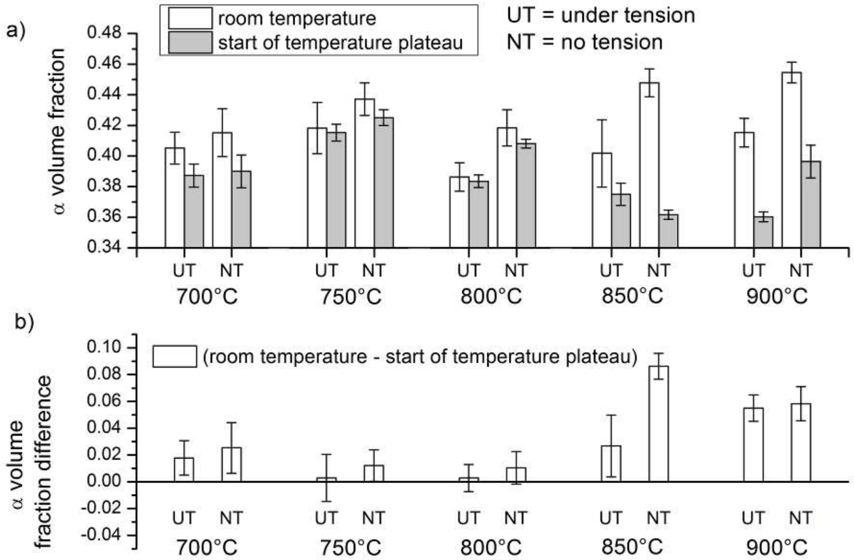

Figure 4.36: a) Comparison between ferrite volume fractions at room temperature and at the start of the temperature plateau. b) Difference between fractions at room temperature minus at the start of the temperature plateau. Fractions were determined by X-ray diffraction using the 2θ acquisition range shown in Figure 4.34. The temperatures and tension state indicate the test in which each sample was used.

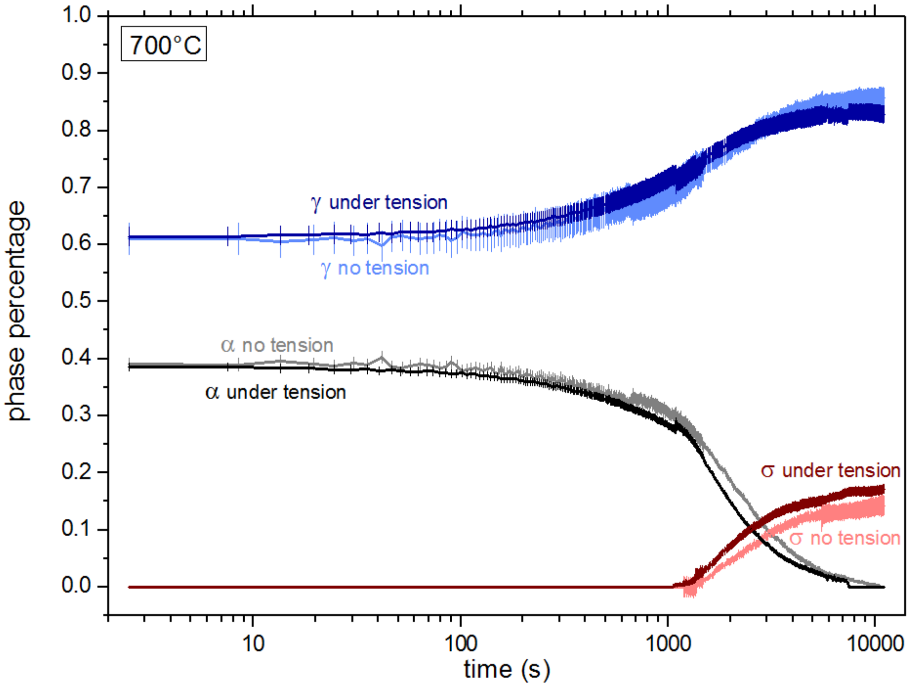

Figure 4.37: Phase volume fractions as a function of time for the stressed and unstressed samples at 700 °C. Tension = 240±8 MPa; Percentage of yield strength = 100±3%

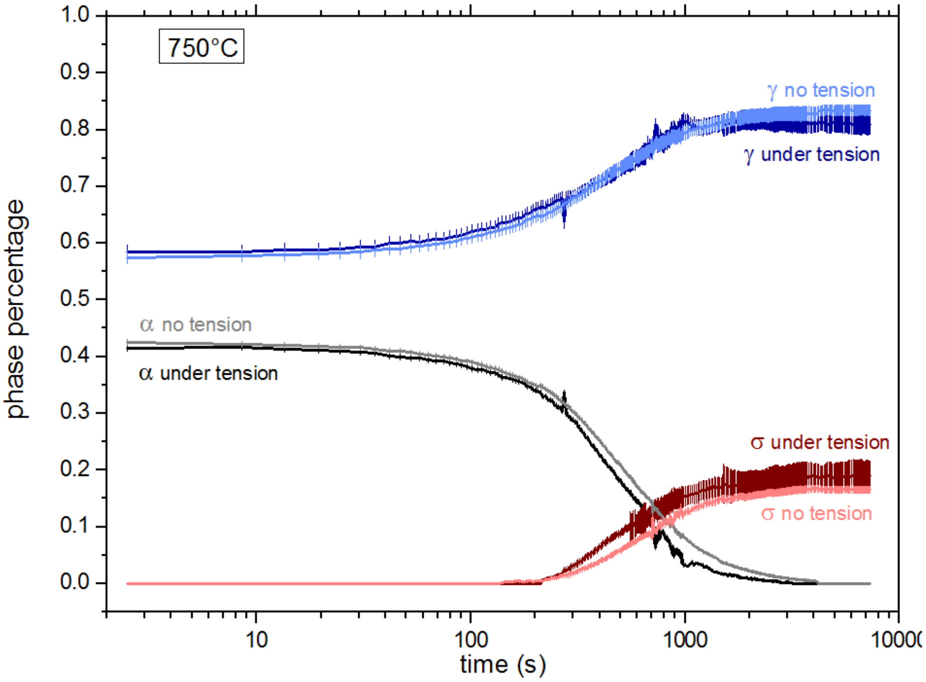

Figure 4.38: Phase volume fractions as a function of time for the stressed and unstressed samples at 750 °C. Tension = 200±8 MPa; Percentage of yield strength = 100±4%

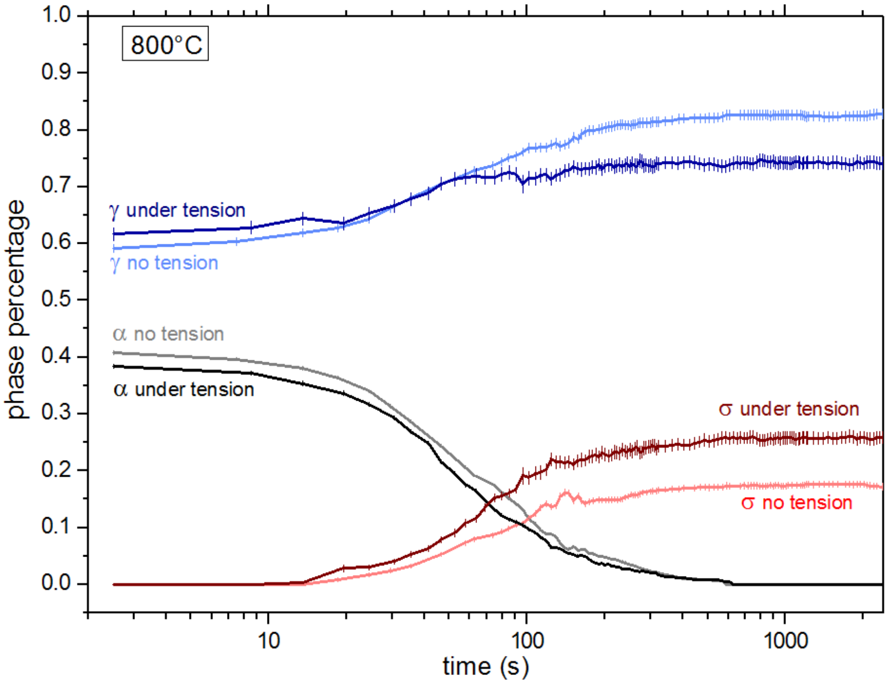

Figure 4.39: Phase volume fractions as a function of time for the stressed and unstressed samples at 800 °C. Tension = 120±8 MPa; Percentage of yield strength = 75±5%

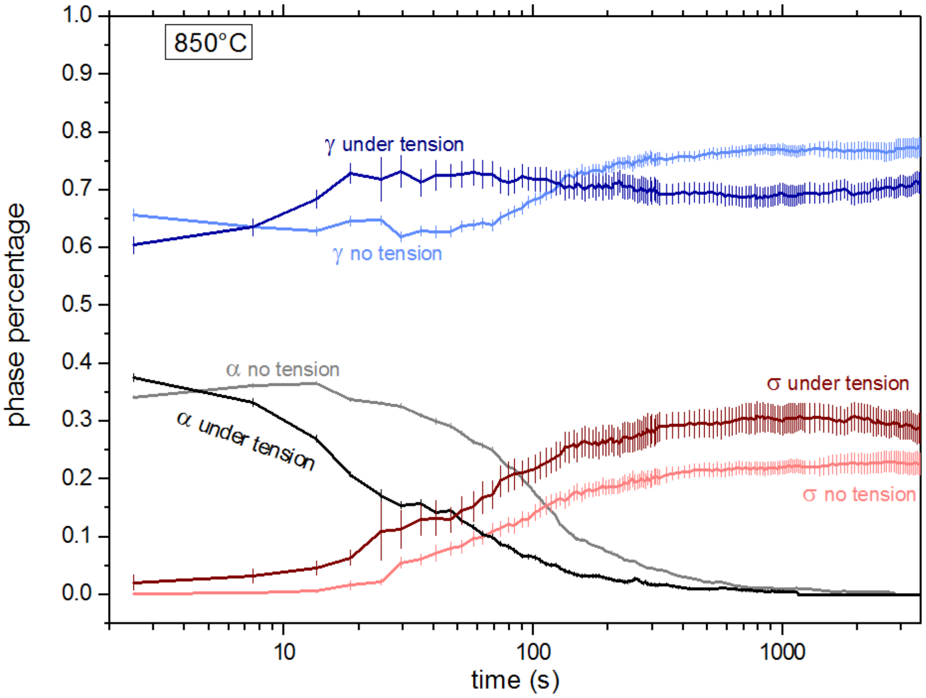

Figure 4.40: Phase volume fractions as a function of time for the stressed and unstressed samples at 850 °C. Tension = 80±8 MPa; Percentage of yield strength = 70±7%

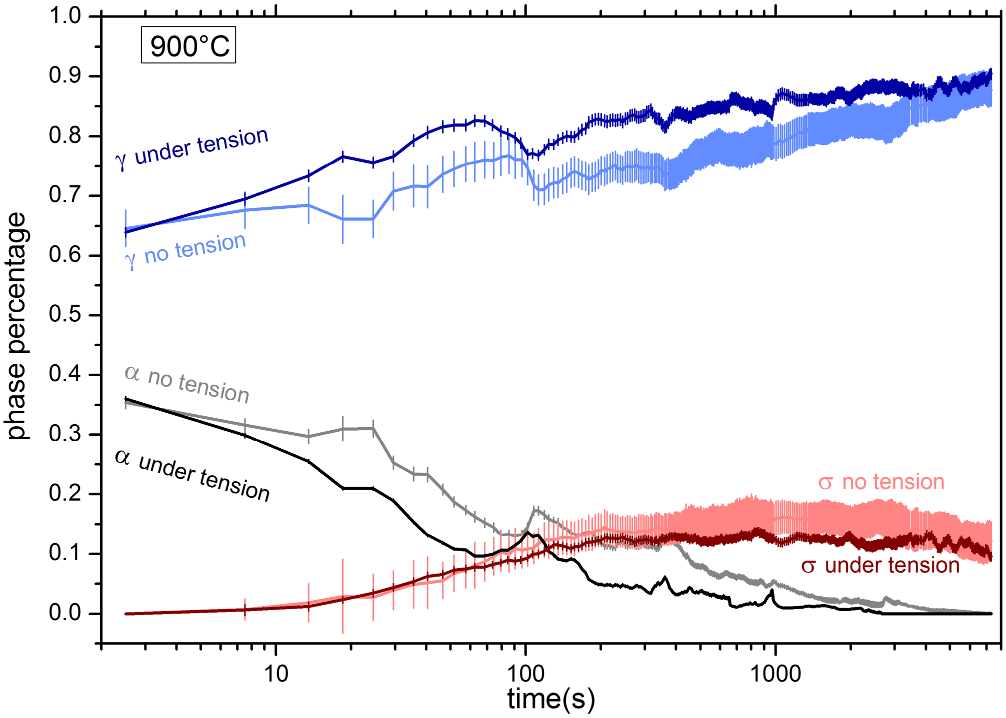

Figure 4.41: Phase volume fractions as a function of time for the stressed and unstressed samples at 900 °C. Tension = 40±8 MPa; Percentage of yield strength = 40±8%

In Figures Figure 4.37: to Figure 4.41: it can be clearly seen that the tension applied is increasing the ferrite phase decomposition kinetics. For all temperatures, tension increases the σ phase formation rate and final fraction, except for 900 °C. Additionally, at 750 °C and 800 °C, tension presented a more relevant effect on ferrite decomposition σ than in austenite. For the tests performed at 900 °C with and without tension and at 850 °C with tension, a slight decrease in σ fraction can be observed for long times, which is probably associated to a σ to γ transformation, since no other phases can be observed. The σ phase is formed through ferrite decomposition and once this last phase has practically vanished, atoms composing σ may now occupy less energetic sites within the austenite. Nevertheless, the long range diffusion within the austenite grains, now relevant for the considered times, can also be playing a role in this sigma phase fractions reduction, which should be now approaching equilibrium conditions. However, as the plateaus duration were planned based on the ferrite decomposition, there is not enough time to fully achieve thermodynamic equilibrium and determine the stable volume fraction of σ at the tested temperature and tension conditions. In Figure 4.42 the observed σ phase fraction at the end of the isothermal plateau for each temperature is shown.

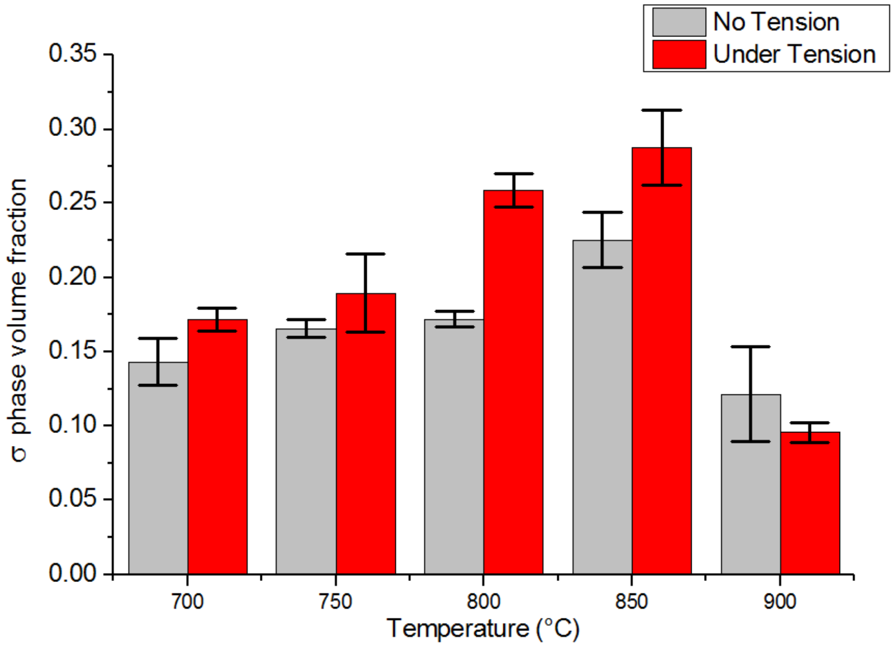

Figure 4.42: σ phase volume fraction at the end of the measured plateaus.

The tension effects can be summarized as follows:

- It increases ferrite decomposition rate at all temperatures.
- It increases σ formation rate and final fraction except for 900 °C.
- Transformation rate increase is larger for σ phase than for austenite.

These effects can be understood by taking into account nucleation and diffusion fundaments described on section 2.5. The applied stress generates an elastic strain with an associated elastic energy, characterized by the work done locally by the stress field. This work can be calculated by (DIETER, 1986):

$$W = \frac{1}{2}[\sigma]\cdot[\varepsilon]. \qquad \text{Equation 4.26}$$

Such work will have an effect on nucleation as described on Equation 2.23 and Equation 2.24, increasing the Gibbs free energy of the phases involved in the transformation. However, the nucleation rate depends on the Gibbs free energy difference between phases involved, and not directly on their total energy. Therefore, if the transformation kinetics changes with the applied stress, and if this difference is associated to nucleation, one possible explanation for such effect is based on the fact that the work done on the matrix and the nuclei is different. In this case, being the nucleation homogeneous or heterogeneous, there will be a difference between the volume term ΔG_V generated by the difference in work.

As for diffusion, it would not be affected by the stress per se, but rather by a gradient in strain energy along the material, as shown on Equation 2.30. Strain variation in a single grain is possible, but considering that this material has a matrix composed by two phases, the strain partitioning between both phases is much more significant than intragranular strain variations. Several results in the literature show the stress partitioning between austenite and ferrite in duplex and superduplex steels. These results cover room temperatures (JIA et al., 2008), following typical use conditions for these steels, and temperatures above 1000 °C (MARTIN et al., 2012), following the typical conformation temperature for duplex alloys. These results show that at room temperature, austenite presents a higher elastic strain than ferrite, while for high temperatures (950 °C), the opposite happens. The different strains mean different strain energies, therefore, if at the test temperatures there is a significant strain partitioning between the phases, there will be a elastic energy gradient at interfaces, increasing diffusion of atoms to this interface, which is where the heterogeneous nucleation of γ* and σ is expected, in accordance to microstructural evidence (WEISBRODT-REISCH et al., 2006).

As discussed on section 2.5, for high temperatures, transformation kinetics is controlled by nucleation, and for lower ones, by diffusion. The interplay between these transformation kinetics mechanisms and ferrite decomposition can be better understood by creating a TTT diagram for the ferrite phase decomposition. The diagram shown on Figure 4.43 and was created using the remaining volume fraction of ferrite regarding this phase fraction at the temperature plateau start. Similar graphs could be created for γ and σ, but given the error bars on the determined fractions of these phases, results are not conclusive.

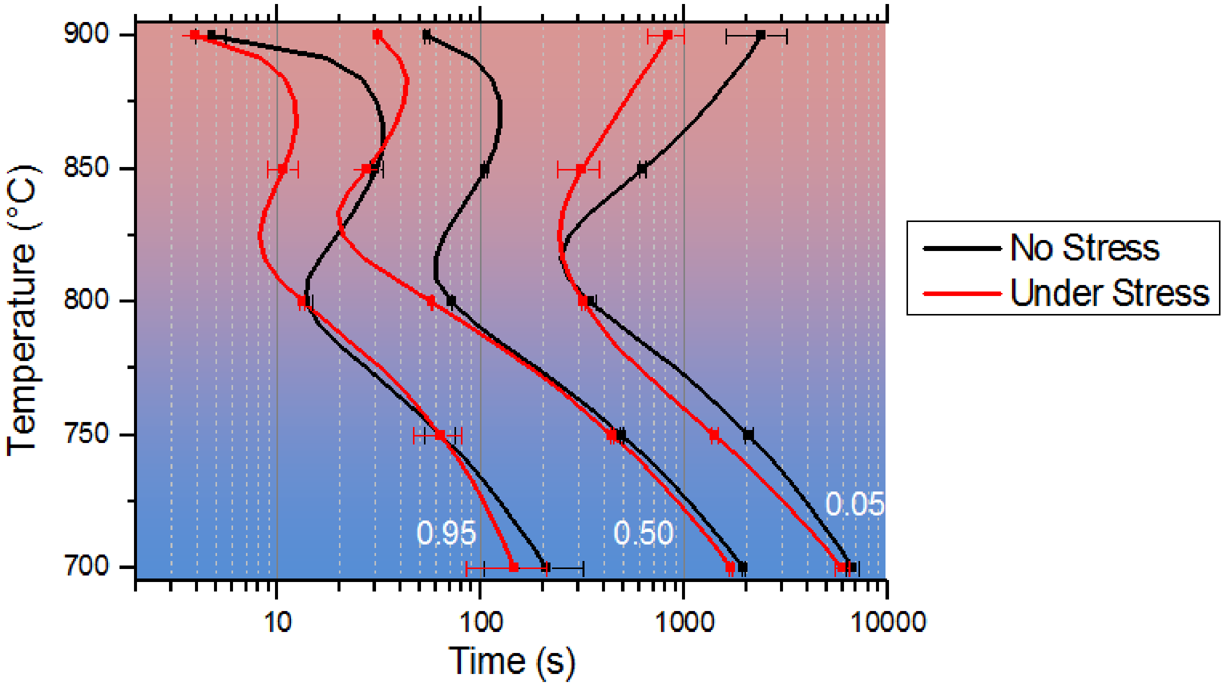

Figure 4.43: Ferrite remaining fraction as a function of time and temperature. The fraction was calculated regarding the volume fraction at the start of the temperature plateau. Points are experimental data, lines are spline curves plotted to facilitate visualization. The figure blue/red background represents the transition from the diffusion (blue) to nucleation (red) controlled transformation regimes.

As stated before, austenite has higher strain energy than ferrite at room temperature while ferrite has higher strain energy in temperatures above the test temperatures used. That means that at some point between room temperature and 950 °C, the strain energies on both phases are equal. As stated above, stress can only have an effect in diffusion if there is strain energy partitioning. The low effect of stress in the diffusion limited transformation regime could be explained by the possibility of both phases to store similar strain energy at this temperature range. Given the ferrite decomposition happening in these temperatures, determining stress partitioning among ferrite and austenite poses a challenge. In addition, no results on stress partitioning in duplex alloys carried in temperatures between 700 °C and 900 °C were found in the literature.

Associating the stress effect on transformation kinetics with nucleation at temperatures above 800 °C and with diffusion below 800 °C, a final analysis in these results can be made to determine when these regimes are more intense during the transformation. To do that, the difference between ferrite remaining percentage on tests with and without stress was calculated. The results are shown on Figure 4.44. As the transformation have different time scales depending on temperature, the time axis in this figure was plotted from 2s to the time in which the ferrite remaining percentage in the unstressed samples reach 5%.

For all temperatures, a negative bulge can be observed, while the difference at the start and at the end is almost zero. This bulge indicates the temporal region in which the stress effect was more accentuated, and therefore, where the transformation mechanisms activated by stress happened more intensely. As shown on Figure 4.44, for lower temperatures the bulge happens in long time scales, near the end of the transformation, when possible nucleation sites are mostly depleted and the change in volume fraction is happening due to migration of atoms from one phase to the other, or in other words, through diffusion. On the other hand, at higher temperatures, the bulge is located at the beginning of the test, where nucleation of new grains is intense. Finally, the most important effect of stress is observed at 850 °C, where the stress effect on both nucleation and diffusion has a synergetic effect on kinetics.

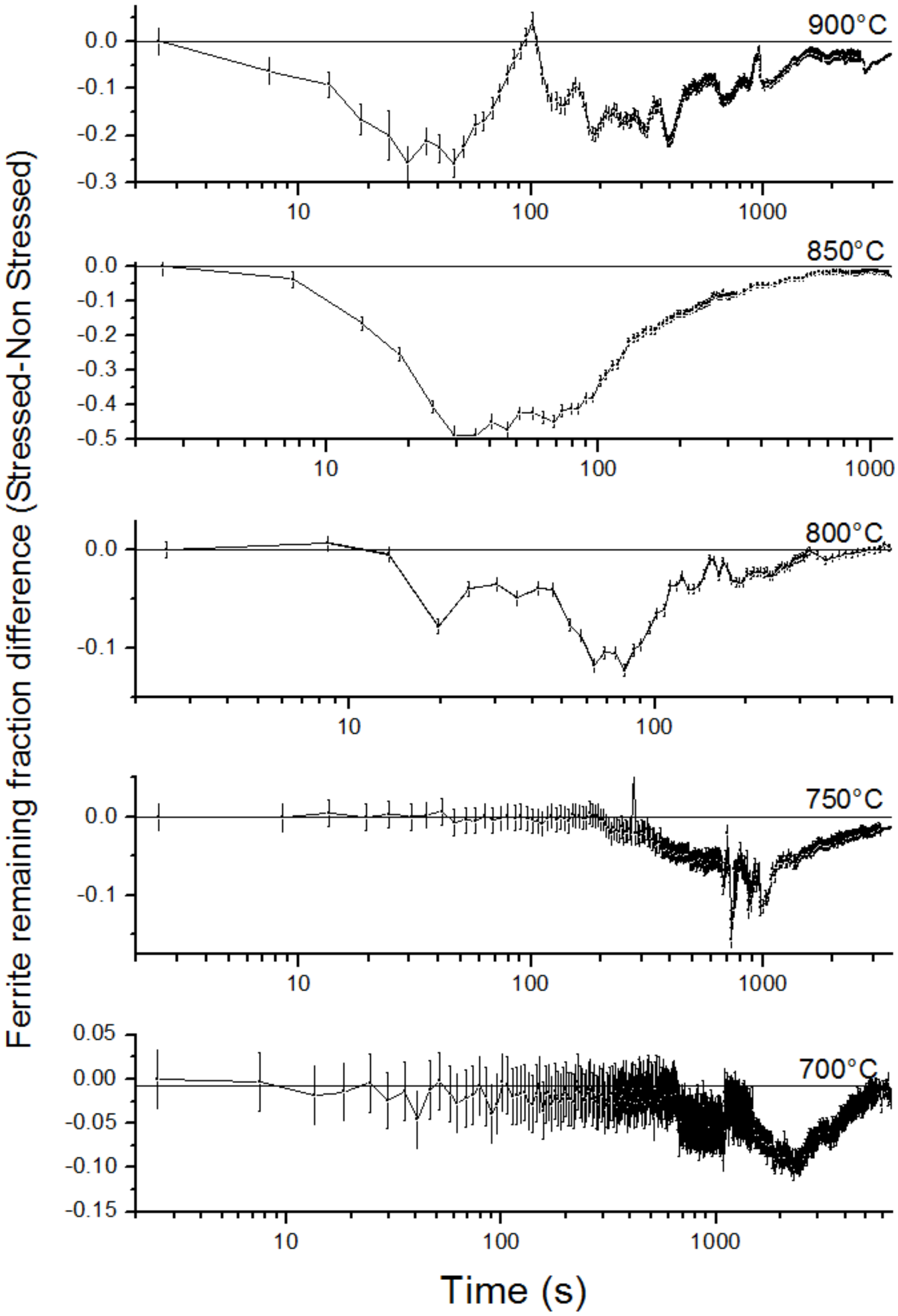

Figure 4.44: **Difference between ferrite remaining percentage on the stressed and unstressed samples as a function of time. The time range plotted in each graph correspond to the time required for the ferrite fraction to reach 0.05 on the non-stressed samples.**

4.6. Phase Transformations and Stress Relief on Supermartensitic Stainless Steel SuperCr13

Supermartensitic steels have high mechanical strength and medium toughness. This toughness can be improved by the retention of a fraction of austenite in its microstructure which is obtained by careful heat treatments. These treatments can be optimized if the martensite to austenite transformation is well understood. The goal of the experiment shown in this section was to study this transformation.

The experiment was performed with an incident beam energy of 12 keV, and given the 2θ angular region observed, peaks {110} and {200} from martensite and {111} and {200} from austenite were followed. The diffraction, temperature and dilatometry data collected during heating are shown on Figure 4.45. A curious result can be observed regarding the evolution with time of peak positions from the {110} and {200} martensite peaks.

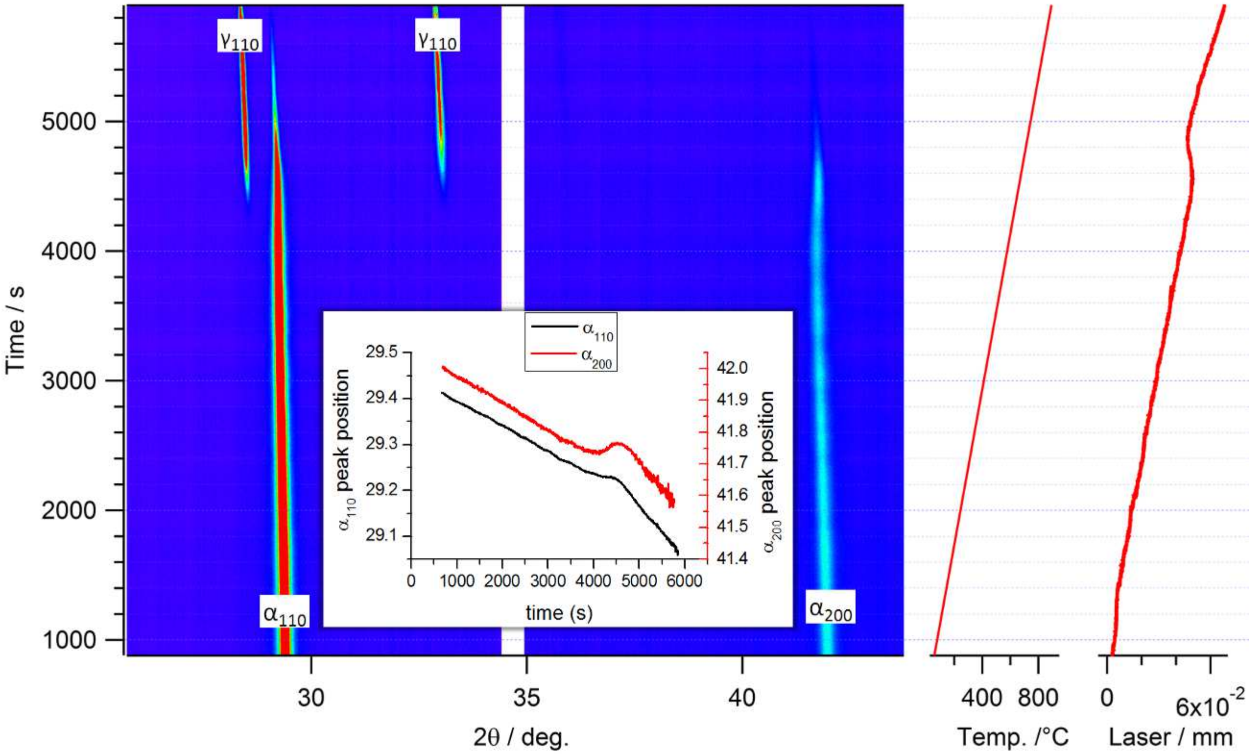

Figure 4.45: Diffraction, temperature and laser dilatometry data collected during the heating of a SMSS sample, shown as a function of time. The intensity collected in the measured 2θ region is shown on a color scale as a function of time and 2θ. On the inset, peak position for the $\alpha_{\{110\}}$ and $\alpha_{\{200\}}$ peaks are shown as a function of time.

As can be seen on Figure 4.45, near the start of the transformation, both martensite peaks present a shift. To investigate this behavior, information such as *d* spacing, microstrain and phase percentages were derived from the measured peaks. Lattice parameter for the {110} and {200} families of martensite were calculated independently based on their respective *d* spacings. Figure 4.46 a) to d) shows these lattice parameters behavior with temperature, as well as sample dilatometry, phase volume fractions, and Δd/d calculated from the {110} and {200} martensite peaks. As shown on this Figure, the lattice parameters start different, but match after the peak shift. Besides, not only the measured lattice parameters are different, but they show a peculiar behavior with temperature. Three hypotheses can be proposed to explain this behavior. They are listed in the following sections.

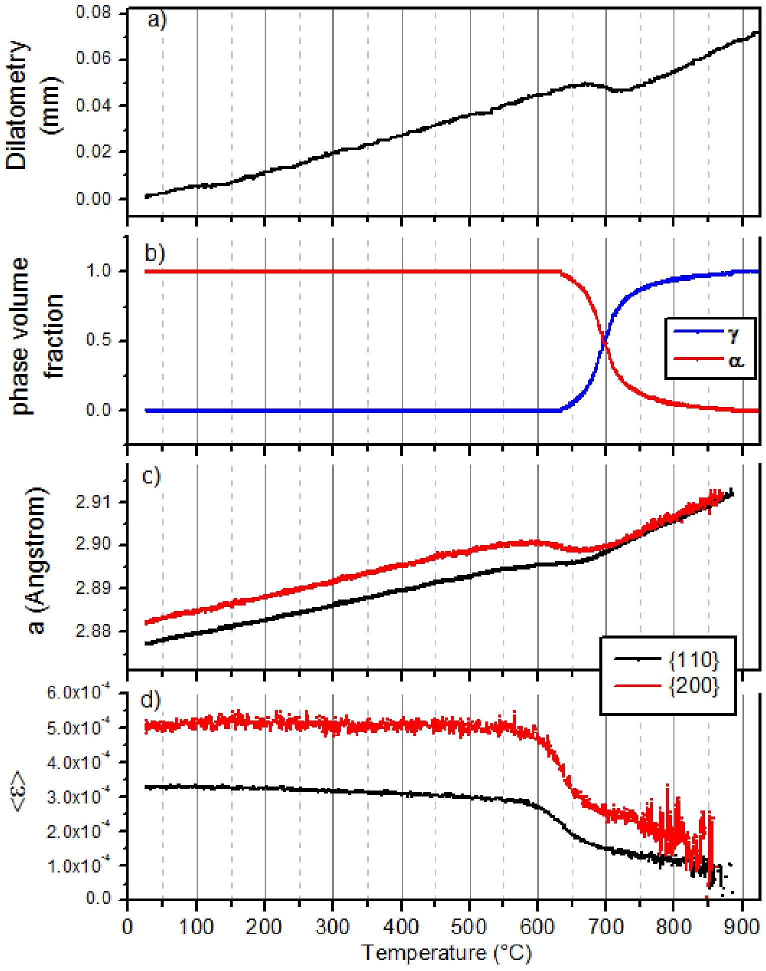

Figure 4.46: Dilatometry (a), α and γ phase volume fractions (b), α{110} and α{200} observed lattice parameter (c) and α{110} and α{200} <ε> for a supermartensitic stainless steel during 10 °C/min heating.

4.6.1. First peak shift hypothesis – instrumental error

The first one is that this is an instrumental error, that is, there is an error in the positioning of the goniometer so that the measurement of 2θ is wrong. This could be a scaling error between pixel position and 2θ. Such an error would have a high effect on the scans taken at the sample, due to the fact that when the goniometer center is positioned at different 2θs, the same peak would be measured in different angles due to the incorrect scaling. As no features are observed in the scans, this hypothesis is not plausible. The other possible error would be a sample misalignment, which would cause deviation in the 2θ value. Peak positions were corrected with Equation 4.6, but if the sample was misaligned, a shift would still exist (Equation 4.17). It could be stated that the sample was misaligned at the start of the experiment, but at the point when the sample diameter change behavior at 650 °C the sample surface become aligned through thermal dilation, minimizing the lattice parameter difference. For small 2θ deviations, the relationship between a shift in sample diameter and a shift in 2θ is linear, and so will be its relationship with the calculated lattice parameter. If such a misalignment existed, in the same way the sample became aligned due to thermal dilation, it would become misaligned afterwards, given its constant dilation. Therefore, this hypothesis is also incorrect.

4.6.2. Second peak shift hypothesis – change in Carbon concentration

The second hypothesis is based on the fact that the lattice parameter was calculated taking into account a BCC structure, whereas the interstitial carbon in martensite can break the symmetry of the Bravais lattice to a tetragonal body centered (BCT) structure. If this phenomenon is happening, peaks being diffracted by planes parallel to (101) and (011) would not belong to the same plane family as peaks being diffracted by planes parallel to (110). A similar symmetry break would happen with the {200} plane family. In the case of the observed diffraction conditions, {110} peaks should split in families {110} and {101}, and {200} peaks should split in {200} and {002}. Nevertheless, with the typical β_{obs} of 0.2 ° observed in the experiment, it would not be possible to define a difference between the two peaks from a plane family split. However, in a simplistic model, the centroid of the observed peak can be taken as the average between all the 2θ angles of a split family weighted by their respective multiplicities. With this approach, an estimative for the lattice parameter calculated from the cubic model, $a_{\{hkl\}}^{obs}$, can be derived from the supposed a for the tetragonal model and the tetragonality t using Equation 2.6 and Equation 2.7, which yields:

$$a_{110}^{obs} = a\left(\frac{1}{3}+\frac{2}{3}\sqrt{\frac{2}{1+t^{-2}}}\right) \quad \text{and} \quad a_{200}^{obs} = a\left(\frac{2+t}{3}\right). \qquad \text{Equation 4.27}$$

The tetragonality of martensites depends on several alloying elements besides carbon, as well as on martensite morphology (KAJIWARA; KIKUCHI, 1991), but a quick estimation can be done with the equation proposed by Kurdjumov:

$$t = 1 + 0.0467(\text{wt.\%C}) \qquad \text{Equation 4.28}$$

Considering a = 2.88 Å and a carbon content of 0.024wt.% the difference between observed lattice parameters should be around 10^{-5} Å, whereas the typical observed difference is around 5 x 10^{-3} Å, two orders of magnitude higher. Therefore, this is also not a valid hypothesis.

4.6.3. Third peak shift hypothesis – changes in stress state

The third hypothesis is based on the assumption that the sample is under a macrostress state. Stress implies strain, and if the sample crystallites are subjected to different strains in different crystallographic orientations, the lattice parameters calculated from these orientations would be different. Considering the anisotropic elastic properties of single crystals and that each crystallite is itself a single crystal, it is valid to assume that crystallites in different orientations would suffer different strains. To check this hypothesis, a homogeneous stress field is assumed on the sample, and the strains generated along the measured directions can be evaluated through Hooke's Law.

$$[\boldsymbol{\varepsilon}] = [\mathbf{S}] \cdot [\boldsymbol{\sigma}] \qquad \text{Equation 4.29}$$

where **[ε]** is the strain tensor, **[S]** is the compliance tensor and **[σ]** is the stress tensor. The stress tensor is defined on the sample reference frame as shown on Figure 4.47. The stress components along $\hat{\boldsymbol{e}}_3$ direction (σ_{13}, σ_{23} and σ_{33}) were considered null given the fact that the measured volume is close to the surface, where the material is under a planar stress state.

In this configuration, the strain in crystallites measured in {110} and {200} plane families can be calculated as shown on Equation 4.30 and Equation 4.31. A detailed description of the mathematical derivation of these equations is presented on Appendix A.

$$\varepsilon_{\{002\}} = 2S_{12}\sigma_K , \qquad \text{Equation 4.30}$$

$$\varepsilon_{\{110\}} = S_{12}\sigma_K + \frac{S_{11}}{2}\sigma_K + \frac{S_{12}}{2}\sigma_K + \frac{S_{44}}{4}\sigma_K . \qquad \text{Equation 4.31}$$

where σ_K is calculated using components of the stress tensor through Equation 4.32, where σ_{11} and σ_{22} are defined using the reference frame on Figure 4.47, and S_{ij} are components of the compliance tensor defined in a BCC unit cell reference frame as shown on Figure 4.48, and :

$$\sigma_K = \frac{\sigma_{11} + \sigma_{22}}{2} . \qquad \text{Equation 4.32}$$

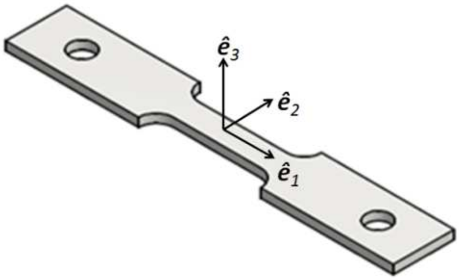

Figure 4.47: Reference frame used in the stress field construction.

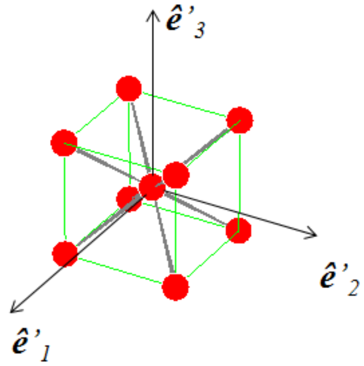

Figure 4.48: Reference frame used in the construction of the compliance tensor.

The relationship between ε and lattice parameter is established by Equation 4.33, and a comparison can be made between the observed lattice parameter values by looking at their difference, as shown on Equation 4.34:

$$\varepsilon_{\{hkl\}} = \frac{a_{hkl}^{obs} - a_0}{a_0}, \qquad \text{Equation 4.33}$$

$$a_{200}^{obs} - a_{110}^{obs} = a_0 \sigma_K \left(\frac{S_{12}}{2} - \frac{S_{11}}{2} - \frac{S_{44}}{4} \right), \qquad \text{Equation 4.34}$$

where a_0 is the unstrained lattice parameter. For materials with positive strain energy $S_{11} \geq 0$ and $S_{44} \geq 0$. Also, $S_{12} = -v_{xy}/E_x$, and given the reference frame used, $v_{xy} > 0$ (NORRIS, 2006), meaning that $S_{12} < 0$. Therefore, the term inside parenthesis on Equation 4.34 is always negative, while a_0 is always positive. Hence, under the assumptions made and the configuration used in this experiment:

$$\begin{cases} \sigma_K < 0 \Leftrightarrow a_{200}^{obs} > a_{110}^{obs} \\ \sigma_K > 0 \Leftrightarrow a_{200}^{obs} < a_{110}^{obs}. \end{cases} \qquad \text{Equation 4.35}$$

In fact, residual stress measurements taken in this sample in a non-heat-treated area show that σ_K is negative (

Table 4.1), whereas Figure 4.46 c) show that $a_{200}^{obs} > a_{110}^{obs}$.

Table 4.1: Residual Stress values on non-heat-treated region of the sample.

Residual Stress	
σ_{11}	-372±25 MPa
σ_{22}	-216±18 MPa
σ_{12}	3±27 MPa
σ_{K}	-294±22 MPa

This consistency shows that this is a valid hypothesis, but in order to confirm it, quantitative evaluations should be made. To follow this approach, the unstrained lattice parameter and the compliance tensor for the single crystal martensite grains in this steel must be known. This poses a severe limitation since, as the martensite formation generates residual stresses, it is not possible to determine the unstressed lattice parameter directly in bulk materials. On the other hand, very few techniques allow the measurement of the tensor in small crystallite grains such as the martensitic ones, and on the few reported values for the compliance tensor of martensitic single crystals, there is a large variation depending on chemical composition and thermal history.

Kim and Johnson (2007) published orthogonal stiffness tensor parameters for two microstructures of a UNSG10500 steel. One microstructure was induction hardened, being completely martensitic and the other was non-hardened, being composed of a mixture of ferrite and perlite. Results for a pure iron single crystal were also reported. The compliance tensor will be the inverse of the stiffness tensor, and using Equation 4.34 and the reported stiffness tensor parameters, the unstrained lattice parameter at room temperature can be calculated. For the orthogonal tensors, C_{11} was taken as the average between C_{11}, C_{22} and C_{33}, C_{44} was taken as the average between C_{44}, C_{55} and C_{66}, and C_{12} was taken as the average between C_{12}, C_{13} and C_{23}. This is justified due to the multiplicity of the measured plane families, since all 90° rotation of the initial orientation also contribute to diffraction. Results are shown on Table 4.2.

Table 4.2: Calculated unstrained lattice parameter through Equation 4.34 using [C] values reported by Kim and Johnson (2007). The Microstructures and reported C_{11}, C_{12} and C_{44} are shown.

Microstructure	C_{11} **(GPa)**	C_{12} **(GPa)**	C_{44} **(GPa)**	a_0 **(Å)**
Induction hardened (martensite)	267.9 ± 0.6	110.8 ± 0.5	78.88 ± 0.04	2.62 ± 0.19
Non-hardened (ferrite-perlite)	273.6 ± 0.5	110.7 ± 0.4	81.78 ± 0.03	2.72 ± 0.20
Pure Iron	231.5 ± 0.5	135.0 ± 0.5	116.0 ± 0.08	2.26 ± 0.17

Given the typical Fe metallic radius (GREENWOOD; EARNSHAW, 1997), the calculated a_0 value is lower than expected for all used compliance parameters, and especially for pure Iron ones. However, small changes in the compliance tensor have a large effect on the calculated a_0 value given the hyperbolical relationship between both, which is shown by the large variation between values for different microstructures. Still, given that the calculated lattice parameters for different microstructures are in the same order of magnitude as the expected value, and given the typical variations of the compliance tensor for different materials and microstructures, the observed results validate the stress hypothesis.

A more interesting analysis can be done by observing how the observed lattice parameter difference changes throughout heating. Figure 4.49 a shows a plot of this difference, b shows the difference between <ε> for α' {200} and α' {110}, and c shows the phase volume fraction, all as a function of temperature.

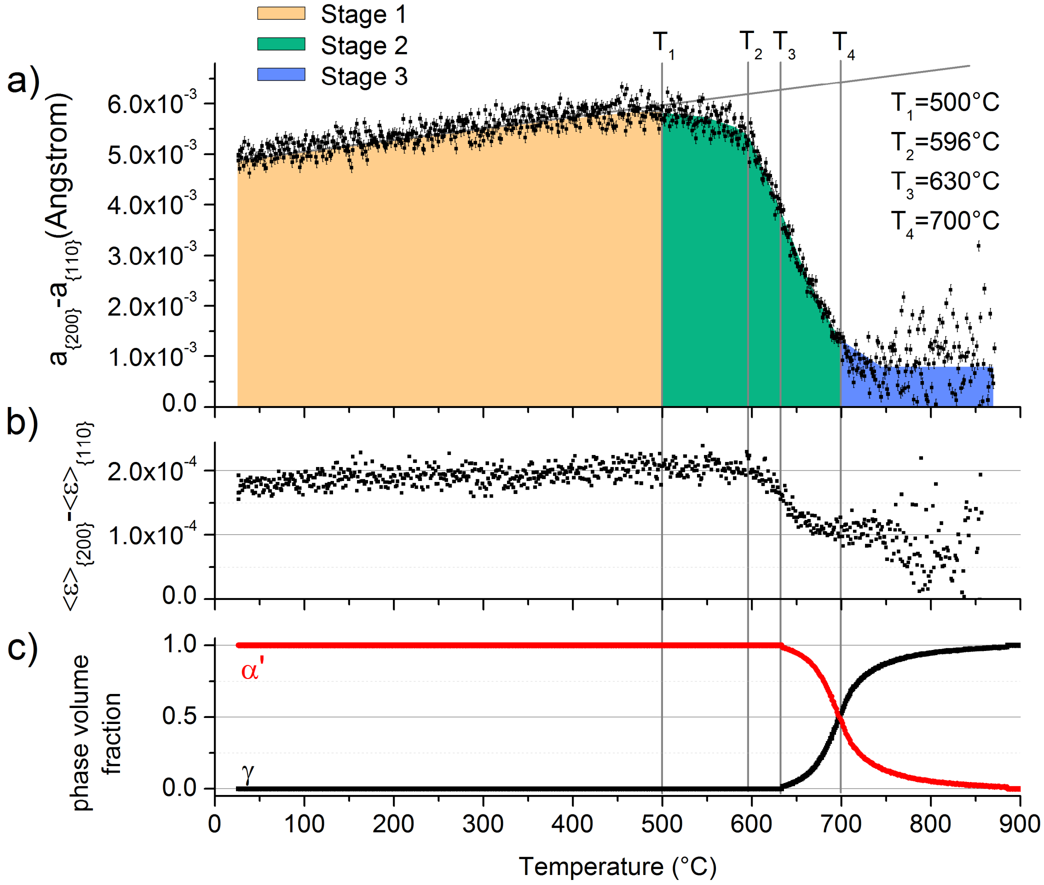

Figure 4.49: Observed lattice parameter (a) and <ε> (b) difference for {110} and {200} plane families, and phase volume fraction for γ and α' (c) as a function of temperature during heating.

Observing Figure 4.49 a, three stages can be clearly defined. During stage 1, the observed lattice parameter difference is increasing. This is probably due to thermal expansion of the unstressed lattice parameter a_0, in accordance with Equation 4.34. During stage 2, the thermal expansion is overcome by the decrease in other factors, either σ_K or the compliance parameters. Given the large reduction on lattice parameter difference, the terms causing this reduction must be drastically changing as well. Such a reduction is more likely happening in σ_K than in the compliance parameters. Therefore, the sample is under stress relief during stage 2. Stage 3 starts when the matrix becomes austenitic, and the remaining martensite is possibly unstressed.

Another interesting observation concerns the relationship between the macro stress and observed microstrain. As shown on Figure 4.46 d, $<\varepsilon>$ is different for the two martensite peaks, which indicates the existence of anisotropic peak broadening. According to Table 2.2, this is related to the presence of dislocations, stacking faults or twinning. In Figure 4.49 b, the difference between $<\varepsilon>$ for the two plane families is plotted against temperature. Shortly after the start of stage 2, at temperature 596 °C indicated by T_2, the microstrain difference starts to decrease, indicating a reduction in the density of the crystalline defects causing anisotropic peak broadening. This decrease happens between T_2 and T_4, where the variation in $a_{\{200\}}$-$a_{\{110\}}$ is steeper. After T_4, a remaining anisotropy in broadening is still observed since the microstrain difference is still non zero.

As stated before, the reduction in microstrain difference between T_2 and T_3 is related to a reduction in the density of three possible defects: dislocations, stacking faults and twinning. In order to annihilate dislocations, the material must be subjected to a temperature in which the dislocations can move freely. The same happens for partial dislocations, which, when recombined, eliminate stacking faults. On the other hand, twinning is only removed when the twinned grains disappear, which can happen due to a phase transformation or recrystallization. It is reasonable to assume that the temperatures required to annihilate dislocations and recombine partial dislocations are lower than that required for recrystallization(PADILHA; SICILIANO, 2005). Therefore, it can be assumed that between T_2 and T_4 the number of dislocations and/or stacking faults in the martensitic matrix is being reduced. After T_4, anisotropy still exists due to twinning. As shown on Table 2.2, if the peak shift caused by these defects on plane families

{110} and {200} is different, their presence can be used to explain the non zero $a_{\{200\}}$-$a_{\{110\}}$ difference in stage 3.

Looking back at the stress relief discussion, two hypotheses can be explored to explain this phenomenon during stage 2:

1. The yield strength of the material decreases with the increase of temperature, and over 500 °C, it becomes smaller than the residual stress. During stage 2, the material minimizes the stress by straining plastically. There are three mechanisms for plastic deformation of polycrystalline metallic materials: creation and movement of dislocations, twinning, and creep (PADILHA; SICILIANO, 2005). At this temperature creep is not possible. Therefore, if there is plastic strain, there would be an increase in dislocation and/or twinning density, while the microstrain difference behavior shows a decrease in such densities. Therefore this hypothesis is invalid.

2. There is a compressive residual stress on the sample. From the measured lattice parameters at this temperature, austenite has a density approximately 2% smaller than martensite. Although it is not possible to determine the elastic macrostrain on martensite, it is reasonable to assume that it is at least one order of magnitude smaller than 2%. That means that a very small amount of new austenite would be enough to relieve the compressive residual stress on the samples. Coupled with that, there is the fact that while it is hard to determine phase volumetric fractions less than a few percent with X-ray diffraction, this technique is very sensitive to interplanar spacings. Therefore, the martensite behavior during stage 2 could be due to formation of a small austenite fraction, which, despite being too small to be directly observed by X-ray diffraction, could be relieving residual stress on the martensite matrix. If this is the case, the reduction in dislocation density proposed above could be due to the fact that the regions of the martensite matrix which are transforming to austenite are the areas under highest strain, hence having the higher dislocation density.

Based on the presented discussions, the second hypothesis is more likely to be correct than the first one. However, from the collected data alone it is not possible to state that austenite is being formed before T_3, nor that there is a correlation between stress relief and dislocation density behavior, as observed by the microstrain anisotropy.

5. CONCLUSIONS AND PROPOSED FUTURE STUDIES

This work is comprised of an extensive characterization of the XTMS installation. Such unique installation, which couples crystallographic and dilatometric analysis with thermo-mechanical simulation has shown to be a powerful tool to uncover fundamental aspects of materials science and optimize materials and processes, both in a expedite manner. The use of the installation enables the determination of subtle connections between materials properties, their microstructure and atomic structure, as well as the observation of thermodynamic and kinetic phenomena under specific and well controlled conditions. The advanced instrumentation and integrated control allow simple and versatile experiment programming, being accessible to new users. The capabilities of the simulator and diffraction setup allow for a large range of experiments, simulating complex processes with impressive time resolution.

Studies on sample design and the facility characterization as a diffraction installation were performed. Methodologies on data analysis and data processing were also developed. Finally, the facility feasibility and capabilities were put to test through the investigation of different phenomena in three different structural metallic materials. In the next sections, the conclusions arising from each of these areas are shown.

5.1. Sample Design

The use of several different sample designs is possible in the installation. However, the sample cross section along the diffraction plane must respect a few constraints. The surface used for diffraction must be flat, while the samples with round sides perform better for high accuracy stress measurements. Therefore, a hybrid cross section is optimal, consisting of a circular area with symmetrical straight edges. The values for the sample thickness between the straight edges and for the circular region radius are not fixed, but values used for sample design must be carefully selected so as not to limit the X ray beam incidence angle.

The sample sides must be designed so it can be assembled in the fittings used to load the latter in the simulator. There are different fitting possibilities, allowing more accurate choice of incident angle, higher maximum possible load, or smaller required sample size, depending on experiment requirements.

The middle section of the sample, or its reduced cross section length, can be adjusted based on the experiment goal. Longer lengths deliver higher temperature resolution in the gauge volume, whereas shorter lengths allow higher cooling rates. The adequate value for most experiments is 20 mm.

5.2. Characterization as a diffraction instrument

Characterization of the installation as a diffraction instrument was performed focusing on three different fields, diffraction angle accuracy, instrumental broadening of diffraction peaks and scattered X-rays absorption.

In the diffraction angle accuracy field, the data collected in the detectors was found to have a potentially high accuracy, although this accuracy is very dependent on alignment. When comparing data from a single peak taken during the same experiment, this resolution can go up to 10^{-5} °. However, based on the typical resolution of variables used in the alignment, the resolution in 2θ scale is limited to approximately 10^{-3} ° for typical sample designs and assembly conditions. This resolution will depend on 2θ.

As a future development, a strategy to improve this resolution is to reduce the uncertainty on the determination of variables affecting alignment, such as dy, dz and ω, especially the latter. The installation is equipped with a long distance microscope, assembled in the goniometer arm. By using digital image analysis techniques, the sample edges can be found in the images taken by the microscope. The use of this microscope for alignment can increase the resolution in the determination of ω by a few orders of magnitude. This can be achieved by observing how the distance between the sample edges in the image coordinate system changes as a function of 2θ. ω will be the angle in which this difference is minimal.

As for instrumental broadening and absorption, analytical models were constructed to describe how these vary with 2θ. When crossed with experimental data, these models yielded accurate predictions, meaning that they can be used in the equations for determination of phase volume fractions and sample originated diffraction peak broadening.

One limiting factor of the facility is that only crystallites oriented in a small region of a 4π solid angle satisfy the diffraction condition. Besides, the volume irradiated by the incident beam is small, given the limited beam size and penetration. Beam size is limited horizontally by sample thermal gradients and vertically by geometric parameters, while beam penetration in the sample is limited on most materials by the maximum available energy at the beamline. Therefore, diffraction data collected is originated in a limited number of crystallites in very specific orientations, reducing the statistical significance in the derived crystallographic information. However, as discussed on sections 4.4 and 4.6, the fact that diffracting crystallites are at known orientations regarding the sample allows the observation of anisotropic phenomena.

Even so, in most experiments it is interesting to increase the observed volume to achieve better sampling statistics. This can be achieved in two ways. If 2D detectors are used, a much larger number of crystallites will be oriented so that diffraction condition is satisfied, since diffraction data collection would not be limited to a single plane. If a higher energy is used, the beam penetration in the samples would also be higher, increasing the number of crystallites observed.

5.3. Data processing and analysis

The data processing routine developed is versatile and powerful, given the possibility of customizing peak search algorithms and least squares fitting. The peak search algorithm can be refined so diffraction peaks are consistently identified, even when peaks have unusual signal-to-noise ratio, broadening or shape. The least squares fitting can also be modified so fitting convergence is increased. However, this customization can be cumbersome and time consuming. This routine is prepared for use in whole pattern fitting analysis, such as the Rietveld method, but the application of these methods normally requires the assumption of several hypotheses on the sample, which is incompatible with the statistical significance of the collected data. An analysis based on the observation of each peak behavior during a test was found to be a more interesting approach, revealing how crystallites at different orientations react to the applied thermomechanical conditions.

5.4. Scientific Case Studies

5.4.1. Stress Induced Phase Transformation in Shape Memory Stainless Steels

The shape memory alloys go through different stress induced transformations during deformation, forming either ε or α'. The possible transformations are γ→ε, γ→α' or γ→ε→α'. The transformations happen during different portions of the deformation, with ε formation from the start of the plastic regime up to 0.02 strain. The α' formation initiate at 0.01 strain, but only increases significantly after 0.02 strain, lasting until 0.04 strain. The sample can only recover 0.017 of the total 0.037 plastic strain applied. Since γ→ε transformation is recoverable while γ→α' or γ→ε→α' is not, the limited recovery can be associated with α' formation. Variant selection is observable in the γ→ε transformation, generating texture in the samples.

In a future work, an interesting way to observe this variant selection directly is to repeat this experiment using a 2D detector. The behavior of crystallites oriented in several directions regarding the load application direction can be followed by observing peak intensities of a same plane family at different azimuth angles.

5.4.2. Ferrite Decomposition on Superduplex Stainless Steel UNS S32750

The application of stress increases the eutectoid $\alpha \rightarrow \gamma^{*}+\sigma$ transformation kinetics the UNS S32750 steel at all temperatures studied, having a larger effect at 850 and 900 °C. Stress also seems to increase σ formation rate and final σ fraction, except at 900 °C. These effects happen through changes in the nucleation energies and diffusion mechanisms. Regarding nucleation, stress can increase the volumetric Gibbs free energy difference between parent phase and nuclei through differences in the work done on each phase, and the heterogeneous nucleation energy term, both increasing the nuclei generation rate. As for diffusion, the stress/strain partitioning between the present phases increases diffusion, consequently increasing the new phases growth rate. Stress has a larger effect on the nucleation limited than on diffusion limited transformation kinetics.

As shown on calculations performed in Appendix A, crystals at diverse orientations regarding a homogeneous stress field will have different strains. If more than one plane family is observed during the ferrite decomposition experiment, the relationships between the strain energy of crystallites satisfying different diffraction conditions can be calculated, similarly to the way they were in Appendix A. To further understand the stress effect on the transformation, the rate of decrease of each ferrite plane family can be observed independently in a future work. As the stress is known and the difference between its effect in each orientation is known, qualitative and quantitative data on the strain energy can be derived.

5.4.3. Phase Transformations and Stress Relief on Supermartensitic Stainless Steel SuperCr13

Uncommon behavior in martensitic diffraction peaks was observed during heating of a SMSS sample. This behavior was associated with residual stress through the construction of a mathematical model that describes strain on crystallites at specific orientations regarding a homogeneous stress field. Predictions made with this model were compared with sample residual stress measurements and literature results, and it was validated. Using the model in the collected data, a stress relief temperature range was identified. The α'→γ transformation starts in this temperature range, and the residual stress on the martensitic phase seems to reach its minimal value at the same temperature at which γ volume fraction reaches 0.5. There also seems to be a reduction in dislocation and/or stacking fault density during the stress relief stage.

The results seem to indicate a correlation between the stress relief and annihilation of dislocation/recombination of partial dislocations, although it is not possible to state the existence of a correlation from the collected data alone. An interesting future work proposal consists of performing a similar experiment using samples with different initial dislocation densities. This can be achieved by applying different plastic strains in the samples at room temperature, prior to the test. By observing how peak shift and anisotropic broadening vary during heating, a clearer answer on dislocation annihilation and partial dislocation recombination can be reached. The initial strain may induce different initial residual stresses in the samples, but these can be measured prior to the test, and the correlation between the stress relief and dislocation density evolution can be evaluated.

REFERENCES

ALS-NIELSEN, J.; MCMORROW, D. **Elements of Modern X-ray Physics**. 2nd. ed. Chichester, UK: John Wiley & Sons, 2011. p. 434

ARFKEN, G. B.; WEBER, H. J. **Mathematical Methods for Physicists**. 6th. ed. [s.l.] Elsevier, 2005.

ARRUDA, G.; BUONO, V.; ANDRADE, M. The influence of deformation on the microstructure and transformation temperatures of Fe–Mn–Si–Cr–Ni shape memory alloys. **Materials Science and Engineering: A**, v. 275, n. 1999, p. 528–532, 1999.

ASTM E 8M. Standard Test Methods for Tension Testing of Metallic Materials. **ASTM International**, p. 1–28, 2013.

BABU, S. S. et al. In-situ observations of lattice parameter fluctuations in austenite and transformation to bainite. **Metallurgical and Materials Transactions A**, v. 36, n. 12, p. 3281–3289, 2005.

BARCELLONA, A.; PALMERI, D. Effect of Plastic Hot Deformation on the Hardness and Continuous Cooling Transformations of 22MnB5 Microalloyed Boron Steel. **Metallurgical and Materials Transactions A**, v. 40, n. 5, p. 1160–1174, 26 fev. 2009.

BHADESHIA, H. K. D. H. **Worked examples in the Geometry of Crystals**. 2nd. ed. London: The Institute of Metals, 2001.

CALLIARI, I.; ZANESCO, M.; RAMOUS, E. Influence of isothermal aging on secondary phases precipitation and toughness of a duplex stainless steel SAF 2205. **Journal of Materials Science**, v. 41, n. 22, p. 7643–7649, 19 set. 2006.

CARROUGE, D. **Microstructural change in high temperature heat-affected zone of low carbon weldable'13% Cr' martensitic stainless steels**. [s.l.] University of Cambridge, 2002.

CULLITY, B. **Elements of X-ray Diffraction**. READING, MASSACHUSETTS: ADDISON-WESLEY PUBLISHING COMPANY, INC., 1956.

DAI, H. et al. Characterizing Phase Transformations and Their Effects on Ferritic Weld Residual Stresses with X-Rays and Neutrons. **Metallurgical and Materials Transactions A**, v. 39, n. 13, p. 3070–3078, 17 jul. 2008.

DIETER, G. E. **Mechanical Metallurgy**. 1st. ed. London, UK: McGraw-Hill Book Company, 1986. p. 751

DOHERTY, R. D. Difusive Phase Transformations in The Solid State. In: CAHN, R. W.; HAASEN, P. (Eds.). . **Physical Metallurgy**. 3rd. ed. Amsterdam, The Netherlands: North-Holland Physics Publishing, 1992. p. 933–1030.

ELMER, J. W. et al. In situ observations of lattice expansion and transformation rates of α and β phases in Ti–6Al–4V. **Materials Science and Engineering: A**, v. 391, n. 1-2, p. 104–113, jan. 2005.

ESCOBAR, J. D. **Transformações de fase associadas ao processamento termomecânico do aço inoxidável supermartensítico Transformações de fase associadas ao processamento termomecânico do aço inoxidável supermartensítico**. [s.l.] State University of Campinas, 2013.

ESCOBAR, J. D.; RAMIREZ, A. J.; MEI, P. R. **Microstructural characterization of friction stir welded of 12Cr-6Ni-2Mo-0.13Ti supermartensitic stainless steel**11° Seminário Brasileiro do Aço Inoxidável. **Anais**...São Paulo: 2012Disponível em: <http://www.abinox.org.br/upfiles/arquivos/downloads/inox12/soldagem/to15.pdf>. Acesso em: 15 set. 2014

ESCRIBA, D. M. et al. Chi-phase precipitation in a duplex stainless steel. **Materials Characterization**, v. 60, n. 11, p. 1214–1219, nov. 2009.

FANG, C. M.; VAN HUIS, M. A.; ZANDBERGEN, H. W. Structural, electronic, and magnetic properties of iron carbide Fe_{7}C_{3} phases from first-principles theory. **Physical Review B**, v. 80, n. 22, p. 224108, dez. 2009.

FERGUSON, D. et al. A look at physical simulation of metallurgical processes, past, present and future. **Materials Science and Engineering: A**, v. 499, n. 1-2, p. 329–332, jan. 2009.

FERRARI, M.; LUTTEROTTI, L. Method for the simultaneous determination of anisotropic residual stresses and texture by x-ray diffraction. **Journal of Applied Physics**, v. 76, n. 11, p. 7246, 1994.

FEUGEAS, J. N. et al. In situ synchrotron radiation diffraction study of low carbon steel during ion nitriding. **Journal of Physics D: Applied Physics**, v. 32, n. 17, p. 2228–2235, 7 set. 1999.

GARIN, J.; MANNHEIM, R. RIETVELD PROCESSING OF PHASES IN HIGHLY TEXTURED REFRACTORY STEELS. **Advances in X-ray Análisis**, v. 48, p. 82–87, 2005.

GENZEL, C. et al. The materials science synchrotron beamline EDDI for energy-dispersive diffraction analysis. **Nuclear Instruments and Methods in Physics Research Section A: Accelerators, Spectrometers, Detectors and Associated Equipment**, v. 578, n. 1, p. 23–33, jul. 2007.

GILES, C.; YOKAICHIYA, F. High-resolution X-ray diffraction beamline at the LNLS for the study of charge, orbital and magnetic structures. **Journal of synchrotron …**, n. 2003, p. 430–434, 2003.

GNÄUPEL-HEROLD, T.; CREUZIGER, A. Diffraction study of the retained austenite content in TRIP steels. **Materials Science and Engineering: A**, v. 528, n. 10-11, p. 3594–3600, abr. 2011.

GREENWOOD, N. N.; EARNSHAW, A. **Chemistry of the Elements**. [s.l.] Butterworth-Heinemann, 1997.

HAEFFNER, D. R.; ALMER, J. D.; LIENERT, U. The use of high energy X-rays from the Advanced Photon Source to study stresses in materials. **Materials Science and Engineering: A**, v. 399, n. 1-2, p. 120–127, jun. 2005.

HAHN, T. et al. **International tables for crystallography**. Fifth ed. Norwell, USA: IUCR - Springer, 2005.

HENKE, B. L.; GULLIKSON, E. M.; DAVIS, J. C. X-Ray Interactions: Photoabsorption, Scattering, Transmission, and Reflection at E = 50-30,000 eV, Z = 1-92. **Atomic Data and Nuclear Data Tables**, v. 54, n. 2, p. 181–342, jul. 1993.

ID11 - Materials science beamline. Disponível em: <http://www.esrf.eu/UsersAndScience/Experiments/StructMaterials/ID11>. Acesso em: 25 jul. 2014.

IUCR. Report of the Executive Committee for 1991. **Acta Crystallographica Section A Foundations of Crystallography**, v. 48, n. 6, p. 922–946, 1 nov. 1992.

JAMES, R.; HANE, K. Martensitic transformations and shape-memory materials. **Acta materialia**, v. 48, 2000.

JIA, N. et al. Tensile Deformation Behavior of Duplex Stainless Steel Studied by In-Situ Time-of-Flight Neutron Diffraction. **Metallurgical and Materials Transactions A**, v. 39, n. 13, p. 3134–3140, 10 out. 2008.

KAJIWARA, S.; KIKUCHI, T. On the abnormally large tetragonality of martensite in Fe□ Ni□ C alloys. **Acta metallurgica et materialia**, v. 39, n. 6, p. 1123–1131, jun. 1991.

KIM, S. A.; JOHNSON, W. L. Elastic constants and internal friction of martensitic steel, ferritic-pearlitic steel, and α-iron. **Materials Science and Engineering: A**, v. 452-453, p. 633–639, abr. 2007.

KOMIZO, Y.; TERASAKI, H. In situ time resolved X□ray diffraction using synchrotron. **Science and Technology of Welding and Joining**, v. 16, n. 1, p. 79–86, jan. 2011.

KONDO, K. et al. **Alloy Design of Super 13 Cr Martensitic Stainless Steel (Development of Super 13 Cr Martensitic Stainless Steel for Line Pipe)**Supermartensitic Stainless Steels. **Anais**...Belgium: 1999

KRIVOGLAZ, M. A. **X-Ray and Neutron Diffraction in Nonideal Crystals**. New York: Plenum Press, 1969.

KVAALE, P.; OLSEN, S. Experience with supermartensitic stainless steels in flowline applications. **Stainless Steel Word**, p. 19–26, 1999.

LAGOUDAS, D. C. **Shape Memory Alloys - Modeling and Engineering Applications**. New York: Springer, 2008.

LANGE, H.; ROGNE, T. **Material selection of weldable super martensitic stainless steels for pipeline material in the offshore industry**. Trondheim, Norway: [s.n.].

LANGFORD, J. Some applications of pattern fitting to powder diffraction data. **Progress in crystal growth and characterization**, v. 14, p. 186–211, 1987.

LANGFORD, J. I.; WILSON, A. J. C. Seherrer after Sixty Years: A Survey and Some New Results in the Determination of Crystallite Size. **Journal of Applied Crystallography**, v. 11, p. 102–113, 1978.

LEEM, D. et al. Amount of retained austenite at room temperature after reverse transformation of martensite to austenite in an Fe–13% Cr–7% Ni–3% Si martensitic stainless steel. **Scripta materialia**, v. 45, p. 767–772, 2001.

MANDZIEJ, S. PHYSICAL SIMULATION OF METALLURGICAL PROCESSES. **materials technology**, v. 44, n. 3, p. 105–119, 2010.

MARTIN, G. et al. Characterization of the High Temperature Strain Partitioning in Duplex Steels. **Experimental Mechanics**, v. 53, n. 2, p. 205–215, 26 maio 2012.

MICHALSKA, J.; SOZAŃSKA, M. Qualitative and quantitative analysis of σ and χ phases in 2205 duplex stainless steel. **Materials Characterization**, v. 56, n. 4-5, p. 355–362, jun. 2006.

NISHIYAMA, Z. **Martensitic Transformation**. 1st. ed. New York, USA: Academic press, 1978. p. 467

NORRIS, A. N. Poisson’s ratio in cubic materials. **Proceedings of the Royal Society A: Mathematical, Physical and Engineering Sciences**, v. 462, n. 2075, p. 3385–3405, 8 nov. 2006.

OTSUKA, K.; WAYMAN, C. M. **Shape Memory Materials**. Cambridge: Cambridge University Press, 1998.

OTUBO, J. **Desenvolvimento de ligas inoxidáveis com efeito de memória de forma: elaboração e caracterização.** [s.l.] State University of Campinas, 1996.

OTUBO, J. et al. Relationship between thermomechanical treatment, microstructure and α' martensite in stainless Fe-based shape memory alloys. **Materials Science and Engineering: A**, v. 273-275, p. 533–537, dez. 1999.

PADILHA, A. F.; SICILIANO, J. F. **Encruamento, Recristalização, Crescimento de Grão e Textura**. 3rd. ed. São Paulo: Associação Brasileira de Metalurgia e Materiais, 2005. p. 232

PORTER, D. A.; EASTERLING, K. E. **Phase transformations in metals and alloys**. 2nd. ed. [s.l.] Springer, 1992.

RAMIREZ, A. J.; BRANDI, S. D.; LIPPOLD, J. C. Study of Secondary Austenite Precipitation by Scaning Electron Microscopy. **Acta Microscopica**, v. 10, n. November, p. 147–148, 2001.

ROCHA, A. DA S.; HIRSCH, T. Fast in situ X-ray diffraction phase and stress analysis during complete heat treatment cycles of steel. **Materials Science and Engineering: A**, v. 395, n. 1-2, p. 195–207, mar. 2005.

SANTELLA, M. L. et al. **A Synchrotron Diffraction Study Of Transformation Behaviour In 9 Cr Steels Using Simulated Weld Heat-Affected Zone Conditions**7th International Charles Parsons Turbine Conference. **Anais**...Glasgow: 2007

SANTOS, T. F. DE A. **Microstructural and performance evaluation of duplex stainless steels friction stir welds**. [s.l.] University of Campinas, 2012.

SATO, A.; SUNAGA, Y.; MORI, T. Contribution of the $\gamma \rightarrow \epsilon$ transformation to the plastic deformation of stainless steel single crystals. **Acta Metallurgica**, v. 25, n. 6, p. 627–634, jun. 1977.

SCHERRER, P. Bestimmung der Grösse und der inneren Struktur von Kolloidteilchen mittels Röntgenstrahlen. **Nachr. Ges. Wiss. Göttingen**, v. 26, p. 98–100, 1918.

SHEWMON, P. **Diffusion in Solids**. 2nd. ed. Warrendale, USA: The Minerals, Metals & Materials Society, 1989. p. 246

SMITH, D. K.; JOHNSON, G. G. Digitized Database Quantification , DDBQ , Analysis of Complex Mixtures using Fully Digitized Patterns. **Advances in X-ray Analysis**, v. 42, n. C, p. 276–286, 2000.

UNGÁR, T. Dislocation densities, arrangements and character from X-ray diffraction experiments. **Materials Science and Engineering: A**, v. 310, n. 0921, p. 14–22, 2001.

UNGÁR, T. Microstructural parameters from X-ray diffraction peak broadening. **Scripta Materialia**, v. 51, n. 8, p. 777–781, out. 2004.

WARREN, B. E. **X-ray Diffraction**. [s.l.] Addison-Wesley, 1969.

WAYMAN, C. M. Phase Transformations, nondiffusive. In: CAHN, R. W.; HAASEN, P. (Eds.). . **Physical Metallurgy**. 3rd. ed. Amsterdam, The Netherlands: North-Holland Physics Publishing, 1992. p. 1032–1074.

WEISBRODT-REISCH, A. et al. Influence of temperature, cold deformation and a constant mechanical load on the microstructural stability of a nitrogen alloyed duplex stainless steel. **Materials Science and Engineering: A**, v. 416, n. 1-2, p. 1–10, jan. 2006.

WILLIAMSON, G.; HALL, W. X-ray line broadening from filed aluminium and wolfram. **Acta Metallurgica**, v. 1, n. January, p. 22–31, 1953.

XIAO, F. et al. Acicular ferritic microstructure of a low-carbon Mn–Mo–Nb microalloyed pipeline steel. **Materials Characterization**, v. 54, n. 4-5, p. 305–314, maio 2005.

YAKEL, H. Atom distributions in Tau-carbide phases: Fe and Cr distributions in (Cr23-xFex) C6 with x= 0, 0.74, 1.70, 4.13 and 7.36. **Acta Crystallographica Section B: Structural Science**, v. 24, n. 1963, p. 230–238, 1987.

YAKEL, H. L. JR. Atom distributions in sigma-phases. II. Estimations of average site-occupation parameters in a sigme-phase containing Fe, Cr, Ni, Mo and Mn. **Acta Crystallographica, Section B: Structural Science**, v. 39, p. 28–33, 1983.

YOUNG, R. A. **The Rietveld Method**. [s.l.] Oxford University Press, 1993.

ZHANG, D. et al. In Situ Observation of Phase Transformation in Low-Carbon, Boron-Treated Steels. **Metallurgical and Materials Transactions A**, v. 43, n. 2, p. 447–458, 27 set. 2011.

ZHANG, D.; TERASAKI, H.; KOMIZO, Y. In situ observation of phase transformation in Fe–0.15C binary alloy. **Journal of Alloys and Compounds**, v. 484, n. 1-2, p. 929–933, set. 2009.

ANEX A – Published and Presented Works

Presentations

XI Brazilian Materials Research Society meeting (2012) – Florianópolis, Brazil

New research possibilities for the thermo-mechanically induced phase transformations - Brazilian unique facility for parallel physical simulation and synchrotron x-ray diffraction
Guilherme Abreu Faria, Thais Alonso, Leonardo Wu, Antonio Jose Ramirez

Time resolved analysis of ferrite decomposition and second phase formation in UNS S32205 duplex stainless steels.
Guilherme Abreu Faria, Leonardo Wu, Maysa Terada, Daniel Santolin, Thais Alonso, Antonio Jose Ramirez

Visual-JW2012-Workshop on in situ studies on photons neutrons and electrons – Osaka, Japan

In situ Thermo-Mechanical Study of Shape Memory Stainless Steels
Guilherme Faria, Leonardo Wu, Daniel Santolin, Julian David Escobar, Thais Alonso, Heide Heloise Bernardi, Jorge Otubo, Antonio Jose Ramirez

Stress Effect On The Kinetics Of Intermetallic Phase Precipitation On UNS S32205 Duplex Stainless Steel
Guilherme Abreu Faria, Leonardo Wu, Maysa Terada, Daniel Santolin, Thais Alonso, Antonio Jose Ramirez

7th International Conference on Mechanical Stress Evaluation by Neutron and Synchrotron Radiation / Australian Nuclear Science and Technology Organisation. – Sydney, Australia (2013)

Parallel thermo-mechanical processing and synchrotron x-ray diffraction for in-situ phase transformations studies under strain/stress conditions: XTMS – Beamline at LNNano (X-ray Scattering and Thermo-Mechanical Simulation)

Antonio Jose Ramirez, Guilherme Abreu FariaLeonardo Wu, Thais Alonso, Leirson Palermo, Julian David Escobar, Paulo Roberto Mei, Heide Bernardi, Jorge Otubo

Stainless Steel World Conference 2013 - Maastricht, The Netherlands

In-situ study of reversed austenite and TRIP effect of a Ti stabilized supermartensitic stainless steel
Julian David Escobar, Guilherme Abreu Faria, Leonardo Wu, Paulo Roberto Mei, Antonio Jose Ramirez

Materials Science Engineering (MSE 2014) – Darmstadt, Germany

The Relationship between the Martensitic Transformation and Macroscopic Behavior during Rapid Cooling of a Martensitic Stainless Steel
Guilherme Abreu Faria, Julian Escobar, Antonio Jose Ramirez

Publications

FARIA, G. A. et al. Advanced Facility For Parallel Thermo-Mechanical Simulation And Synchrotron X-Ray Diffraction. In: KANNENGIESSER, T. et al. (Eds.). **In-situ Studies with Photons, Neutrons and Electrons Scattering II**. 1st. ed. Switzerland, Springer, 2014. p. 245–259.

SMITH, R. et al. In-Situ X-ray Diffraction Analysis of Strain-Induced Transformations in Fe- and Co- base Hardfacing Alloys. **Accepted for publication in Scripta Materialia Sep2014.**

APPENDIX A – Calculating strains on crystalline grains in specific orientations regarding a homogeneous stress field.

The goal of the calculations shown on this appendix is to determine the effect of a homogeneous stress field on single crystal grains observed by diffraction. The stress field is constructed in the reference frame shown on Figure A.1. This reference frame is fixed regarding the sample.

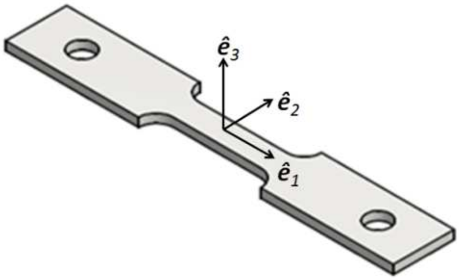

Figure A.1: Sample reference frame used in the definition of the stress tensor.

The crystallites observed by diffraction belong to two plane families, {110} and {200}. Figure A.2 illustrates how the sets of planes contributing to diffraction in the two families would be arranged concerning the reference frame adopted.

As the incident beam penetration is around 5µm, the stress state in these crystallites is considered a planar state, with all stress components along $\hat{\boldsymbol{e}}_3$ being equal to zero. Therefore the stress tensor $[\boldsymbol{\sigma}]$ is constructed in Voigt notation as

$$[\boldsymbol{\sigma}] = \begin{bmatrix} \sigma_{11} \\ \sigma_{22} \\ 0 \\ 0 \\ 0 \\ \sigma_{12} \end{bmatrix}. \qquad \text{Equation A.1}$$

The strains in each set of crystallites can be calculated using Hooke's law, shown in Equation A.2, where [**ε**] is the strain tensor and [**S**] the compliance tensor.

$$[\boldsymbol{\varepsilon}] = [\mathbf{S}][\boldsymbol{\sigma}]. \qquad \text{Equation A.2}$$

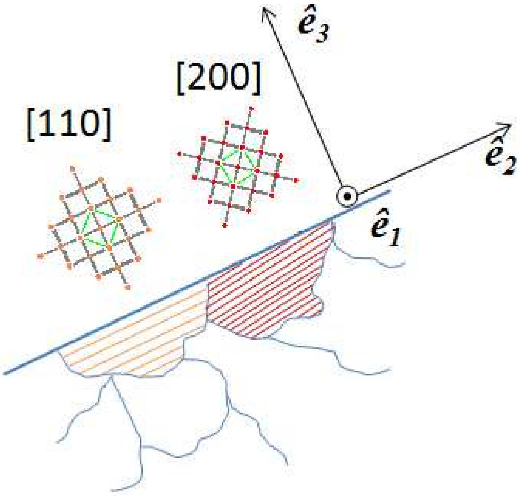

Figure A.2: Orientation of crystallites satisfying the diffraction condition for {111} and {200} plane families regarding the sample reference frame.

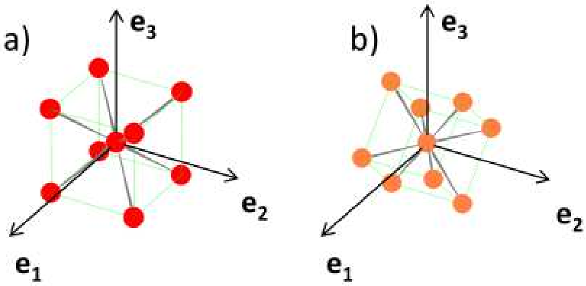

Figure A.3: Reference frames used in the calculation of the compliance parameter for plane families {110} (b) and {200) (a).

The compliance tensor will be different for each plane family, and therefore, must be defined based on the orientation of the crystallites on a plane family regarding the stress field. The compliance tensor is built in a simpler way in the reference frames of the unit cell of the crystallites observed. A different reference frame will be used for each family, so that the compliance tensor carries the symmetry of said plane family. On the {200} plane family, $\boldsymbol{e_1}$ is along [100], $\boldsymbol{e_2}$ along [010] and $\boldsymbol{e_3}$ along [001]. On the {110} plane family, $\boldsymbol{e_1}$ is along [101], $\boldsymbol{e_2}$ along [010] and $\boldsymbol{e_3}$ along [-101] (Figure A.3).

A few factors are taken into account to do this calculation. First one is that the compliance tensor is assumed to have cubic symmetry in the {200} case. For the {110} case, the tensor is rotated 45 ° around the $\boldsymbol{e_2}$ axis, and will have tetragonal symmetry. Following the rotation, elements of [**S**] on {110} plane family ([$\mathbf{S}_{\{110\}}$]) can be written as a function of elements of [**S**] in the {200} plane family ([$\mathbf{S}_{\{200\}}$]). Using these choices for reference frame, the diffraction vector is always parallel to the $\boldsymbol{e_3}$ axis.

There will be three independent values on $S_{\{200\}}$, and six on $S_{\{110\}}$. Additionally, these six values are written in terms of the three values on $S_{\{200\}}$, as those are obtained from a rotation of the later. They are written in Voigt notation on Equation A.3 and Equation A.4.

$$[\mathbf{S}_{\{200\}}] = \begin{bmatrix} S_{11} & S_{12} & S_{12} & & & \\ S_{12} & S_{11} & S_{12} & & & \\ S_{12} & S_{12} & S_{11} & & & \\ & & & S_{44} & & \\ & & & & S_{44} & \\ & & & & & S_{44} \end{bmatrix}, \qquad \text{Equation A.3}$$

$$[\mathbf{S}_{\{110\}}] = \begin{bmatrix} S'_{11} & S_{12} & S'_{13} & & & \\ S_{12} & S_{11} & S_{12} & & & \\ S'_{13} & S_{12} & S'_{11} & & & \\ & & & S_{44} & & \\ & & & & S'_{55} & \\ & & & & & S_{44} \end{bmatrix}. \qquad \text{Equation A.4}$$

$$\text{where } S'_{13} = \frac{S_{11}}{2} + \frac{S_{12}}{2} + \frac{S_{44}}{4}$$

From the rotation, S'_{11} and S'_{55} can also be derived, but are not relevant for this calculation, as will be shown later.

A second consideration is that the sampled crystallites are in a planar stress state. In the measurement condition, the beam penetrates only a few micrometers on the surface. Also given the measurement geometry, the angle between direction [110] for {110} plane family and the normal to the sample surface is 1.1 °, while for [100] at {200} plane family, this angle is 3.8 °. Given these low values, it is assumed that all stress components along the $\boldsymbol{e_3}$ direction in the reference frames are zero.

Finally, before solving Hooke's law, the fact that all orientations for which the diffraction vector lies parallel to the $\boldsymbol{e_3}$ axis in the reference frame choices must be considered, since all of them satisfy Bragg's law, and the final observed strain will be an average of the strain for all the valid orientations. Two approaches can be taken to solve this. One is to fix the reference frame in the sample, and rotate the compliance tensor around $\boldsymbol{e_3}$, and the other is to fix the reference frame in the crystal structure of each plane family and rotate the stress tensor to simulate the stress suffered by the valid orientations. Due to its simplicity, the second approach was chosen. In this calculation, the sample was considered to have no texture. Starting with the stress tensor shown in Equation A.1, and considering σ_{12} null, the rotated stress tensor will be described as a function of the rotation angle φ by Equation A.5.

$$[\boldsymbol{\sigma}'(\varphi)] = \begin{bmatrix} \frac{\sigma_{11}+\sigma_{22}}{2} + \frac{\sigma_{11}-\sigma_{22}}{2}\cos(2\varphi) \\ \frac{\sigma_{11}+\sigma_{22}}{2} - \frac{\sigma_{11}-\sigma_{22}}{2}\cos(2\varphi) \\ \\ \\ \\ \frac{\sigma_{11}-\sigma_{22}}{2}\sin(2\varphi) \end{bmatrix}. \qquad \text{Equation A.5}$$

To simplify notation, the constants σ_K and σ_T are introduced as:

$$\sigma_K = \frac{\sigma_{11}+\sigma_{22}}{2} \text{ and } \sigma_T = \frac{\sigma_{11}-\sigma_{22}}{2}. \qquad \text{Equation A.6}$$

Finally the strain can be calculated, and given the reference frame choices, these are calculated as the projection of the strain tensor in the ***e₃*** direction in both cases. The strains for {200} and {110} plane families are written on Equation A.7.

$$\begin{cases} \varepsilon_{\{200\}}(\varphi) = 2S_{12}\sigma_K \\ \varepsilon_{\{110\}}(\varphi) = S_{12}\left(\sigma_K - \sigma_T \cos(2\varphi)\right) + S'_{13}\left(\sigma_K + \sigma_T \cos(2\varphi)\right) \end{cases}. \qquad \text{Equation A.7}$$

While $\varepsilon_{\{200\}}$ is independent on φ, $\varepsilon_{\{110\}}$ is. Still, all crystallites rotated in different φ angles will contribute to diffraction, and the final strain value will be the average of the strains suffered by all crystallites. Therefore, the final value for $\varepsilon_{\{110\}}$ will be the average integral of $\varepsilon_{\{110\}}(\varphi)$ along φ, which is shown on Equation A.8:

$$\varepsilon_{\{110\}} = S_{12}\sigma_K + \frac{S_{11}}{2}\sigma_K + \frac{S_{12}}{2}\sigma_K + \frac{S_{44}}{4}\sigma_K . \qquad \text{Equation A.8}$$